J. Fluid Mech. (2024), *vol*. 996, A30, doi:10.1017/jfm.2024.681

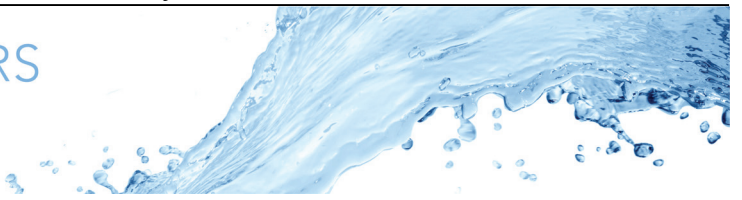

Scale dependence and non-isochoric effects on the thermohydrodynamics of rarefied Poiseuille flow

Shashank Ravichandir[1] **and Meheboob Alam**[1],†

[1]Engineering Mechanics Unit, Jawaharlal Nehru Centre for Advanced Scientific Research, Jakkur PO, Bangalore 560064, India

(Received 14 November 2023; revised 14 May 2024; accepted 24 June 2024)

The plane Poiseuille flow of a rarefied gas in a finite length channel, driven by an axial pressure gradient, is analysed numerically to probe (i) the role of 'dilatation' ($\Delta = \boldsymbol{\nabla}\cdot\boldsymbol{u} \neq 0$) on its thermohydrodynamics as well as to clarify (ii) the possible equivalence with its well-studied 'dilatation-free' or 'isochoric' ($\mathrm{D}\rho/\mathrm{D}t = 0$) counterpart driven by a constant acceleration. Focussing on the mass flow rate $\mathcal{M}(Kn)$, which is an invariant quantity for both pressure-driven and acceleration-driven Poiseuille flows, it is shown that while $\mathcal{M} \sim \log Kn$ at $Kn \gg 1$ in the acceleration-driven case, the mass flow saturates to a constant value $\mathcal{M} \sim Kn^0$ at $Kn \gg 1$ in the pressure-driven case due to the finite length ($L_x < \infty$) of the channel. The latter result agrees with prior theory and recent experiments, and holds irrespective of the magnitude of the axial pressure gradient (G_p). The pressure-dilatation cooling ($\Phi_p = -p\Delta < 0$) is shown to be responsible for the absence of the bimodal shape of the temperature profile in the pressure-driven Poiseuille flow. The dilatation-driven reduction of the shear viscosity and the odd signs of two normal stress differences ($\mathcal{N}_1$ and $\mathcal{N}_2$) in the pressure-driven flow in comparison with those in its acceleration-driven counterpart are explained from the Burnett-order constitutive relations for the stress tensor. While both $\mathcal{N}_1$ and $\mathcal{N}_2$ appear at the Burnett order $O(Kn^2)$ in the acceleration-driven flow, the leading term in $\mathcal{N}_1$ scales as $(\mu/p)\Delta$ due to the non-zero dilatation in the pressure-driven Poiseuille flow which confirms that the two flows are not equivalent even at the Navier–Stokes–Fourier order $O(Kn)$. The heat-flow rate ($\mathcal{Q}_{q_x} = \int q_x(x, y)\,\mathrm{d}y$) of the tangential heat flux is found to be negative (i.e. directed against the axial pressure gradient), in contrast to its positive asymptotic value (at $Kn \gg 1$) in the acceleration-driven flow. Similar to the scale-dependence of the mass flow rate, $\mathcal{Q}_{q_x}(Kn, L_x)$ is found to saturate to a constant value at $Kn \gg 1$ in finite length channels. The double-well shape of the $q_x(y)$-profile in the near-continuum limit agrees well with predictions from a generalized Fourier law. On the whole, the dilatation-driven signatures (such as the pressure-dilatation work and the 'normal' shear-rate differences) are shown to

† Email address for correspondence: meheboob@jncasr.ac.in

© The Author(s), 2024. Published by Cambridge University Press

Downloaded from https://www.cambridge.org/core. IP address: 3.144.47.8, on 13 Nov 2024 at 06:58:59, subject to the Cambridge Core terms of use, available at https://www.cambridge.org/core/terms. https://doi.org/10.1017/jfm.2024.681

be the progenitor for the observed differences between the two flows with regard to (i) the hydrodynamic fields, (ii) the rheology and (iii) the flow-induced heat transfer.

Key words: non-continuum effects, rheology

1. Introduction

The well-known Poiseuille flow through a channel or a pipe, driven by an axial pressure gradient, has served as a prototype (Knudsen 1909) for experimental and theoretical studies over more than a century (Knudsen 1909; Cercignani & Daneri 1963; Raghuraman & Willis 1977; Cercignani 1979; Alaoui & Santos 1992; Tison 1993; Sharipov & Seleznev 1994; Arkilic, Schmidt & Breuer 1997; Sharipov 1999; Zheng, Garcia & Alder 2002; Ewart *et al.* 2007; Graur *et al.* 2009; Marino 2009; Yang & Garimella 2009; Perrier *et al.* 2011; Takata & Funagane 2011; Brancher *et al.* 2021). For an incompressible, isothermal fluid flowing through a channel, the axial pressure gradient remains constant and the streamwise velocity follows the parabolic profile ($u_x(y) = u_0(1 - y^2)$, where x and y denote the streamwise and wall-normal directions, respectively) which is an exact solution of the Navier–Stokes (NS) equations under the assumptions of steady, fully developed flow; the mass flow rate can be calculated in terms of the pressure gradient and the mean velocity. For a compressible fluid (such as molecular gases) undergoing Poiseuille flow, however, there are variations in the density, temperature and velocity along both streamwise and wall-normal directions; the axial variations of the streamwise velocity leads to a non-zero transverse velocity (i.e. $u_y(y) \neq 0$); moreover, the pressure can vary nonlinearly across the channel except in the limit of small pressure gradient. The pressure-driven Poiseuille flow of molecular gases is often analysed in the linear regime of small pressure gradient for which the pressure-gradient is replaced by a constant 'acceleration' or 'body-force' (Cercignani & Daneri 1963; Ohwada, Sone & Aoki 1989; Alaoui & Santos 1992; Tij & Santos 1994; Mansour, Baras & Garcia 1997; Uribe & Garcia 1999; Sone 2000; Aoki, Takata & Nakanishi 2002; Tij & Santos 2004; Gupta & Alam 2017; Rongali & Alam 2018*a*). Such acceleration-driven gaseous Poiseuille flow admits an exact solution of the compressible Navier–Stokes–Fourier (NSF) equations (Tij & Santos 1994; Alam, Gupta & Ravichandir 2021),

$$u_x(y) = u_{x0} - \frac{\rho_0 a}{\mu_0} y^2, \quad u_y(y) = 0, \tag{1.1}$$

$$T(y) = T_0 - \frac{\rho_0^2 a^2}{12\mu_0\kappa_0} y^4, \quad p(y) = \text{constant} = p_0, \tag{1.2}$$

$$\rho(y) = p_0 \left(T_0 - \frac{\rho_0^2 a^2}{12\mu_0\kappa_0} y^4 \right)^{-1}, \tag{1.3}$$

under the assumption of small acceleration ($a \ll 1$), with the subscript '0' on any quantity denoting its value at the channel centreline ($y = 0$) (see the Appendix in Alam *et al.* (2021)). It is clear from (1.1)–(1.3) that while the streamwise velocity follows a parabolic profile, the temperature and density of the gas vary across the wall-normal direction, with the pressure being constant across y. Note that the NSF equations are well suited to describe the behaviour of a gas in the continuum limit, and the departure from the continuum hypothesis can be quantified in terms of the Knudsen number ($Kn = l_f/L$), defined as the ratio between the mean free path (l_f) and the characteristic length (L) of

Downloaded from https://www.cambridge.org/core. IP address: 3.144.47.8, on 13 Nov 2024 at 06:58:59, subject to the Cambridge Core terms of use, available at https://www.cambridge.org/core/terms. https://doi.org/10.1017/jfm.2024.681

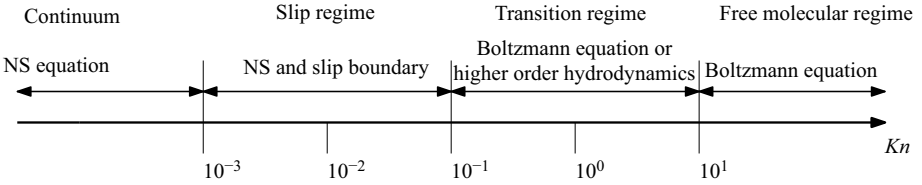

Figure 1. Different flow regimes of a gas characterized by the Knudsen number, $Kn = l_f/L$, where l_f is the mean free path and L is the characteristic length scale.

the flow. The NSF theory is strictly valid in the limit of $Kn \to 0$, and the gas is considered to be in the 'rarefied' regime if $Kn > 0.001$, see the classification of different flow regimes in figure 1; we refer to Akhlaghi, Roohi & Stefanov (2023) for a recent review on related issues in rarefied gas flows.

When the rarefied/non-continuum effects of gases are taken into account, the behaviour of the gas can change qualitatively: for example, in acceleration-driven Poiseuille flow, (i) the temperature profile $T(y)$ contains a local minimum (Tij & Santos 1994; Mansour *et al.* 1997; Rongali & Alam 2018*a*) at the channel centreline, instead of a local maximum at $y = 0$ (see (1.2)) as dictated by the NSF theory; (ii) the transverse pressure profile $p(y)$ is non-uniform; (iii) the mass-flow rate $\mathcal{M}(Kn)$ decreases with increasing Kn, reaches a minimum at $Kn \sim 1$ and then increases logarithmically $\mathcal{M} \sim \log Kn$ at $Kn \gg 1$ (i.e. the well-known Knudsen paradox (Knudsen 1909; Cercignani & Daneri 1963)), whereas the NSF theory can predict only the decaying behaviour of $\mathcal{M} \sim Kn^{-1}$ at $Kn \sim 0$ expectedly; (iv) a finite tangential heat flux ($q_x \neq 0$ in the absence of any temperature gradient along the x-direction) that cannot be explained by the standard Fourier law of heat flux ($\boldsymbol{q} \propto \boldsymbol{\nabla} T$). While the hydrodynamics and rheology of the acceleration-driven Poiseuille flow of rarefied gases have been extensively studied using (i) Boltzmann kinetic theory (Cercignani & Daneri 1963; Tij & Santos 1994; Ohwada *et al.* 1989; Aoki *et al.* 2002; Tij & Santos 2004; Rongali & Alam 2018*a*,*b*), (ii) Burnett-like extended hydrodynamic equations (Uribe & Garcia 1999; Taheri, Torrilhon & Struchtrup 2009; Lv *et al.* 2013; Torrilhon 2016; Rath, Singh & Agrawal 2018; Rath, Yadav & Agrawal 2021) and (iii) the direct simulation Monte Carlo (DSMC) method (Bird 1994; Mansour *et al.* 1997; Alam, Mahajan & Shivanna 2015; Gupta & Alam 2017, 2018), much less attention has been paid to analyse its pressure-driven counterpart (Raghuraman & Willis 1977; Cercignani 1979; Sharipov & Seleznev 1994; Arkilic *et al.* 1997; Sharipov 1999; Beskok & Karniadakis 1999; Zheng *et al.* 2002; Ewart *et al.* 2007; Yang & Garimella 2009; Titarev & Shakhov 2010; Takata & Funagane 2011; Titarev & Shakhov 2012). An (often unspecified) assumption is that the two flows are equivalent (Alaoui & Santos 1992; Takata & Funagane 2011) at least at the NSF order $O(Kn)$.

For the pressure-driven flow of a rarefied gas, the first theoretical work is that of Cercignani & Daneri (1963) who correctly predicted the variation of the mass flow rate with Kn, thereby offering a theoretical explanation on the Knudsen paradox (Knudsen 1909) based on the Boltzmann–Bhatnagar–Gross–Krook (Boltzmann–BGK) kinetic equation. While the channel length was assumed to be infinite ($L_x \to \infty$) in the work of Cercignani & Daneri (1963), the effect of the finite length ($L_x < \infty$) of the channel was analysed later by Raghuraman & Willis (1977) and Cercignani (1979). In both works, the assumptions of (i) no variations in the density and temperature across the channel (i.e. $\rho(x, y) \equiv \rho(x) = \rho_0(1 + G_\rho x/L_y)$ and $T(x, y) = T_0$, where L_y is the width of the channel) and (ii) small pressure/density gradient ($|d(p/p_0)/d(x/L_y)| = G_p \ll 1$) were made such that the linearized version of the Boltzmann–BGK equation can be used

Downloaded from https://www.cambridge.org/core. IP address: 3.144.47.8, on 13 Nov 2024 at 06:58:59, subject to the Cambridge Core terms of use, available at https://www.cambridge.org/core/terms. https://doi.org/10.1017/jfm.2024.681

for analysing this flow. The works of Raghuraman & Willis (1977) and Cercignani (1979) bring out a crucial result: the mass flow rate $\mathcal{M}(Kn, L_x)$ saturates to a constant value at $Kn \gg 1$ if L_x is finite, and the logarithmic branch of $\mathcal{M}(Kn, L_x) \propto \log Kn$ is recovered for a channel of infinite length $L_x \to \infty$. This scale-dependence of $\mathcal{M}(L_x)$ is a key difference between the two flows since the mass-flow rate is an invariant quantity irrespective of the forcing protocol (acceleration- or pressure-driven) that generates the underlying Poiseuille flow.

In addition to the mass flow rate and its dependence on the channel length, there are other quantities like (i) the temperature, density and pressure profiles, (ii) heat-flux and (iii) normal-stress differences, and how they behave in the two flows remains unexplored. Although the leading-order, $O(G_p)$, analysis of Cercignani (Cercignani & Daneri 1963; Raghuraman & Willis 1977; Cercignani 1979), assumes that the gas lives in an isothermal state with its density being uniform across the channel width, the higher-order terms (HOT) in $O(G_p^n, n \geq 2)$ are likely to yield transverse variations of the density and temperature fields. The latter issue is also evident from (1.2)–(1.3) that the transverse variations in $T(y)$ and $\rho(y)$ appear at quadratic order in acceleration, $O(a^2)$. The kinetic theory work of Tij & Santos (1994) discovered the bimodal shape of the temperature profile in the acceleration-driven Poiseuille flow of a rarefied gas which was confirmed later in DSMC simulations (Mansour *et al.* 1997) – this is a super-Burnett order effect that appears at $O(a^4)$. In contrast, the bimodal shape of the temperature profile was not found in the DSMC simulations of the pressure-driven Poiseuille flow (Zheng *et al.* 2002). While the latter simulations were carried out for order-one $G_p = O(1)$ values of the pressure-gradient, the present simulations (Ravichandir & Alam 2024) over a large range of G_p confirmed the absence of temperature bimodality as we shall show in this work. Therefore, the recent literature indicates that there are qualitative differences between the acceleration-driven Poiseuille flow and its pressure-driven counterpart for some hydrodynamic fields, although a detailed comparative analysis of the two forcings and the reasons for underlying differences are still lacking.

Since all experiments belong to pressure-driven Poiseuille flow, starting with the seminal work of Knudsen (1909) as well as the recent experiments (Tison 1993; Ewart *et al.* 2007; Marino 2009; Keerthi *et al.* 2018; Brancher *et al.* 2021; Kunze *et al.* 2022), it is of interest to understand its differences with its much-simplified acceleration-driven counterpart. While the nonlinear regime of large pressure gradient is accessible in experiments, the underlying two-dimensional flow is quite complicated to be explored analytically via perturbation analysis of the nonlinear Boltzmann equation; all related works (Titarev & Shakhov 2010; Takata & Funagane 2011) are based on the linearized version of the Boltzmann equation and/or infinite channel length – the latter assumption simplifies to solving an equivalent one-dimensional problem (Takata & Funagane 2011), which holds as long as the pressure gradient is small enough, but its validity for large pressure gradient remains unknown. In this work we use DSMC simulations to address the following question: is the pressure-driven plane Poiseuille flow of a rarefied gas equivalent to its acceleration-driven counterpart? If not, what makes these two flows different from the viewpoint of mechanics? In addition, we also address: what are the effects of (i) the pressure gradient and (ii) the finite length of the channel on the measurable flow quantities in Poiseuille flow? Does the equivalence (if any) between the two forcings hold for all hydrodynamic and rheological fields in a finite-length channel even in the limit of arbitrarily small forcing-level for which the linearized Boltzmann equation is assumed to hold (Cercignani & Daneri 1963; Cercignani 1979; Ohwada *et al.* 1989; Tij & Santos 1994; Aoki *et al.* 2002; Titarev & Shakhov 2010; Takata & Funagane 2011)? If there are indeed

Downloaded from https://www.cambridge.org/core. IP address: 3.144.47.8, on 13 Nov 2024 at 06:58:59, subject to the Cambridge Core terms of use, available at https://www.cambridge.org/core/terms. https://doi.org/10.1017/jfm.2024.681

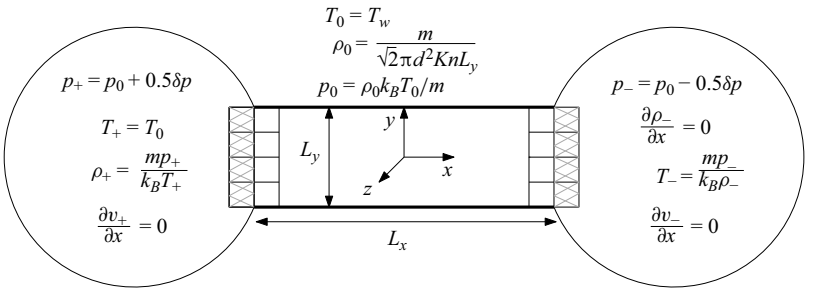

Figure 2. Schematic of the pressure-driven Poiseuille flow in a channel of length L_x and width L_y bounded by two isothermal (diffuse) walls at $T = T_w$, with the z-direction being periodic. The flow is driven by the pressure difference $\delta p = (p_+ - p_-)$ along the streamwise (x) direction. The hatched grey cells at the entrance and exit represent ghost cells to implement inlet and outlet boundary conditions, see § 2.1 for details.

qualitative differences between the two flows with reference to various hydrodynamic and rheological fields, one would like to understand the physical origin of observed differences.

The rest of this paper is organized as follows. We begin § 2 by describing the implementation of boundary conditions (§ 2.1), averaging procedure (§ 2.2) and introduce the control parameters (§ 2.3); the details on the Boltzmann equation and the DSMC method are given in Appendix A. The results on the hydrodynamic fields and the mass-flow rate are discussed in detail in § 3. The results on the shear stress, shear viscosity and normal stress differences are discussed in § 4; the heat flux vector and the tangential heat flow rate are characterized in § 5. The reasons for observed differences in hydrodynamic fields, rheology and heat flux between the two flows are explained (§§ 3.2.2, 3.3, 4.3 and 5.3) by comparing the DSMC results with theory (Burnett 1935; Chapman & Cowling 1970; Sela & Goldhirsch 1998; Reddy & Alam 2020), thereby uncovering the crucial role of the dilatation ($\nabla \cdot \boldsymbol{u} \neq 0$) on the thermohydrodynamics of Poiseuille-type flows. We conclude this paper in § 6 by summarizing the present results and suggesting possible future extensions.

2. Pressure-driven plane Poiseuille flow via DSMC method

The schematic of the pressure-driven Poiseuille flow is shown in figure 2. The domain is filled with hard spheres of diameter d and mass m. The boundary conditions for the system are periodic along the z-direction, fully diffuse thermal walls at $y = \pm L_y/2$ and constant pressure at $x = \pm L_x/2$. A brief account of the DSMC method (Bird 1994), a stochastic algorithm to solve the Boltzmann equation, is provided in Appendix A.

2.1. *Implementation of inlet and outlet conditions*

The main challenge of extending the acceleration-driven Poiseuille flow to the pressure-driven Poiseuille flow is to impose the constant pressure inlet and outlet boundary conditions at the particle level which is non-trivial. Following Zheng *et al.* (2002), we add a layer of ghost cells on either side of the simulation domain along the x-direction to act as infinite reservoirs as shown schematically in figure 2. After the streaming stage in every time step the particles in these ghost cells are deleted and the required number of particles N_{req}, calculated from $\rho_\pm$ (see figure 2), are generated uniformly in the ghost cells and their velocities are sampled from a Gaussian with mean equal to the average velocities in their adjacent cells in the x-directions and a standard distribution of $\sqrt{k_B T_\pm / m}$. This ensures that the inlet and outlet of the system are maintained at the specified states.

Downloaded from https://www.cambridge.org/core. IP address: 3.144.47.8, on 13 Nov 2024 at 06:58:59, subject to the Cambridge Core terms of use, available at https://www.cambridge.org/core/terms. https://doi.org/10.1017/jfm.2024.681

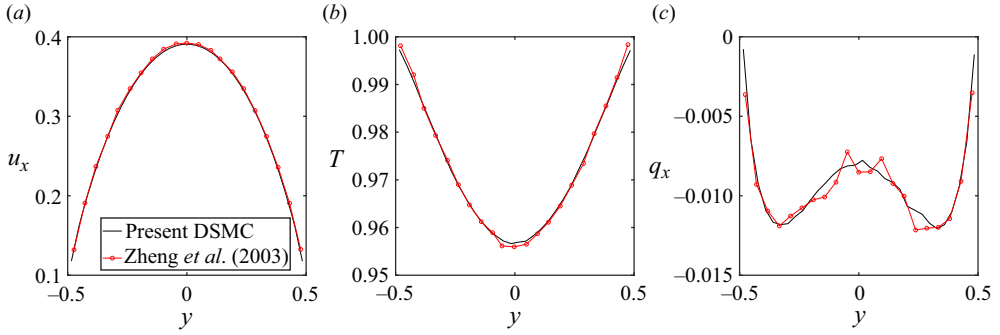

Figure 3. Transverse profiles of the dimensionless (*a*) streamwise velocity $u_x(x = 0, y)$, (*b*) temperature $T(x = 0, y)$ and (*c*) tangential heat flux $q_x(x = 0, y)$ at the midchannel ($x = 0$), with parameter values of $Kn = 0.1$, $\delta p/p_0 = 1$ and $AR = L_x/L_y = 3$; see the last paragraph in § 2.3 for the reference scales for dimensionless fields. The red-circled lines denote the data of Zheng *et al.* (2002) for the same pressure-driven Poiseuille flow.

The calculation of the mean pressure $p_0 = p_{av}$, the mean density $\rho_0 = \rho_{av}$ and other inlet and outlet quantities are done using the relations listed in figure 2. For example, the derivative conditions on the velocity $\partial v_{\pm}/\partial x$ correspond to the DSMC conditions of $v_+ \to v_{+1} \equiv v_{in}$ and $v_- \to v_{-1} \equiv v_{out}$ at the inlet and outlet, respectively.

The implementation of inlet and outlet conditions also produces noisier data compared with its acceleration-driven counterpart. To resolve this issue, we follow a two-step algorithm. First, we run the code with $N = O(10^5)$ number of computational particles for a shorter period of time with the average velocities in the adjacent cells taken to be a running average of the past 50 time steps. This is done to obtain the steady state inlet and outlet velocities since the velocity is a first-order moment and converges faster even with a fewer number of particles $N = O(10^5)$. The code is then run again with larger $N = O(10^6)$ with the inlet and outlet velocities, which are used as the mean for the Gaussian from which the generated particles are sampled, being taken from the previous run (step 1). The results of this two-step procedure are shown in figure 3, which confirms smoother profiles of hydrodynamic fields (especially the higher-order quantities, such as the tangential heat flux q_x and temperature T) than those presented by Zheng *et al.* (2002). It may be noted that the particle–wall collisions are modelled as those of fully 'diffuse' thermal-wall (Bird 1994; Mansour *et al.* 1997; Pöschel & Schwager 2005; Gupta & Alam 2017) boundary conditions for both pressure-driven and acceleration-driven flows, see Appendix A for details.

Since the hydrodynamic fields in the pressure-driven case vary in both the longitudinal (streamwise) and transverse (cross-stream) directions, we need to have collision cells and averaging cells in two directions, leading to increased computing time. To tackle this issue the code is parallelized by dividing the domain into a number of subdomains, which is equal to the number of processing cores the code is intended to run on. The streaming (including the implementation of the boundary conditions) and collision of particles in different subdomains is carried out simultaneously, and the information of the particles that leave or enter the subdomain is communicated amongst the cores using a message passing interface. The parallelized version of this code is used to run the simulations on the ParamYukti supercomputing cluster at the Jawaharlal Nehru Centre for Advanced Scientific Research (JNCASR).

Downloaded from https://www.cambridge.org/core. IP address: 3.144.47.8, on 13 Nov 2024 at 06:58:59, subject to the Cambridge Core terms of use, available at https://www.cambridge.org/core/terms. https://doi.org/10.1017/jfm.2024.681

2.2. *Hydrodynamic and flux fields, and the averaging procedure*

Referring to figure 2, the flow domain ($L_x \times L_y \times L_z$) is divided into a number of cells, each of size $\delta_x \times \delta_y \times \delta_z$, where δ_x, δ_y and δ_z are the dimensions of the cell along the x-, y- and z-directions, respectively; note that the 'collision' cells and the 'averaging' cells are taken to be identical. The macroscopic average of a particle level quantity $\psi(v)$ in a given cell is defined as

$$\langle \psi(\boldsymbol{v}) \rangle_{x,y,z} = \frac{1}{N_t} \sum_{t}^{N_t} \frac{1}{V_c} \sum_{i \in cell} \psi(\boldsymbol{v}_i(t)), \tag{2.1}$$

where $V_c = \delta_x \delta_y \delta_z$ is the volume of the cell and N_t is the number of snapshots over which the quantity is averaged. Since the pressure-driven Poiseuille flow is invariant along the periodic z-direction, we obtain two-dimensional fields of the macroscopic quantities by considering a single cell ($\delta_z = L_z$) in the z-direction. The density, velocity and temperature are defined via (Mansour *et al.* 1997; Uribe & Garcia 1999)

$$\rho(x, y) = \langle m \rangle_{x,y}\,, \tag{2.2}$$

$$\boldsymbol{u}(x, y) = \frac{1}{\rho(x, y)} \langle m\boldsymbol{v} \rangle_{x,y}\,, \tag{2.3}$$

$$T(x, y) = \frac{m}{3k_B \rho(x, y)} \left\langle (\boldsymbol{v} - \boldsymbol{u})^2 \right\rangle_{x,y}\,, \tag{2.4}$$

which are obtained by setting $\psi(v) = (m, m\boldsymbol{v}, m(\boldsymbol{v} - \boldsymbol{u})^2/3k_B)$ in (2.1). The stress tensor and heat flux vector are accordingly obtained from

$$\boldsymbol{P}(x, y) = \langle m(\boldsymbol{v} - \boldsymbol{u})(\boldsymbol{v} - \boldsymbol{u}) \rangle_{x,y}\,, \tag{2.5}$$

$$\boldsymbol{q}(x, y) = \tfrac{1}{2} \left\langle m(\boldsymbol{v} - \boldsymbol{u})^2 (\boldsymbol{v} - \boldsymbol{u}) \right\rangle_{x,y}\,. \tag{2.6}$$

Note that the trace of the stress tensor divided by the number of dimensions, $p = (P_{xx} + P_{yy} + P_{zz})/3$, yields the expression for pressure.

The averaging of the hydrodynamic and flux fields, as defined in (2.1), is carried out over multiple snapshots of the system once the system has reached a steady state. The steady state is determined by checking the constancy of the average kinetic energy per particle ($E/N = \sum_i m v_i^2/2N$) in the system, see figure 4(*a*). Another issue is the maintenance of the inlet (p_+) and outlet (p_-) values of the pressure which can be verified from figure 4(*b*) that displays the streamwise variation of the pressure, $p(x, 0)$, at the middle of the channel ($y = 0$) – it is clear that $p_+/p_0 \approx 1.5$ and $p_-/p_0 \approx 0.5$ as imposed in simulations (*viz.* figure 2). In addition to validating the present code to correctly reproduce the previous simulation results (Zheng *et al.* 2002) on the pressure-driven Poiseuille flow in figure 3, the same DSMC code was further validated to simulate acceleration-driven Poiseuille flow and the planar Couette flow of rarefied gases.

2.3. *Control parameters and reference scales*

The main control parameter is the 'global' Knudsen number,

$$Kn = \frac{l_f}{L_y} = \frac{1}{\sqrt{2}\pi d^2 n_0 L_y}, \tag{2.7}$$

which is varied in the range of $0.01 \leq Kn \leq 100$ by changing the mean free path $l_f = 1/(\sqrt{2}\pi n_0 d^2)$ via changing the reference density $\rho_0 = m n_0 = \rho_{av}$ while keeping the

Downloaded from https://www.cambridge.org/core. IP address: 3.144.47.8, on 13 Nov 2024 at 06:58:59, subject to the Cambridge Core terms of use, available at https://www.cambridge.org/core/terms. https://doi.org/10.1017/jfm.2024.681

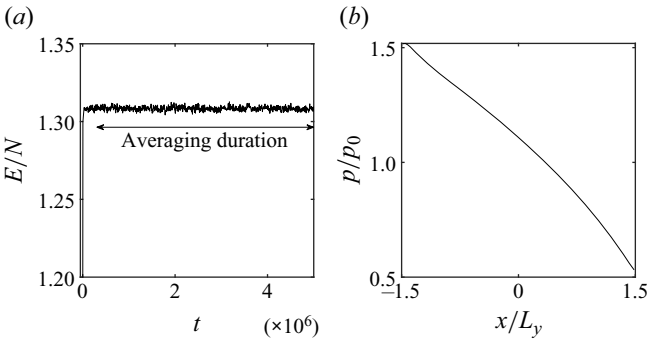

Figure 4. (*a*) Average kinetic energy per particle, $E/N = \sum_i mv_i^2/N$, versus time and (*b*) the axial variation of the pressure $p(x, 0)$ at midchannel $y = 0$. Parameter values are as in figure 3.

channel width L_y constant. The inlet and outlet pressures p_+ and p_- are set as

$$p_+ = p_0 + \frac{\delta p}{2} \quad \text{and} \quad p_- = p_0 - \frac{\delta p}{2}, \tag{2.8a,b}$$

such that

$$p_+ - p_- = \delta p \quad \text{and} \quad \tfrac{1}{2}\,(p_+ + p_-) = p_0 \tag{2.9a,b}$$

refer to the pressure difference and the mean pressure, respectively, see figure 2.

For most of the presented results, the pressure difference is set to $\delta p = p_0$, which has been chosen such that the forcing terms in (i) the acceleration-driven case $\rho_0 a$ and (ii) the pressure-driven case $\mathrm{d}p/\mathrm{d}x \approx \delta p/L_x$ are of the same magnitude for a meaningful comparison between the results of the two sets of studies. We have verified that $1.3 \times 10^{-6} \geq \rho_0 a \geq 1.3 \times 10^{-10}$ and $1.08 \times 10^{-6} \geq \mathrm{d}p/\mathrm{d}x \geq 1.08 \times 10^{-10}$ for the range of Knudsen numbers $0.01 \leq Kn \leq 100$, and the forcing terms for four values of Kn are shown in table 1. The dimensionless acceleration (Tij & Santos 1994; Mansour *et al.* 1997; Aoki *et al.* 2002; Gupta & Alam 2017; Alam *et al.* 2021) is defined as

$$\hat{a} = \frac{aL_y}{2k_B T_w/m}, \tag{2.10}$$

which is a measure of the strength of the flow and represents the body force acting on a gas molecule travelling a distance L_y; the numerical value of $\hat{a} = 0.1$ has been chosen for a comparison with the pressure-driven case with $\delta p/p_0 = 1$. Note that the acceleration-driven flow belongs to the linearized and nonlinear regimes for $\hat{a} \ll 1$ and $O(1)$, respectively. We refer to Appendix B for related details on the local values of the Knudsen number ($Kn(x, y)$), Mach number ($Ma(x, y)$) and Reynolds number ($Re(x, y)$) for both forcings.

The mass and the diameter of the atoms/particles are taken to be unity ($m = d = 1$), the Boltzmann constant is taken as $k_B = 0.5$ and the wall temperature is $T_w = T_0 = 1$. The width of the channel is fixed as $L_y = 1860d$ in most simulations; to study the effect of the channel aspect ratio ($AR = L_x/L_y$), the length of the channel (L_x) is increased keeping its width constant such that $3 \leq AR \leq 27$. The effect of pressure gradient is studied by changing the pressure difference ($0.1 \leq \delta p/p_0 \leq 1$) by a factor of 10. All results are presented in dimensionless form: the density is normalized by $\rho_0 = \rho_{av}$, the temperature by $T_0 = T_w$, the velocity by $u_0 = \sqrt{2k_B T_0/m}$, the pressure and stresses by $p_0 = (p_+ + p_-)/2 = p_{av}$ and the heat fluxes by $\rho_0 u_0^3/2$. The lengths are rescaled by

Downloaded from https://www.cambridge.org/core. IP address: 3.144.47.8, on 13 Nov 2024 at 06:58:59, subject to the Cambridge Core terms of use, available at https://www.cambridge.org/core/terms. https://doi.org/10.1017/jfm.2024.681

Kn	$\rho_0 a$	$\mathrm{d}p/\mathrm{d}x$	p_0	ρ_0
0.05	2.6×10^{-7}	2.1×10^{-7}	1.21×10^{-3}	2.42×10^{-3}
0.5	2.6×10^{-8}	2.1×10^{-8}	1.21×10^{-4}	2.42×10^{-4}
5	2.6×10^{-9}	2.1×10^{-9}	1.21×10^{-5}	2.42×10^{-5}
50	2.6×10^{-10}	2.1×10^{-10}	1.21×10^{-6}	2.42×10^{-6}

Table 1. Comparison of the forcing terms ($\rho_0 a$ and $\mathrm{d}p/\mathrm{d}x$) for various Knudsen number (Kn) corresponding to (i) a pressure-difference of $\delta p = p_0$ (and the pressure-gradient is $\mathrm{d}p/\mathrm{d}x = \delta p/L_x$) in the pressure-driven Poiseuille flow and (ii) a dimensionless acceleration (2.10) of $\hat{a} = 0.1$ in the acceleration-driven Poiseuille flow. The width and length of the channel are $L_y/d = 1860$ and $L_x/d = 5580$, respectively, with aspect ratio $AR = L_x/L_y = 3$.

the channel width L_y such that the streamwise and wall-normal ranges are given by $-AR/2 \leq x/L_y \leq AR/2$ and $-0.5 \leq y/L_y \leq 0.5$, respectively.

3. Hydrodynamics, mass-flow rate and the role of dilatation

We start with presenting results on the velocity field and the mass flow rate in § 3.1, followed by the analyses of (i) the velocity gradient tensor in § 3.3.1 and (ii) the pressure, density and temperature fields in § 3.2. The equivalence between the two forcing (pressure gradient and acceleration) to realize NSF-order hydrodynamic fields is discussed in § 3.3.2.

3.1. *Velocity field and the mass flow rate*

The contour plots of the streamwise velocity $u_x(x, y)$ and the local mass flux $\rho(x, y)u_x(x, y)$ are displayed in figures 5(*a*) and 5(*b*), respectively, at a Knudsen number of $Kn = 0.05$. It is seen that while the streamwise velocity u_x (figure 5*a*) increases along the length of the channel (and hence the flow is developing and steady), the local mass-flux ρu_x (figure 5*b*,*d*) also varies slightly along the length of the channel. The effect of rarefaction (Kn) on the transverse and axial profiles of the local mass flux $\rho(x, y)u_x(x, y)$ at $x = 0$ and $y = 0$, respectively, can be understood from figures 5(*c*) and 5(*d*). It is seen that the local mass flux decreases with increasing Kn but seems to saturate beyond a critical value of Kn; the latter can be appreciated from the curves representing $Kn = 5$ (blue dot–dashed line) and 50 (magenta dotted line) that are almost indistinguishable from each other.

That the pressure-driven Poiseuille flow of a gas is not fully developed (*viz.* figure 5*a*; see also the discussion in § 3.3.1) and the local mass flux $\rho(x, y)u_x(x, y)$ (*viz.* figure 5*d*) varies axially suggest that the wall-normal velocity $u_y(x, y)$ must be finite as dictated by the continuity equation

$$\frac{\partial \rho u_x}{\partial x} + \frac{\partial \rho u_y}{\partial y} = 0. \tag{3.1}$$

This is confirmed in figures 6(*a*) and 6(*b*), which display the contour plots of $u_y(x, y)$ and $\rho(x, y)u_y(x, y)$, respectively. Ignoring entrance and exit effects, we observe that both the streamwise and wall-normal velocities vary monotonically along the length of the channel. The effect of Kn on the transverse profiles of the wall-normal velocity $u_y(0, y)$ at the midchannel ($x = 0$) is shown in figure 6(*c*). The wall-normal velocity profiles closely resemble sine waves, irrespective of the value of Kn; its amplitude ($\delta u_y = u_y^{max} - u_y(0)$), which is an order smaller compared with the magnitudes of u_x, decreases with increase in Kn, see figure 6(*d*), and appears to saturate to a constant value at large enough $Kn \gg 1$.

Downloaded from https://www.cambridge.org/core. IP address: 3.144.47.8, on 13 Nov 2024 at 06:58:59, subject to the Cambridge Core terms of use, available at https://www.cambridge.org/core/terms. https://doi.org/10.1017/jfm.2024.681

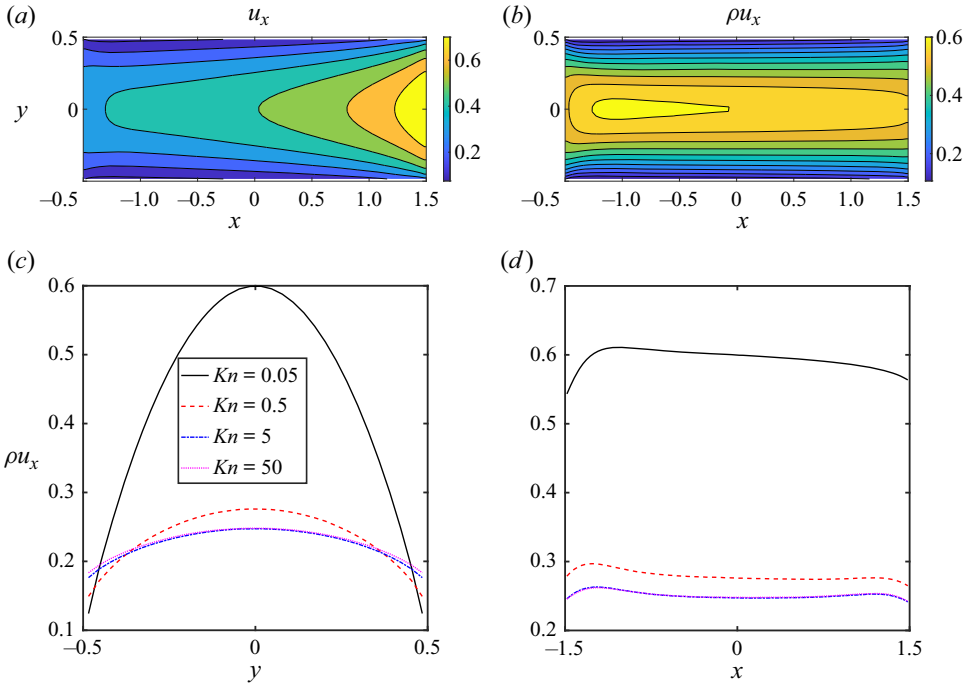

Figure 5. (*a*,*b*) Contour plots of (*a*) streamwise velocity $u_x(x, y)$ and (*b*) local mass flux $\rho(x, y)u_x(x, y)$ at $Kn = 0.05$. (*c*,*d*) Variations of (*c*) $\rho(0, y)u_x(0, y)$ at $x = 0$ and (*d*) $\rho(x, 0)u_x(x, 0)$ at $y = 0$ for different values of Kn. Parameter values are as in figure 3.

From the contour plots of ρu_x such as in figure 5(*b*), the mass flow rate of the gas is calculated using

$$\mathcal{M}(Kn) = \frac{1}{\rho_0 u_0} \int_{-0.5}^{0.5} \rho(x, y)u_x(x, y)\, \mathrm{d}y, \tag{3.2}$$

where ρ_0 is the average density and $u_0 = \sqrt{2k_B T_0/m}$ is the most probable velocity. Since $\mathcal{M}$ is invariant of the streamwise location, (3.2) can be evaluated at any cross-section such as integrating the transverse profiles in figure 5(*c*). The variation of $\mathcal{M}$ with Kn is shown in figure 7(*a*) for the pressure-driven case with a dimensionless pressure-difference of $\delta p/p_0 = 1$. It is seen that while the mass flow rate decreases sharply with increasing Kn, there is indeed a minimum in $\mathcal{M}$ at $Kn \approx O(1)$ as evident in the inset of figure 7(*a*). Comparing figure 7(*a*) with its acceleration-driven counterpart in figure 7(*b*), we find that the mass flow rate saturates to a constant value at $Kn \gg 1$ in the pressure-driven case in contrast to its slow logarithmic increase $\mathcal{M} \sim \log Kn$ in the latter.

For a finite-length ($L_x < \infty$) channel with width L_y, there is an upper bound on the Knudsen number $Kn_{\max} = L_x/L_y$ beyond which the particles would rarely collide with two lateral walls before reaching the exit of the channel, and hence the gas would flow freely without wall collisions, resulting in a saturation of $\mathcal{M}(Kn, L_x) \to$ constant at $Kn \gg AR$. This trend is indeed captured in the main panel and the inset of figure 8(*a*) that show the variations of $\mathcal{M}(Kn, L_x)$ with Kn for three different channel lengths ($L_x/d = 5580$, 16 740 and 50 220), with parameter values as in table 2. It is clear from the inset that the range of Kn over which the logarithmic scaling $\mathcal{M} \propto \log Kn$ holds increases with increasing L_x and $\mathcal{M}(Kn, L_x)$ saturates to some constant value for a specified L_x; the asymptotic

Downloaded from https://www.cambridge.org/core. IP address: 3.144.47.8, on 13 Nov 2024 at 06:58:59, subject to the Cambridge Core terms of use, available at https://www.cambridge.org/core/terms. https://doi.org/10.1017/jfm.2024.681

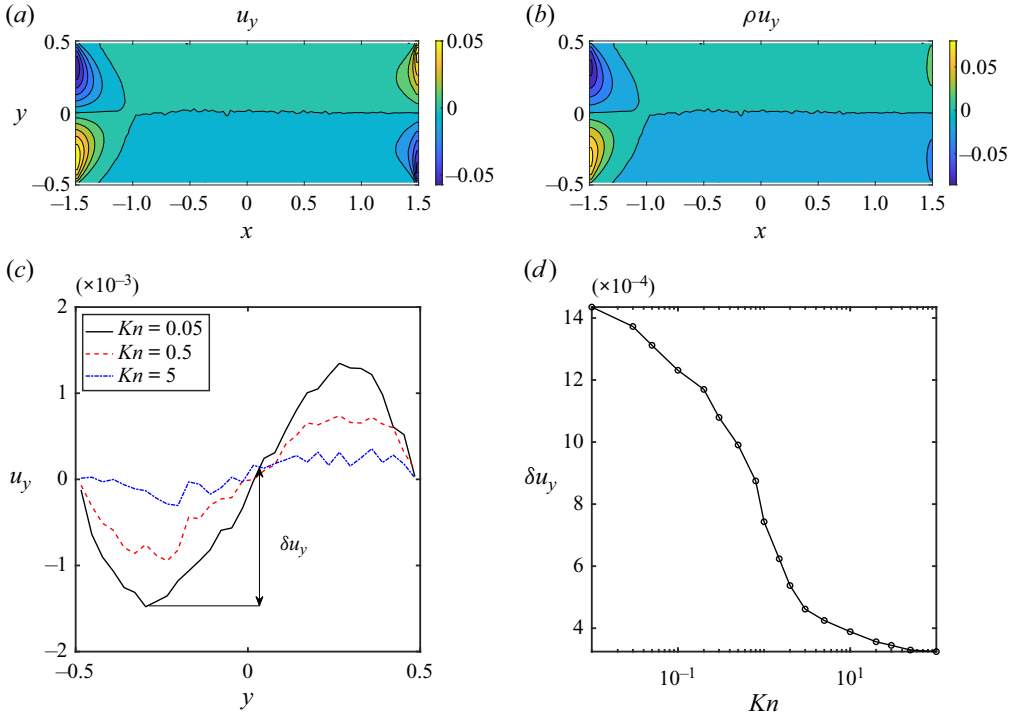

Figure 6. (*a*,*b*) Contour plots of (*a*) the wall-normal velocity $u_y(x, y)$ and (*b*) $\rho(x, y)u_y(x, y)$ for $Kn = 0.05$. (*c*,*d*) Cross-stream variations of the wall-normal velocity $u_y(0, y)$ and (*d*) $\delta u_y = \max|u_y(0, y)|$ with Kn. Other parameter values as in figure 5.

logarithmic branch of $\mathcal{M}(Kn, L_x)$ is expected to be recovered only in an infinite-length ($L_x \to \infty$) channel. The recent experimental data of Kunze *et al.* (2023) support these overall findings, see figure 8(*b*). This dependence of $\mathcal{M}$ on the length scales of the channel is also in agreement with the theoretical predictions of Raghuraman & Willis (1977) and Cercignani (1979) based on the linearized Boltzmann–BGK equation. Therefore, we conclude that the scale-dependence and the saturation of $\mathcal{M}(Kn \to \infty, L_x)$ in the pressure-driven Poiseuille flow is due to the finite length of the channel.

3.2. *Pressure, density and temperature: dilatation-driven effects?*

In this section we seek answers to the following questions in the context of the pressure-driven Poiseuille flow of a rarefied gas. (i) Are the axial variations of pressure and density linear as assumed in theoretical analyses (Cercignani & Daneri 1963; Raghuraman & Willis 1977; Cercignani 1979; Takata & Funagane 2011)? (ii) Can the gas be approximated as isothermal (at least in terms of the axial variation) of temperature? (iii) Is the temperature profile $T(y)$ of bimodal shape (as in the case of acceleration-driven Poiseuille flow) at $Kn \sim 0$ for small enough values of the pressure gradient?

The contour plots of pressure $p(x, y)$, density $\rho(x, y)$ and temperature $T(x, y)$ are displayed in figure 9, with figure 9(*a*,*c*,*e*) and figure 9(*b*,*d*,*f*) referring to $Kn = 0.05$ and 0.5, respectively; the channel width is $L_y/d = 1860$, with an aspect ratio of $AR = L_x/L_y = 3$ and a normalized pressure difference of $\delta p/p_0 = 1$. There are noticeable variations in pressure, density and temperature along both streamwise (x)

Downloaded from https://www.cambridge.org/core. IP address: 3.144.47.8, on 13 Nov 2024 at 06:58:59, subject to the Cambridge Core terms of use, available at https://www.cambridge.org/core/terms. https://doi.org/10.1017/jfm.2024.681

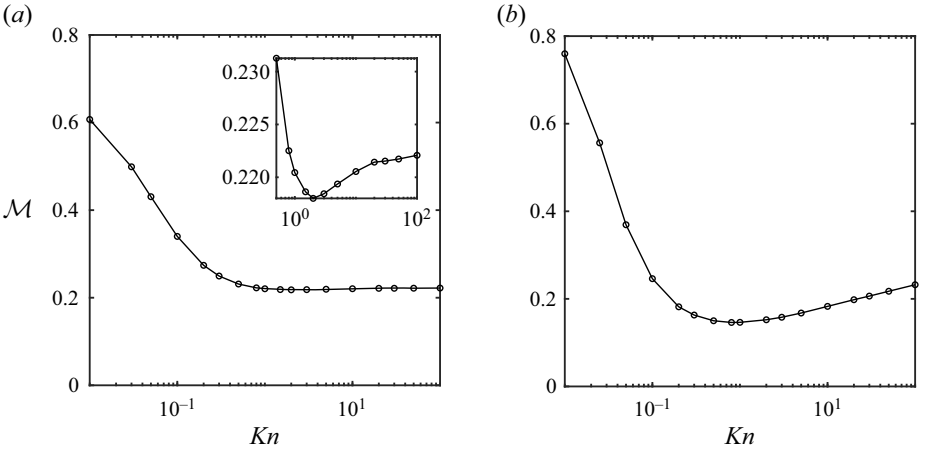

Figure 7. Variation of the mass flow rate $\mathcal{M}$ with Knudsen number Kn for (a) pressure-driven Poiseuille flow with $\delta p/p_0 = 1$ (and $p_0 = 6.05 \times 10^{-4}$) and $AR = L_x/L_y = 3$ and (b) acceleration-driven Poiseuille flow with $\hat{a} = 0.1$. For both cases, the channel width is $L_y/d = 1860$.

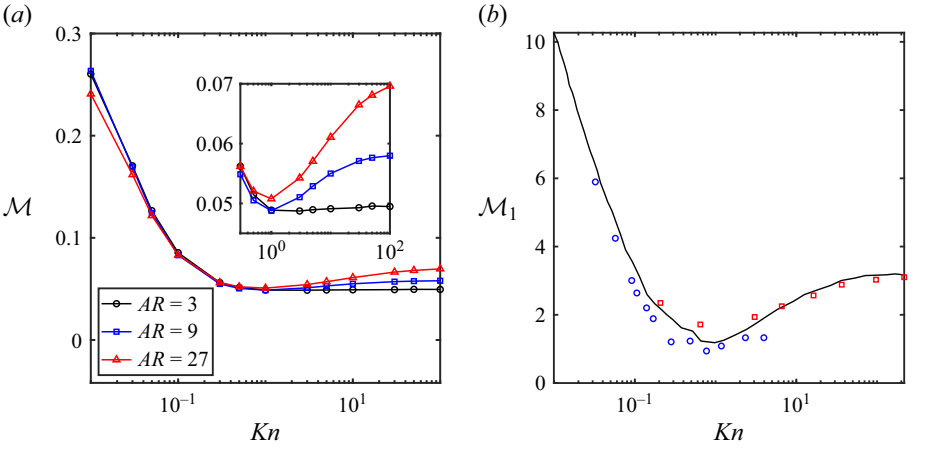

Figure 8. (a) Effect of channel-length on the mass flow rate $\mathcal{M}$: $L_x/d = 5580$ ($AR = 3$, $\Delta p/p_0 = 0.2$; black circles line), $L_x/d = 16740$ ($AR = 9$, $\delta p/p_0 = 0.6$; blue squares line) and $L_x/d = 50\,220$ ($AR = 27$, $\delta p/p_0 = 1.8$; red triangles line). For all cases, the dimensionless pressure-gradient is kept fixed at $G_p = (\delta p/p_0)/(L_x/L_y) = 1/15$, with $p_0 = 6.05 \times 10^{-4}$ and the channel width $L_y/d = 1860$, see table 2. (b) Saturation of $\mathcal{M}$ (in arbitrary unit) at $Kn \gg 1$ in a finite-length channel, adapted from Kunze *et al.* (2023); the symbols and the solid line represent the experimental data (blue circles and red squares denote data for *He* in short and long channels, respectively) and their model prediction, respectively.

Aspect ratio	L_y/d	L_x/d	p_0	$\delta p/p_0$	$G_p = (\delta p/p_0)/(L_x/L_y)$	p_{in}/p_{out}
3	1860	5580	6.05×10^{-4}	0.2	1/15	1.222
9	1860	16 740	6.05×10^{-4}	0.6	1/15	1.857
27	1860	50 220	6.05×10^{-4}	1.8	1/15	19.00

Table 2. Parameter values for changing the aspect ratio ($AR = L_x/L_y$) by increasing the length (L_x) of the channel.

Downloaded from https://www.cambridge.org/core. IP address: 3.144.47.8, on 13 Nov 2024 at 06:58:59, subject to the Cambridge Core terms of use, available at https://www.cambridge.org/core/terms. https://doi.org/10.1017/jfm.2024.681

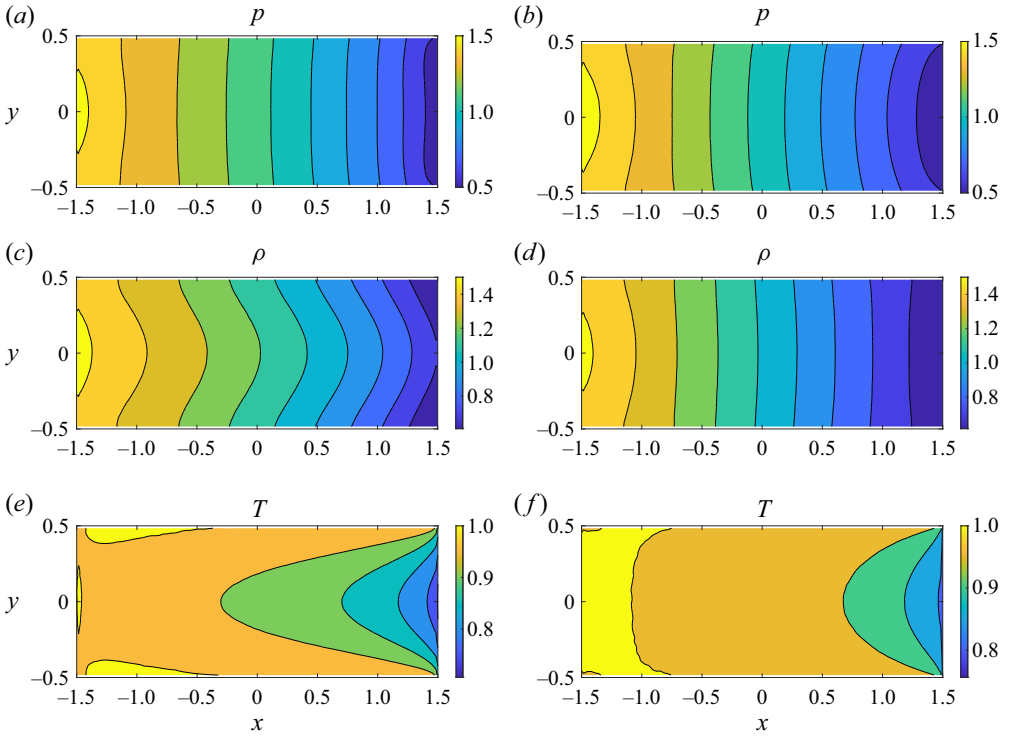

Figure 9. Contour plots of (*a*,*b*) pressure $p(x, y)$, (*c*,*d*) density $\rho(x, y)$ and (*e*,*f*) temperature $T(x, y)$ for (*a*,*c*,*e*) $Kn = 0.05$ and (*b*,*d*,*f*) $Kn = 0.5$; other parameter values as in figure 5.

and cross-stream (y) directions. The streamwise variations of $(p(x, 0), \rho(x, 0), T(x, 0))$ and their gradients $\mathrm{d}/\mathrm{d}x(p(x, 0), \rho(x, 0), T(x, 0))$ are shown in figure 10(*a–c*) and figure 10(*d–f*), respectively. Figure 10(*a*) confirms that the inlet and outlet pressures are indeed $p_+ = 1.5p_0$ and $p_- = 0.5p_0$, respectively, irrespective of the value of Kn. Looking at figure 10(*a*,*b*) we find that the axial decay of both $p(x, 0)$ and $\rho(x, 0)$ are approximately linear in the bulk of the channel (except near the entrance and exit of the channel, see their axial gradients in figure 10*d*,*e*) at $Kn \geq 0.5$, but become nonlinear at smaller values of the Knudsen number $Kn = 0.05$. Figure 10(*c*,*f*) illustrates that the temperature of the gas also decreases axially irrespective of the value of Kn, but its decay rate is milder (compared with pressure and density) in the bulk of the channel with a relatively sharper decay near the exit of the channel. These overall findings on the effect of Kn remain robust irrespective of the choice of the length of the channel (not shown).

3.2.1. *Effect of imposed pressure gradient*

By fixing the channel aspect ratio at $AR = L_x/L_y = 3$, but decreasing the magnitude of the pressure gradient makes the pressure and density variations with x increasingly linear even at smaller values of $Kn = 0.1$, see figure 11(*a*,*b*). Comparing the data for cases C (blue dot–dashed line) and D (dotted magenta line) in figure 11(*c*,*f*), we find that the axial variation of temperature $T(x, 0)$ can be made very small by decreasing the value of the imposed pressure gradient; the corresponding axial gradients in pressure ($\mathrm{d}p/\mathrm{d}x$) and density ($\mathrm{d}\rho/\mathrm{d}x$) become nearly independent of x as marked by the blue and magenta lines

Downloaded from https://www.cambridge.org/core. IP address: 3.144.47.8, on 13 Nov 2024 at 06:58:59, subject to the Cambridge Core terms of use, available at https://www.cambridge.org/core/terms. https://doi.org/10.1017/jfm.2024.681

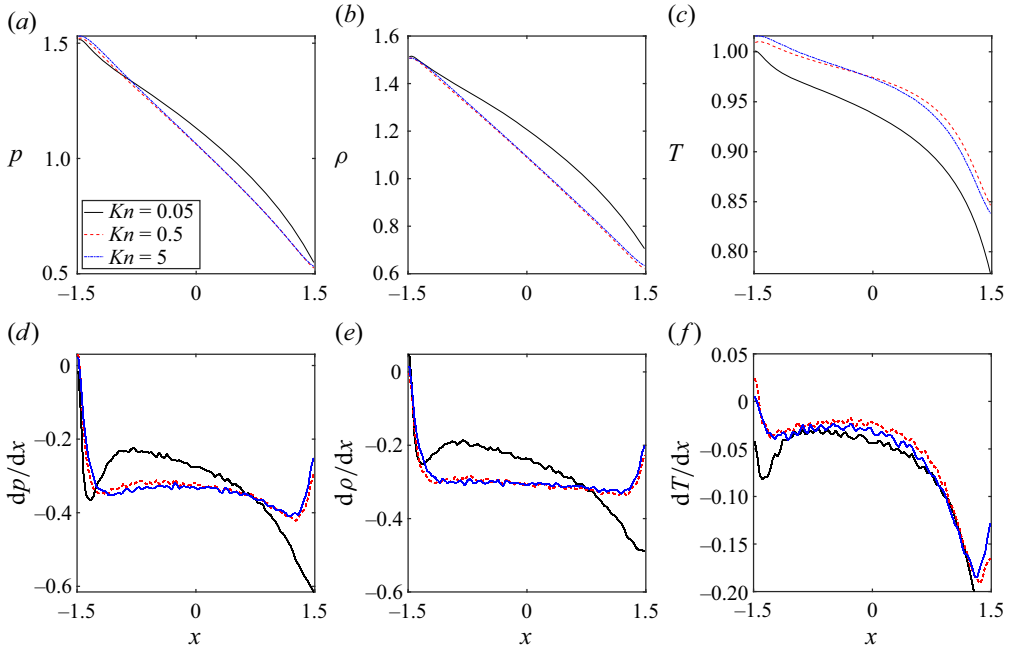

Figure 10. Effects of Knudsen number on streamwise variations of (*a*) $p(x, 0)$, (*b*) $\rho(x, 0)$ and (*c*) $T(x, 0)$ along $y = 0$ line and (*d–f*) their gradients (*d*) $\mathrm{d}p(x, 0)/\mathrm{d}x$, (*e*) $\mathrm{d}\rho(x, 0)/\mathrm{d}x$ and (*f*) $\mathrm{d}T(x, 0)/\mathrm{d}x$; parameter values as in figure 9.

in figures 11(*d*) and 11(*e*), respectively. Therefore, the axial variation of the gas temperature can be made arbitrarily small at small enough values of the imposed (dimensionless) pressure gradient,

$$G_p = \frac{\mathrm{d}(p/p_0)}{\mathrm{d}(x/L_y)} \approx \left(\frac{\delta p}{p_0}\right) \Big/ \left(\frac{L_x}{L_y}\right) \sim G_\rho \ll 1, \tag{3.3}$$

yielding a nearly linear decay of both pressure $p(x, 0)$ and density $\rho(x, 0)$,

$$p(x) = p_0(1 - G_p x) + O(G_p^2) \quad \text{and} \quad \rho(x) = \rho_0(1 - G_\rho x) + O(G_\rho^2) \tag{3.4a,b}$$

along the channel length. It may be recalled that the kinetic theory analysis of Cercignani (1979) is built around the ansatz (3.4*a*,*b*), along with additional assumptions that the transverse variations of both pressure and density are negligible, i.e.

$$p(x, y) \equiv p(x) \quad \text{and} \quad \rho(x, y) \equiv \rho(x), \tag{3.5a,b}$$

at the leading order $O(G_p)$ that correctly predicted the dependence of the mass flow rate on the channel length such as in figure 8(*a*). Therefore, the mapping '$G_p \leftrightarrow \hat{a}$' between the two flows (replacing the pressure gradient by the acceleration in the limit of $G_p \ll 1$) would hold that recovers the logarithmic branch of $\mathcal{M}(Kn, L_x) \sim \log Kn$ in an infinite channel of infinite length ($L_x \to \infty$).

Figure 12(*a–c*) show the transverse profiles of pressure $p(0, y)$, density $\rho(0, y)$ and temperature $T(0, y)$ for three values of the Knudsen number $Kn = 0.05$ (black line), 0.5 (dashed magenta line) and 5 (dot–dashed blue line), with $\delta p/p_0 = 1$ and other parameters as in figure 10. It is seen that while both the pressure and temperature profiles are of

Downloaded from https://www.cambridge.org/core. IP address: 3.144.47.8, on 13 Nov 2024 at 06:58:59, subject to the Cambridge Core terms of use, available at https://www.cambridge.org/core/terms. https://doi.org/10.1017/jfm.2024.681

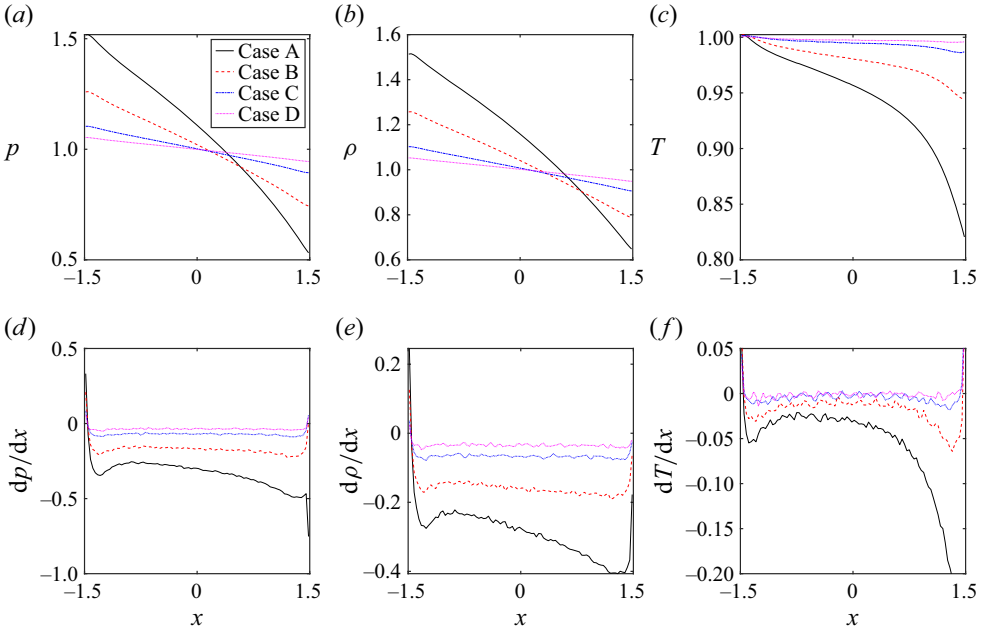

Figure 11. Effect of imposed pressure gradient on the streamwise variations of (*a*) $p(x, 0)$, (*b*) $\rho(x, 0)$ and (*c*) $T(x, 0)$ and (*d–f*) their gradients (*d*) $\mathrm{d}p(x, 0)/\mathrm{d}x$, (*e*) $\mathrm{d}\rho(x, 0)/\mathrm{d}x$ and (*f*) $\mathrm{d}T(x, 0)/\mathrm{d}x$; parameters are listed in table 3 with $Kn = 0.1$ and $AR = 3$.

Case	$\delta p/p_0$	$G_p = (\delta p/p_0)/(L_x/L_y)$	$(\delta p/p_0)/(L_x/d)$	$Ma(0, 0)$	$Re(0, 0)$
A	1	1/3	1.79×10^{-4}	0.43	8.20
B	0.5	1/6	8.95×10^{-5}	0.27	4.70
C	0.2	1/15	3.58×10^{-5}	0.12	1.99
D	0.1	1/30	1.79×10^{-5}	0.06	1.02

Table 3. Protocols for changing the pressure difference for $Kn = 0.1$, $AR = L_x/L_y = 3$ and $L_y/d = 1860$.

convex-up shape around the channel centreline, the density profiles are convex down at any *Kn*. All profiles become flatter with increasing *Kn*. For a comparison, we display the corresponding profiles of $(p(y), \rho(y), T(y))$ in figure 12(*d–f*) in the acceleration-driven Poiseuille flow for a dimensionless acceleration of $\hat{a} = 0.1$.

The first difference we encounter in figure 12 is about the shape of the temperature profile at small values of *Kn*: $T(y)$ at $Kn = 0.05$ is of bimodal structure in the acceleration-driven flow (figure 12*f*), with a local minimum of temperature at $y = 0$ and two local maxima symmetrically located away from the channel centre, in contrast to the convex-up temperature profiles that persist at all *Kn* in its pressure-driven counterpart (figure 12*c*). The close-up version in the inset of figure 12(*f*) clearly identifies the locations of temperature minima and maxima for the case of $Kn = 0.05$. The pressure profiles in figure 12(*a*,*d*) possess similar characteristic features as those of the temperature profiles in figure 12(*c*,*f*). It is known from theory (Tij & Santos 1994; Uribe & Garcia 1999; Tij & Santos 2004; Rongali & Alam 2018*a*,*b*) and simulations (Mansour *et al.* 1997; Alam *et al.* 2015; Gupta & Alam 2017, 2018) that the two local maxima in the $T(y)$-profile move

Downloaded from https://www.cambridge.org/core. IP address: 3.144.47.8, on 13 Nov 2024 at 06:58:59, subject to the Cambridge Core terms of use, available at https://www.cambridge.org/core/terms. https://doi.org/10.1017/jfm.2024.681

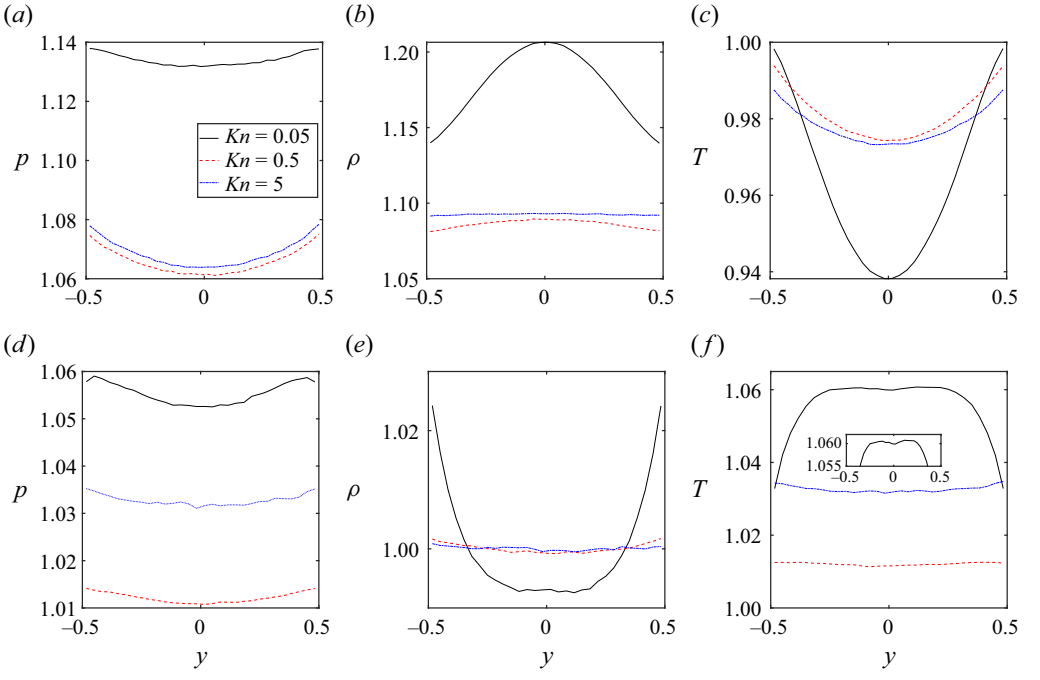

Figure 12. Effects of Knudsen number on the cross-stream variations of (*a*) $p(x = 0, y)$, (*b*) $\rho(0, y)$ and (*c*) $T(0, y)$ in pressure-driven Poiseuille flow with (*a–c*) $\delta p/p_0 = 1.0$. Panels (*d–f*) represent corresponding profiles in acceleration-driven Poiseuille flow with dimensionless acceleration $\hat{a} = 0.1$; the inset in (*f*) shows the close-up version of $T(y)$ for $Kn = 0.05$, clarifying its 'bimodal' shape.

towards the walls with increasing Kn, thereby making a transition from the bimodal-shape to unimodal convex-up shape for both $T(y)$ and $p(y)$ profiles in the acceleration-driven flow at large Kn.

The second difference between the two flows is that while the density profile $\rho(y)$ in the acceleration-driven flow has a minimum at the channel centre (see figure 12*e*), its pressure-driven counterpart admits a density maximum at $y = 0$ in figure 12(*b*). The above differences regarding the role of forcing on the transverse profiles of $(p(y), \rho(y), T(y))$ persist when the imposed pressure gradient is reduced further, see figure 13. For example, the inset in figure 13(*b*) confirms the presence of the convex-down $\rho(y)$-profile even at $\delta p/p_0 = 0.1$ for $Kn = 0.1$. Collectively, figures 12 and 13 underscore the qualitative differences in the shape of the temperature (and density) profiles, depending on whether the flow is generated by an axial pressure gradient or a constant acceleration.

3.2.2. *Energy balance, pressure work and the absence of temperature bimodality*

To check how the underlying assumptions in the two flows may impact the profiles of $(\rho(y), T(y), p(y))$, we consider the steady energy balance equation (in dimensionless form) at the NSF order,

$$\underline{-\rho c_v \left(u_x \frac{\partial T}{\partial x} + u_y \frac{\partial T}{\partial y} \right)} - \boldsymbol{\nabla} \cdot \boldsymbol{q} - \underline{p(\boldsymbol{\nabla} \cdot \boldsymbol{u})} + \Phi_{sh} = 0, \tag{3.6}$$

Downloaded from https://www.cambridge.org/core. IP address: 3.144.47.8, on 13 Nov 2024 at 06:58:59, subject to the Cambridge Core terms of use, available at https://www.cambridge.org/core/terms. https://doi.org/10.1017/jfm.2024.681

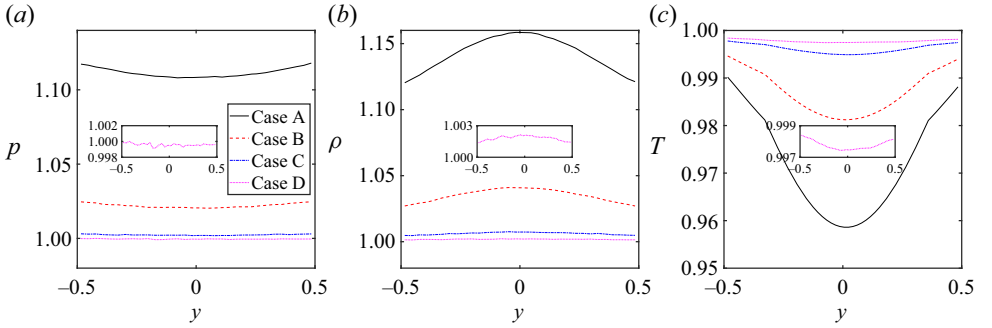

Figure 13. Effects of imposed pressure gradient on cross-stream variations of (*a*) $p(x = 0, y)$, (*b*) $\rho(0, y)$ and (*c*) $T(0, y)$ at $Kn = 0.1$; Case A $\delta p/p_0 = 1$, Case B $\delta p/p_0 = 0.5$, Case C $\delta p/p_0 = 0.2$ and Case D $\delta p/p_0 = 0.1$, see table 3 for other parameters. Insets in (*a–c*) display the close-up version of the Case D.

in which the underlined terms ((i) convective heat transport and (ii) pressure work) are absent in the acceleration-driven Poiseuille flow, and the shear-work term

$$\Phi_{sh} = 2\mu \left(\left(\frac{\partial u_x}{\partial y} \right)^2 + \ldots \right) > 0 \tag{3.7}$$

is positive, representing the shear-induced heating of the gas. Next, we estimate the underlined terms in (3.6) at finite values of Kn around the channel centreline ($y \sim 0$) to ascertain their relative importance compared with the shear work term. At the midchannel $y = 0$, we have $u_y(x, 0) = 0$ and $\partial T/\partial x < 0$ and hence the convective term simplifies to

$$Q_c = -\rho c_v \left(u_x \frac{\partial T}{\partial x} + u_y \frac{\partial T}{\partial y} \right) \Bigg|_{y=0} \equiv -\frac{3}{2} \rho u_x(x, 0) \left(\frac{\partial T}{\partial x} \right) \Bigg|_{y=0} > 0, \tag{3.8}$$

representing a heating effect; the pressure work is given by

$$\Phi_p = -p(\boldsymbol{\nabla} \cdot \boldsymbol{u})|_{y=0} < 0, \tag{3.9}$$

representing a cooling effect. Figure 14(*a*,*b*) verifies that $Q_c > 0$ (figure 14*a*) and $\Phi_p < 0$ (panel *b*) in the bulk of the channel (except at the inlet and outlet of the channel). Furthermore, figure 14(*c*) confirms that the cooling due to pressure work (3.9) dominates over convective heating (3.8) at all Kn, resulting in a net cooling (i.e. $\Phi_p + Q_c < 0$) in the pressure-driven flow. These overall observations hold for transverse variations of $Q_c(0, y)$, $\Phi_p(0, y)$ and $(\Phi_p + Q_c)(0, y)$ too, see figures 14(*d*), 14(*e*) and 14(*f*), respectively. It is clear that the dominance of the pressure work over the convective heating is responsible for the cooling of the gas in the bulk of the channel – this leads to a lower bulk temperature in the pressure-driven case (*viz.* figure 12*c*) compared with its acceleration-driven counterpart (*viz.* figure 12*f*) at $Kn \to 0$. Consequently, the changes in the temperature profile affect the density and pressure profiles (via the equation of state $p = \rho T$) as demonstrated in figure 12(*a*,*b*,*d*,*e*). We conclude that the non-zero values of the terms in (3.8)–(3.9) in the pressure-driven flow are responsible for the different shapes of $(T(y), \rho(y))$ in the two flows even in the continuum limit of $Kn \to 0$ at finite values of G_p and $\hat{a}$.

The foregoing analysis confirms that the absence of the bimodal shape of the temperature in the pressure-driven Poiseuille flow profile at small $Kn \sim 0$ is tied to the cooling afforded by the 'pressure-dilatation' work (3.9) which, however, vanishes in its acceleration-driven counterpart. It must be noted that the temperature bimodality

Downloaded from https://www.cambridge.org/core. IP address: 3.144.47.8, on 13 Nov 2024 at 06:58:59, subject to the Cambridge Core terms of use, available at https://www.cambridge.org/core/terms. https://doi.org/10.1017/jfm.2024.681

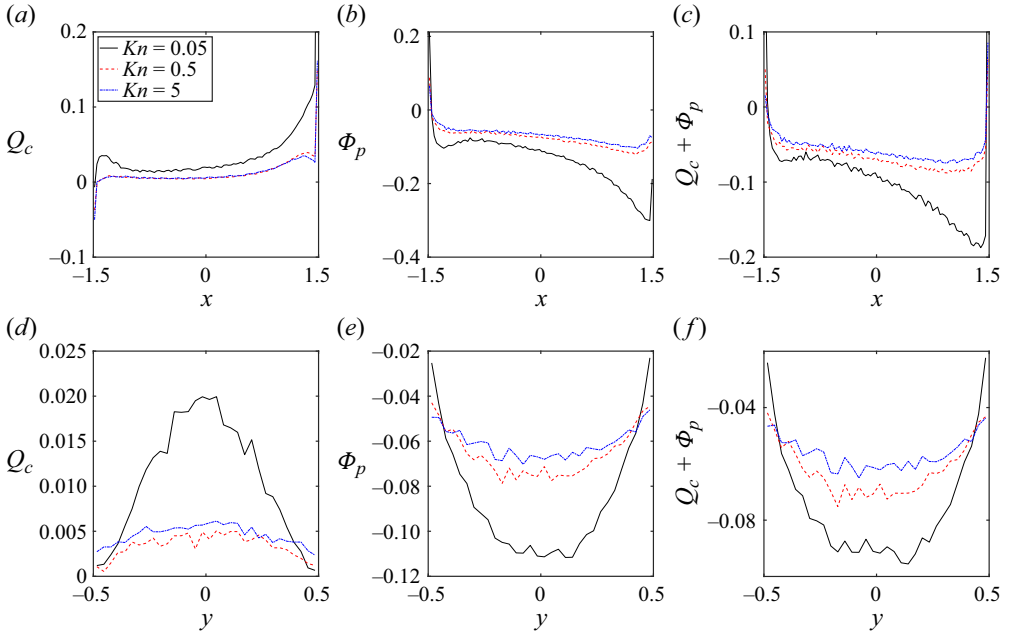

Figure 14. (*a–c*) Axial variations of (*a*) convective heat Q_c (3.8), (*b*) pressure work Φ_p (3.9) and (*c*) $(\Phi_p + Q_c)$ at the midchannel ($y = 0$) for different Kn, with $\delta p/p_0 = 1$ and $AR = 3$. (*d–f*) Same as (*a–c*) but for transverse variations at $x = 0$.

has been predicted (Tij & Santos 1994) to appear at the quartic order $O(a^4)$ in the acceleration-driven Poiseuille flow, however, the dilatation, $\Delta = \boldsymbol{\nabla} \cdot \boldsymbol{u} \sim O(G_p^2)$ (see § 3.3.1), also increases with increasing $G_p \propto \hat{a}$ in an equivalent pressure-driven flow. The increased dilatation would lead to a much lower bulk temperature due to the increased pressure-dilatation cooling, thereby further diminishing the possibility of temperature bimodality even in the nonlinear regime of forcing $O(\hat{a}^4) \sim O(G_p^4)$. Note that we did not observe bimodal temperature profile $T(y)$ when the pressure-gradient was changed by a factor of 10 in present simulations. We conclude that the dilatation-driven pressure cooling ($\Phi_p = -p\Delta < 0$) is likely to be responsible for the absence of the bimodal-shape of $T(y)$ in the pressure-driven Poiseuille flow.

3.3. *Are the pressure-driven and acceleration-driven Poiseuille flows equivalent?*

It must be kept in mind that the Poiseuille flow of a molecular gas driven by a body force (acceleration) is an idealised, toy problem that cannot be realized in experiments. This forcing protocol was originally used by Cercignani & Daneri (1963) in the context of solving the Boltzmann–BGK equation with a constant body force that yielded a steady and fully developed solution for a Poiseuille-type flow of a monatomic gas; this seminal work provided the first theoretical explanation of the Knudsen minimum phenomenon. Based on the present results in §§ 3.1–3.2, we note that while the Kn-dependence of the mass-flow rate in both acceleration-driven and pressure-driven flows looks similar (barring its scale dependence as in figure 8*a*), there exist key differences at the level of the hydrodynamic fields that can be appreciated by analysing the velocity gradient tensor of the two flows as discussed below.

Downloaded from https://www.cambridge.org/core. IP address: 3.144.47.8, on 13 Nov 2024 at 06:58:59, subject to the Cambridge Core terms of use, available at https://www.cambridge.org/core/terms. https://doi.org/10.1017/jfm.2024.681

3.3.1. *Velocity gradient tensor, dilatation and the developing gaseous Poiseuille flow*

The velocity gradient tensor is defined as

$$\boldsymbol{L} \overset{\text{def}}{=} (\boldsymbol{\nabla u})^{\mathrm{T}} = \left[\left(\frac{\partial u_j}{\partial x_i}\right)^{\mathrm{T}}\right] = \left[\frac{\partial u_i}{\partial x_j}\right] = \left[L_{ij}\right] = \begin{pmatrix} \frac{\partial u_x}{\partial x} & \frac{\partial u_x}{\partial y} & \frac{\partial u_x}{\partial z} \\ \frac{\partial u_y}{\partial x} & \frac{\partial u_y}{\partial y} & \frac{\partial u_y}{\partial z} \\ \frac{\partial u_z}{\partial x} & \frac{\partial u_z}{\partial y} & \frac{\partial u_z}{\partial z} \end{pmatrix}, \tag{3.10}$$

whose trace

$$\mathrm{trace}(\boldsymbol{L}) = L_{kk} = \frac{\partial u_k}{\partial x_k} = \partial_k u_k \overset{\text{def}}{=} \Delta \tag{3.11}$$

is called the dilatation. The symmetric part of L_{ij} is

$$D_{ij} \overset{\text{def}}{=} \frac{1}{2}\left(L_{ij} + L_{ji}\right) = \frac{1}{2}\left(\frac{\partial u_i}{\partial x_j} + \frac{\partial u_j}{\partial x_i}\right) \tag{3.12}$$

and its deviatoric (traceless, symmetric) part is

$$S_{ij} = \overline{\partial_j u_i} \overset{\text{def}}{=} \frac{1}{2}\left(\frac{\partial u_i}{\partial x_j} + \frac{\partial u_j}{\partial x_i}\right) - \frac{1}{3}\delta_{ij}\frac{\partial u_k}{\partial x_k} \equiv D_{ij} - \frac{\Delta}{3}\delta_{ij} = S_{ji}, \tag{3.13}$$

denoted by an 'over-bar' on the respective tensorial quantity. The deformation field is classified in terms of the invariants of the objective deformation rate $\boldsymbol{D}$, defined via $D_k = trace(\boldsymbol{D}^k)/k,\ k = 1, 2, 3$ (Goddard 2014), with the dilatation $\Delta = \mathrm{trace}(\boldsymbol{D}) \equiv D_1$ being its first invariant. The dilatation-free, $\Delta = 0$, deformation for a compressible gas is equivalent to the condition that the material derivative of the mass density is zero,

$$\frac{\mathrm{D}\rho}{\mathrm{D}t} \equiv \left(\frac{\partial}{\partial t} + \boldsymbol{u}\cdot\boldsymbol{\nabla}\right)\rho = -\rho(\boldsymbol{\nabla}\cdot\boldsymbol{u}) = 0, \tag{3.14}$$

i.e. the specific-volume ($v = 1/\rho$) is preserved, and such deformation field ($D\rho/Dt = 0$) is known as 'isochoric' (volume preserving) deformation.

For the present case of steady, pressure-driven Poiseuille flow, there are no gradients along the z-direction, i.e. $\boldsymbol{u}(x, y) = (u_x, u_y, 0)(x, y)$ with $\partial/\partial z(\cdot) = 0$, and hence the velocity gradient tensor and its symmetric part are

$$\boldsymbol{L} = \begin{pmatrix} \frac{\partial u_x}{\partial x} & \frac{\partial u_x}{\partial y} & 0 \\ \frac{\partial u_y}{\partial x} & \frac{\partial u_y}{\partial y} & 0 \\ 0 & 0 & 0 \end{pmatrix} \quad \text{and} \quad \boldsymbol{D} = \begin{pmatrix} \frac{\partial u_x}{\partial x} & \frac{1}{2}\left(\frac{\partial u_x}{\partial y} + \frac{\partial u_y}{\partial x}\right) & 0 \\ \frac{1}{2}\left(\frac{\partial u_x}{\partial y} + \frac{\partial u_y}{\partial x}\right) & \frac{\partial u_y}{\partial y} & 0 \\ 0 & 0 & 0 \end{pmatrix}, \tag{3.15a,b}$$

with its deviatoric part being

$$\boldsymbol{S} = \begin{pmatrix} \frac{\partial u_x}{\partial x} - \frac{\Delta}{3} & \frac{1}{2}\left(\frac{\partial u_x}{\partial y} + \frac{\partial u_y}{\partial x}\right) & 0 \\ \frac{1}{2}\left(\frac{\partial u_x}{\partial y} + \frac{\partial u_y}{\partial x}\right) & \frac{\partial u_y}{\partial y} - \frac{\Delta}{3} & 0 \\ 0 & 0 & -\frac{\Delta}{3} \end{pmatrix}. \tag{3.16}$$

Downloaded from https://www.cambridge.org/core. IP address: 3.144.47.8, on 13 Nov 2024 at 06:58:59, subject to the Cambridge Core terms of use, available at https://www.cambridge.org/core/terms. https://doi.org/10.1017/jfm.2024.681

An expression for the dilatation and its scaling can be obtained by noting the fact that the steady pressure-driven Poiseuille flow of a gas can never be in a fully developed state, irrespective of the channel length ($L_x < \infty$), and hence the flow field is two-dimensional (*viz.* figures 5*a*,*b*, 6*a*,*b* and 9; assuming homogeneity along the z-direction). The latter can be understood from the steady mass balance equation (3.1):

$$\Delta(x, y) = \boldsymbol{\nabla} \cdot \boldsymbol{u} = -u_x \frac{\partial \ln \rho}{\partial x} - u_y \frac{\partial \ln \rho}{\partial y}, \tag{3.17}$$

$$\Rightarrow \quad \Delta(x, 0) = -u_x(x, 0) \left.\frac{\partial \ln \rho}{\partial x}\right|_{y=0} \neq 0. \tag{3.18}$$

Equation (3.18) implies that the local dilatation is always finite and positive since (i) $u_x(x, 0) > 0$ and (ii) the density of the gas decreases along the axial direction (*viz.* figures 10*b* and 11*b*), irrespective of (i) the magnitude of the axial pressure gradient G_p and (ii) the length of the channel (L_x). For the pressure-driven flow,

$$u_x \propto \frac{\mathrm{d}p}{\mathrm{d}x} = \frac{\delta p}{L_x} \sim G_p \quad \text{and} \quad \rho = \rho_0(1 - G_\rho x - G_\rho^2 x^2), \tag{3.19a,b}$$

and assuming that $G_\rho = O(G_p)$ under small pressure gradient, it immediately follows that

$$\Delta(x, 0) \sim G_p G_\rho \sim G_p^2, \tag{3.20}$$

i.e. the dilatation scales quadratically with the imposed pressure-gradient G_p.

That the dilatation is non-zero within the bulk of the channel can be ascertained from figure 15(*a*,*b*) that display the contours of $\Delta(x, y)/G_p^2$ for $Kn = 0.05$ and 0.5, respectively; the imposed pressure gradient is $G_p = 1/15$ (i.e. $\delta p/p_0 = 0.2$) and the channel aspect ratio is $AR = 3$. Similar qualitative variations of $\Delta(x, y)$ hold also in longer channels with $AR = 9$ and 27 (not shown). Figure 15(*c*,*d*) confirms that $\Delta(x, 0) > 0$ and increases axially within the bulk region of the channel, except near the entrance and exit, irrespective of the values of the channel length (L_x) and the pressure gradient (G_p). It is also clear from figure 15(*c*,*d*) that the quadratic scaling (3.20) holds approximately within the bulk of the channel, and the data collapse is relatively better at higher rarefaction ($Kn = 0.5$, figure 15*d*) than that at $Kn = 0.05$ (figure 15*c*). The case denoted by the black line in figure 15(*c*) corresponds to a nonlinear axial density profile (see the profile of $\partial_x \rho(x, 0)$ in figure 15*e*) and the neglected HOT (i.e. $\partial_x \rho(x, 0) = -G_\rho - G_\rho^2 x + \cdots$) are likely responsible for its disagreement with the remaining two cases in figure 15(*c*) for $Kn = 0.05$. On the other hand, the density profiles $\rho(x, 0)$ at higher rarefaction ($Kn = 0.5$) can be approximated having a linear decay with x, with nearly constant axial gradients (see figure 15*f*), and hence the axial profiles of $\Delta(x, 0)/G_p^2$ for the three cases at $Kn = 0.5$ closely follow each other in figure 15(*d*).

For the idealized problem of the acceleration-driven Poiseuille flow (Cercignani & Daneri 1963; Ohwada *et al.* 1989; Alaoui & Santos 1992; Tij & Santos 1994; Mansour *et al.* 1997; Uribe & Garcia 1999; Aoki *et al.* 2002; Gupta & Alam 2017; Rongali & Alam 2018*a*; Alam *et al.* 2021) of a gas, the flow is one-dimensional with no gradients along x and z-directions, i.e. $\boldsymbol{u}(y) = (u_x(y), 0, 0)$ with $\partial/\partial x(\cdot) = 0 = \partial/\partial z(\cdot)$. The velocity gradient tensor and its symmetric and deviatoric parts are given by

$$\boldsymbol{L} = \begin{pmatrix} 0 & \dfrac{\partial u_x}{\partial y} & 0 \\ 0 & 0 & 0 \\ 0 & 0 & 0 \end{pmatrix} \quad \text{and} \quad \boldsymbol{D} = \begin{pmatrix} 0 & \dfrac{1}{2}\dfrac{\partial u_x}{\partial y} & 0 \\ \dfrac{1}{2}\dfrac{\partial u_x}{\partial y} & 0 & 0 \\ 0 & 0 & 0 \end{pmatrix} \equiv \boldsymbol{S}. \tag{3.21a,b}$$

Downloaded from https://www.cambridge.org/core. IP address: 3.144.47.8, on 13 Nov 2024 at 06:58:59, subject to the Cambridge Core terms of use, available at https://www.cambridge.org/core/terms. https://doi.org/10.1017/jfm.2024.681

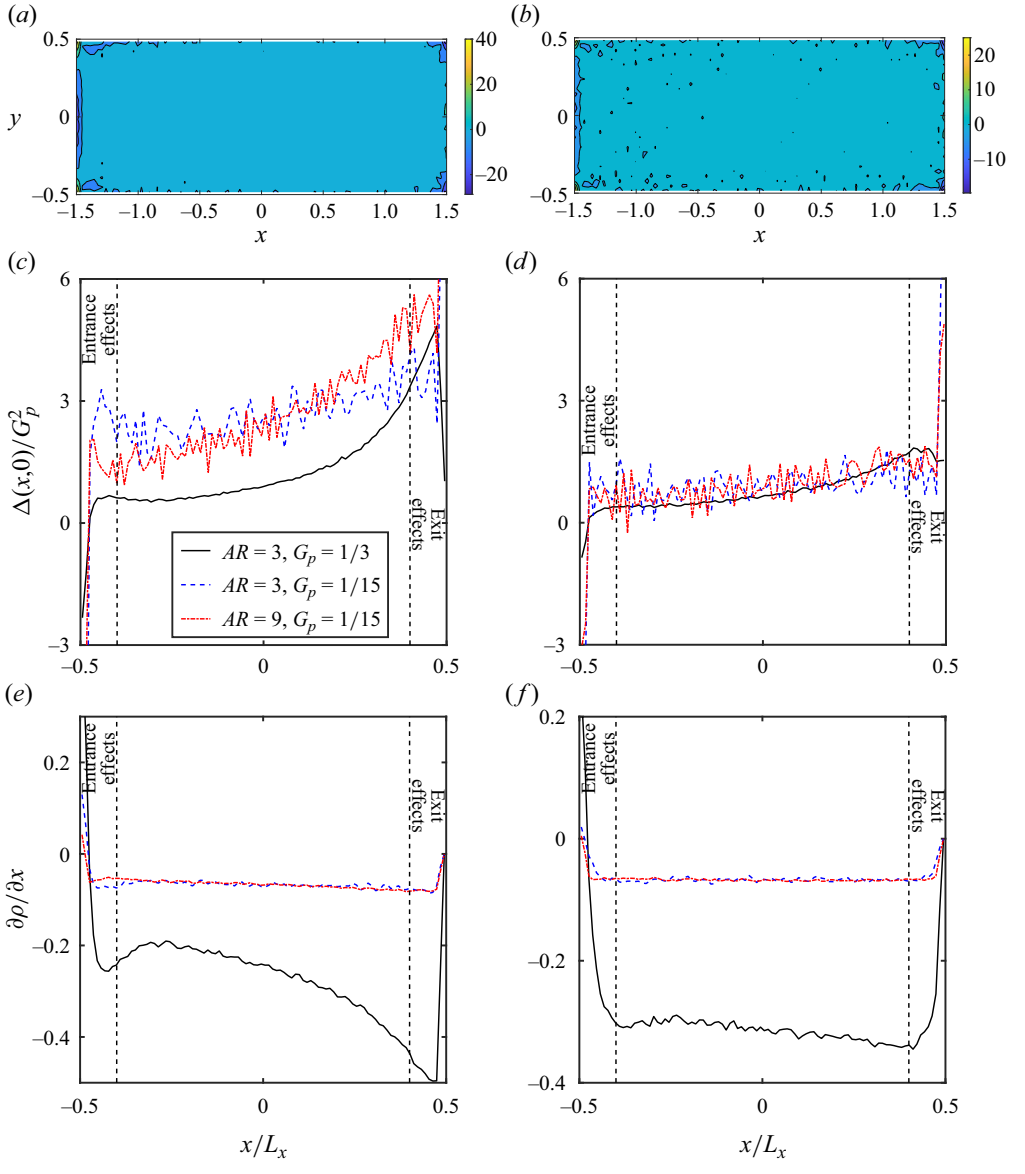

Figure 15. (*a*,*b*) Contours of the normalized dilatation '$\Delta(x, y)/G_p^2$' in the $(x/L_y, y/L_y)$-plane for $G_p = 1/15$ ($\delta p/p_0 = 0.2$) and $AR = 3$. (*c*,*d*) Axial variations of '$\Delta(x, 0)/G_p^2$' for three data sets: (i) black solid line ($G_p = 1/3$ (i.e. $\delta p/p_0 = 1.0$) and $AR = 3$); (ii) blue dashed line ($G_p = 1/15$ ($\delta p/p_0 = 0.2$) and $AR = 3$); (iii) red dot–dashed line ($G_p = 1/15$ ($\delta p/p_0 = 0.6$) and $AR = 9$). (*e*,*f*) Axial variations of the density gradient '$\partial\rho(x, 0)/\partial x$', with other parameters as in panels (*c*,*d*). The panels denote data for (*a*,*c*,*e*) $Kn = 0.05$ and (*b*,*d*,*f*) $Kn = 0.5$, respectively. The wiggles seen in two data sets in (*c*,*d*) are due to (i) the discrete derivative calculations and (ii) the increased noise in the DSMC data at small values of G_p.

The dilatation is given by

$$\Delta(x, y, z) = \frac{\partial u_x}{\partial x} + \frac{\partial u_y}{\partial y} + \frac{\partial u_z}{\partial z} = 0, \tag{3.22}$$

Downloaded from https://www.cambridge.org/core. IP address: 3.144.47.8, on 13 Nov 2024 at 06:58:59, subject to the Cambridge Core terms of use, available at https://www.cambridge.org/core/terms. https://doi.org/10.1017/jfm.2024.681

i.e. the steady, fully developed acceleration-driven Poiseuille flow is divergence-free and consequently the deformation is isochoric ($\mathrm{D}\rho/\mathrm{D}t = 0$) which remains the major difference with its non-isochoric ($\mathrm{D}\rho/\mathrm{D}t \neq 0$) pressure-driven counterpart (3.20) at the level of the velocity gradient tensor.

3.3.2. *Inequivalence at the NSF order $O(Kn)$*

The analysis in § 3.3.1 suggests that, irrespective of the magnitude of the axial pressure gradient (G_p) and the channel length (L_x), the 'equivalence' between the pressure-driven and acceleration-driven Poiseuille flows of rarefied gases is not expected to hold for all hydrodynamic fields even at the NSF order. The origin of the said inequivalence is tied to the fact that the steady, gaseous pressure-driven flow is spatially developing, with finite dilatation ((3.17)–(3.18)), and consequently the deformation is non-isochoric ($\mathrm{D}\rho/\mathrm{D}t \neq 0$). As explained in § 3.2.2, one important consequence of the dilatation is an effective cooling of the gas via the pressure-dilatation work, and thereby ruling out the appearance of the bimodal shape of the temperature profile $T(y)$ at $Kn \sim 0$ even in the nonlinear regime of large G_p. Further confirmation of the inequivalence between the two forcings in generating the hydrodynamic fields at the NSF order will be provided in § 4.3.1 while discussing the origin of normal stress differences.

At the level of hydrodynamic fields, the perceived equivalence between the two flows holds only for the mass flow rate that can be quantitatively predicted in a pressure-driven gaseous flow (Cercignani & Daneri 1963; Cercignani 1979) by assuming a 'constant' pressure gradient (and hence the linearly varying pressure and density fields, (3.4*a*,*b*), along the axial direction) in a finite-length ($L_x < \infty$) channel, and the logarithmic branch, $\mathcal{M}(Kn, L_x) \propto \log Kn$ at $Kn \gg 1$, is recovered in the limit of $L_x \to \infty$. More specifically, the underlying assumptions ((3.4*a*,*b*)–(3.4*a*,*b*)) help to transform the 'two-dimensional' problem of the pressure-driven flow to an equivalent 'one-dimensional' problem of acceleration-driven flow. The mass flow rate, being invariant of the streamwise distance in both flows, can be predicted from the linearized Boltzmann theory (Cercignani & Daneri 1963; Cercignani 1979; Takata & Funagane 2011) by using the ansatz $\hat{a} \leftrightarrow G_p$, and the dilatation ($\Delta \neq 0$) does not affect $\mathcal{M}$ since this is a conserved quantity.

4. Stress tensor and transport coefficients

The rheology of the gas is characterized by the stress tensor $\boldsymbol{P}$ and the related transport coefficients. The stress tensor can be decomposed into isotropic and deviatoric parts

$$\boldsymbol{P} = p\boldsymbol{I} + \boldsymbol{\sigma}, \tag{4.1}$$

where $p = P_{ii}/3$ is the pressure, $\boldsymbol{\sigma}$ is the stress deviator and $\boldsymbol{I}$ is the identity tensor. For the planar flows, the only non-zero off-diagonal term $P_{xy}(x, y)$ represents the shear stress that depends on both (x, y) in pressure-driven Poiseuille flow; we have verified that P_{xz} and P_{yz} fluctuate around zero in present simulations. It should be noted that the 'rarefaction-induced' signatures on the rheology of a gas can be explained if certain beyond-NSF-order terms (Burnett 1935; Chapman & Cowling 1970; Tij & Santos 1994; Uribe & Garcia 1999; Tij & Santos 2004; Taheri *et al.* 2009; Takata & Funagane 2011; Alam *et al.* 2015; Saha & Alam 2017; Rongali & Alam 2018*a*,*b*) are included. In the rest of this paper, we shall show that the dilatation must be considered in the constitutive models to explain several seemingly anomalous findings on the rheology of non-isochoric flows such as in the present case.

Downloaded from https://www.cambridge.org/core. IP address: 3.144.47.8, on 13 Nov 2024 at 06:58:59, subject to the Cambridge Core terms of use, available at https://www.cambridge.org/core/terms. https://doi.org/10.1017/jfm.2024.681

4.1. *Shear stress and viscosity*

Using the DSMC data on the shear stress P_{xy}, the local shear viscosity is calculated from

$$\mu(x, y) = -\frac{P_{xy}(x, y)}{2S_{xy}}, \tag{4.2}$$

where $2S_{xy} = \dot{\gamma}(x, y) = (\partial_y u_x + \partial_x u_y) \approx \partial_y u_x$ is the local shear rate. The cross-stream variations of the shear stress $P_{xy}(0, y)$, the local shear rate $\dot{\gamma}(0, y)$ and the shear viscosity $\mu(0, y)$ for different Kn are shown in figures 16(*a*), 16(*b*) and 16(*c*), respectively, for $\delta p/p_0 = 1$ and $AR = 3$; the analogous plots for the acceleration-driven flow are displayed in figure 16(*d–f*) for $\hat{a} = 0.1$. It is seen in figure 16(*a*,*d*) that the shear stress $P_{xy}(y)$ profiles are nearly linear with y and independent of Kn at large values of Kn for both forcing, but become nonlinear with y at small values of Kn ($Kn = 0.05$, figure 16*a*) for the pressure-driven case. From the viscosity variations in figure 16(*c*,*f*), we find that the viscosity decreases away from the channel centreline ($y = 0$), confirming the shear-thinning behaviour of rarefied gases since the local shear rate $\dot{\gamma}(0, y)$ (see figure 16*b*,*e*) increases in the same limit. Note further in figure 16(*c*,*f*) that the viscosity profiles become increasingly non-uniform with increasing Kn, and the magnitude of local $\mu(y)$ increases with increasing Kn due to the decrease in the overall/effective shear rate (across the half-channel width),

$$\dot{\gamma}_{eff} = \frac{u_x(0) - u_x(\pm 1/2)}{L_y/2} \equiv \frac{1}{2}\left(\frac{\mathrm{d}u_x}{\mathrm{d}y}(y = -0.5) + \frac{\mathrm{d}u_x}{\mathrm{d}y}(y = 0.5)\right) \tag{4.3}$$

as in figure 16(*b*,*e*).

We define the 'width-averaged' shear viscosity

$$\mu_{av} = \int_{-1/2}^{1/2} \mu(0, y)\, \mathrm{d}y, \tag{4.4}$$

as a measure for the effective flow resistance in the bulk. Figure 17(*a*) illustrates the effect of imposed pressure gradient on $\mu_{av}(x = 0)$ for $\delta p/p_0 = 1$ and 0.2; both curves closely follow each other, before settling towards a plateau value at $Kn \gg 1$, similar to the saturation of the mass flow rate seen in figure 8(*a*). Figure 17(*b*) indicates that the saturation of μ_{av} at large Kn is a consequence of the finite length of the channel. Comparing figure 17(*a*) with figure 17(*c*), we find that the average viscosity in the pressure-driven case is smaller than that in its acceleration-driven counterpart. This observation holds also for the local viscosity $\mu(y)$ as it is evident from figure 16(*c*,*f*).

To explain the above finding of the reduction of viscosity, we consider the leading expression for the shear-viscosity of a gas undergoing pressure-driven Poiseuille flow,

$$\mu = \mu_{NSF}\mathcal{F}_0(\Delta, T), \quad \text{with } \mathcal{F}_0(\Delta, T) \approx 1 - c_\mu\, Kn\left(\frac{\Delta}{\sqrt{T}}\right), \tag{4.5}$$

valid up-to the Burnett-order $O(Kn^2)$, where

$$\mu_{NSF} = \mu_0\sqrt{T}, \quad \text{with } \mu_0 = \sqrt{2}\omega_0\rho l_f \approx 0.7957\rho l_f, \tag{4.6}$$

denotes the viscosity at the NSF order and $\mathcal{F}_0(\Delta, T)$ is its Burnett-order correction factor, with $c_\mu \approx 4$; (4.5) holds strictly around the channel centreline, see Appendix C.2 for details. The dimensionless expression $\mathcal{F}_0(\Delta, T)$ in (4.6) incorporates the leading

Downloaded from https://www.cambridge.org/core. IP address: 3.144.47.8, on 13 Nov 2024 at 06:58:59, subject to the Cambridge Core terms of use, available at https://www.cambridge.org/core/terms. https://doi.org/10.1017/jfm.2024.681

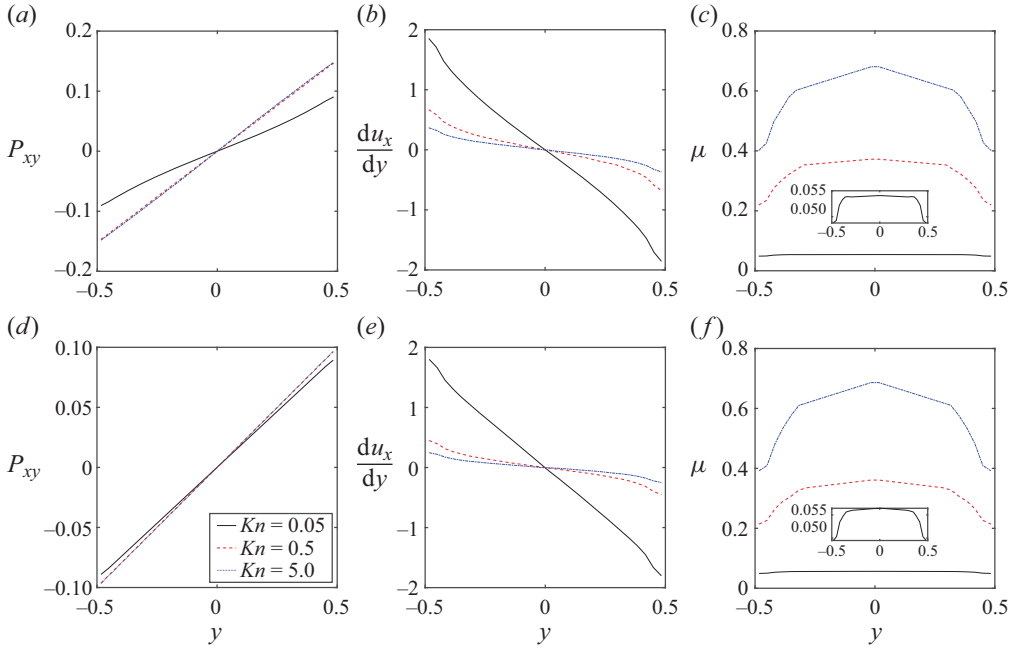

Figure 16. (*a–c*) Cross-stream variations of (*a*) shear stress $P_{xy}(0, y)$, (*b*) shear rate $\mathrm{d}u_x/\mathrm{d}y(0, y)$ and (*c*) shear viscosity $\mu(0, y)$ at $x = 0$ in pressure-driven Poiseuille flow with $\delta p/p_0 = 1$ and $AR = 3$. (*d–f*) Same as in (*a–c*), but for the acceleration-driven case with dimensionless acceleration $\hat{a} = 0.1$. The insets in (*c*,*f*) denote the close-up version of the case with $Kn = 0.05$. For all panels the channel width is $L_y/d = 1860$.

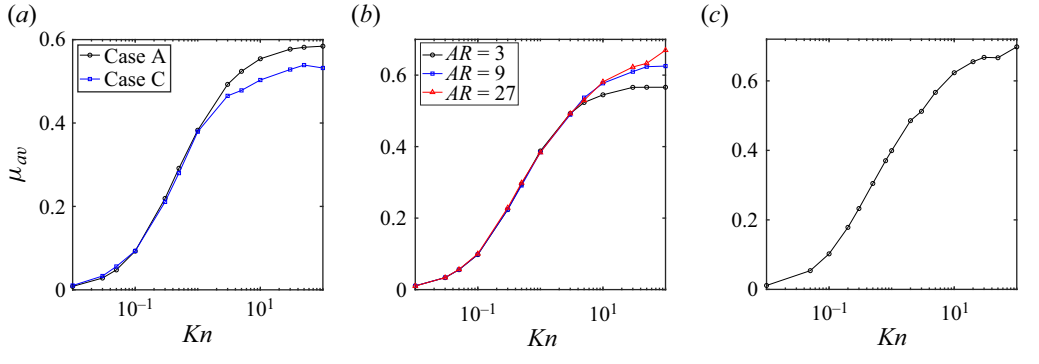

Figure 17. Variations of the width-averaged viscosity $\mu_{av}(x = 0)$ (4.4) with Knudsen number: (*a*) effect of pressure gradient ($\delta p/p_0 = 1$, open black circles; $\delta p/p_0 = 0.2$, filled blue circles) on μ_{av} for $AR = 3$ (table 3); (*b*) effect of channel length/aspect-ratio on μ_{av} for $\delta p/p_0 = 0.2$ (table 2). (*c*) Acceleration-driven flow with $\hat{a} = 0.1$. For all panels the channel width is $L_y/d = 1860$.

correction due to finite dilatation ($\Delta \neq 0$), a characteristic of the pressure-driven gaseous Poiseuille flow. It should be noted that for the isochoric deformation ($\Delta = 0$) of a monatomic gas the expressions for the shear viscosity (Chapman & Cowling 1970; Saha & Alam 2020) at the NSF and Burnett orders are identical (i.e. $\mu_{NSF} = \mu_{Burnett}$).

Downloaded from https://www.cambridge.org/core. IP address: 3.144.47.8, on 13 Nov 2024 at 06:58:59, subject to the Cambridge Core terms of use, available at https://www.cambridge.org/core/terms. https://doi.org/10.1017/jfm.2024.681

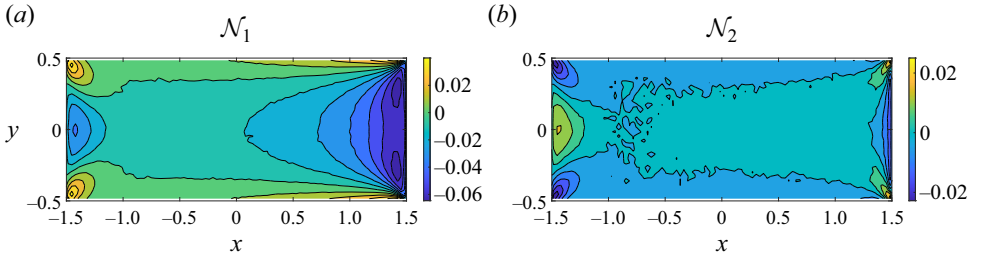

Figure 18. Contour plots of (*a*) $\mathcal{N}_1(x, y)$ and (*b*) $\mathcal{N}_2(x, y)$ for $Kn = 0.05$, $\delta p/p_0 = 1$ and $AR = 3$ ($L_y/d = 1860$).

For a quantitative understanding, with parameter values of $Kn = 0.05$, $\delta p = p_0$, and $AR = 3$, it has been verified that, at the middle $(x, y) = (0, 0)$ of the channel,

$$\frac{\partial u_x}{\partial x} \approx 20\left(\frac{\partial u_y}{\partial y}\right), \quad \Rightarrow \Delta(0,0) \approx \left.\frac{\partial u_x}{\partial x}\right|_{(0,0)} \approx 0.096. \tag{4.7}$$

With (4.7), the estimated shear viscosity (4.5) is

$$\mu(0,0) \approx 0.9817\mu_0\sqrt{T}, \tag{4.8}$$

a reduction of less than 2 %, compared with its value ($\mu(0) = \mu_0\sqrt{T} = \mu_{Burnett} \equiv \mu_{NS}$) in the acceleration-driven Poiseuille flow. Note that the positivity of the dilatation holds in the bulk region of the channel (i.e. $\Delta(x, y) > 0$), except near its entrance and exit, see figure 15(*a–d*). Therefore, we conclude that the effect of the dilatation/non-isochoricity is to reduce the shear viscosity (4.5) of the gas in the pressure-driven Poiseuille flow.

4.2. *Normal stress differences*

In general, the diagonal components of the stress tensor (4.1) are unequal (i.e. $P_{xx} \neq P_{yy} \neq P_{zz}$), and hence, in addition to pressure $p = P_{ii}/3$ and shear stress P_{xy}, two independent quantities are needed to completely describe the stress tensor in Poiseuille-type flows. These two functions are defined as (Sela & Goldhirsch 1998; Alam & Luding 2003, 2005)

$$\mathcal{N}_1(x, y) = \frac{P_{xx} - P_{yy}}{p} \quad \text{and} \quad \mathcal{N}_2(x, y) = \frac{P_{yy} - P_{zz}}{p} \equiv \frac{P_{xx} + 2P_{yy}}{p} - 3, \tag{4.9a,b}$$

known as the first (primary) and second (secondary) normal stress differences, respectively. The contour plots of $\mathcal{N}_1(x, y)$ and $\mathcal{N}_2(x, y)$ are shown in figure 18(*a,b*) for $Kn = 0.05$, indicating strong variations of both quantities along the axial and transverse directions in the pressure-driven Poiseuille flow.

The cross-stream variations of $\mathcal{N}_1(0, y)$ and $\mathcal{N}_2(0, y)$, both evaluated at $x = 0$, are shown in figures 19(*a*) and 19(*b*), respectively. It is seen that $\mathcal{N}_1$ is an order of magnitude larger compared with $\mathcal{N}_2$, and in general the two normal stress differences are found to be of opposite signs, for example,

$$\mathcal{N}_1 < 0 \quad \text{and} \quad \mathcal{N}_2 > 0, \tag{4.10a,b}$$

at any Kn in the pressure-driven case. Comparing the variations of $\mathcal{N}_1(0, 0)$ and $\mathcal{N}_2(0, 0)$ with the Knudsen number in figure 20(*a,b*), we find that the magnitudes of both quantities

Downloaded from https://www.cambridge.org/core. IP address: 3.144.47.8, on 13 Nov 2024 at 06:58:59, subject to the Cambridge Core terms of use, available at https://www.cambridge.org/core/terms. https://doi.org/10.1017/jfm.2024.681

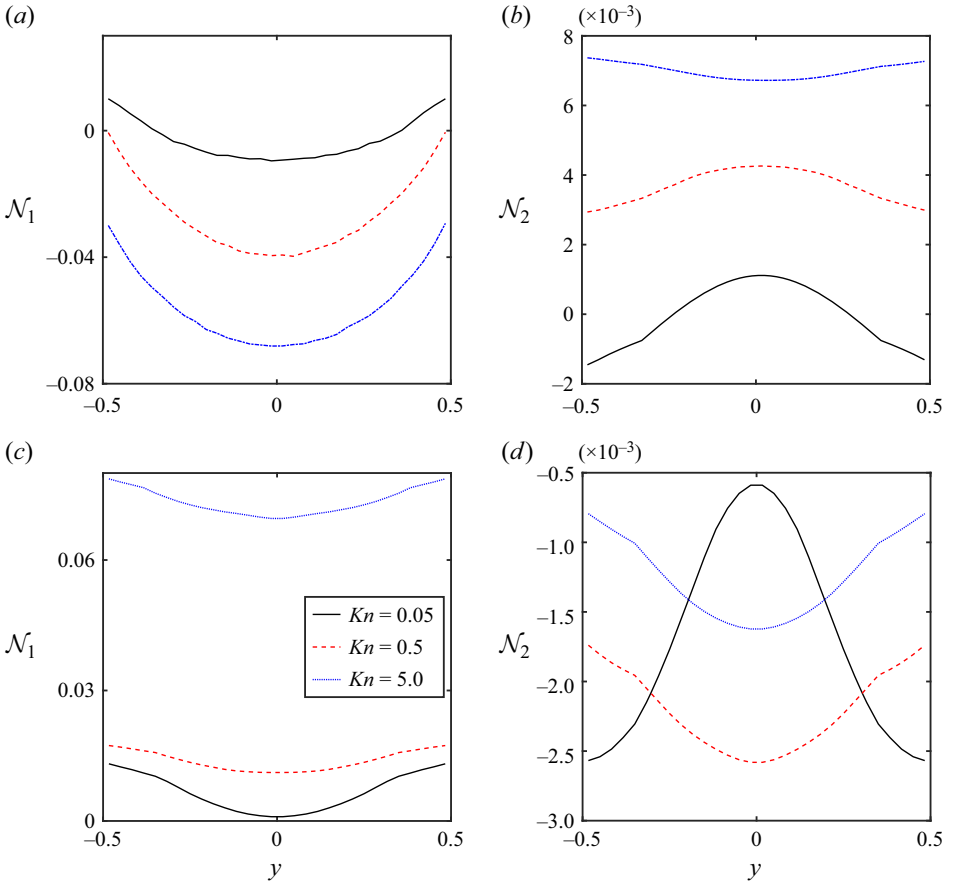

Figure 19. Cross-stream variations of (*a*) $\mathcal{N}_1(0, y)$ and (*b*) $\mathcal{N}_2(0, y)$, respectively, at the midchannel $x = 0$ in the pressure-driven flow, with parameter values as in figure 18. (*c*,*d*) Analogues of (*a*,*b*) for acceleration-driven flow with $\hat{a} = 0.1$. For all panels the channel width is $L_y/d = 1860$.

increase with increasing Kn. The observation of the anticorrelation between $\mathcal{N}_1$ and $\mathcal{N}_2$ is similar to the theoretical (Rongali & Alam 2018*a*,*b*) and previous numerical (Gupta & Alam 2017) findings in the acceleration-driven Poiseuille flow as well as in simple shear flow (Sela & Goldhirsch 1998; Alam & Luding 2005; Saha & Alam 2016). For the sake of comparison, the corresponding plots for the acceleration-driven case are displayed in figures 19(*c*,*d*) and 20(*c*,*d*) for a dimensionless acceleration of $\hat{a} = 0.1$; it is seen that while $\mathcal{N}_1(y)$ remains positive and increases with increasing Kn, the variation of $\mathcal{N}_2(y)$ with Kn is found to be non-monotonic; in particular, $\mathcal{N}_2(0)$ (figure 20*d*) is negative over a range of $Kn < 10$ but attains a positive value at large $Kn > 10$. Comparing figures 20(*a*) and 20(*c*), we find that

$$\mathcal{N}_1(0, 0)|_{pressure\text{-}driven} < 0 \quad \text{and} \quad \mathcal{N}_1(0)|_{acceleration\text{-}driven} > 0, \quad \forall\, Kn > 0. \tag{4.11a,b}$$

This sign-reversal also holds for the second normal stress difference (figure 20*b*,*d*),

$$\mathcal{N}_2(0, 0)|_{pressure\text{-}driven} > 0 \quad \text{and} \quad \mathcal{N}_2(0)|_{acceleration\text{-}driven} < 0 \quad \text{at } Kn < O(10), \tag{4.12a,b}$$

but both $\mathcal{N}_2(0, 0)$ and $\mathcal{N}_2(0)$ attain positive values at large enough $Kn > 10$.

Downloaded from https://www.cambridge.org/core. IP address: 3.144.47.8, on 13 Nov 2024 at 06:58:59, subject to the Cambridge Core terms of use, available at https://www.cambridge.org/core/terms. https://doi.org/10.1017/jfm.2024.681

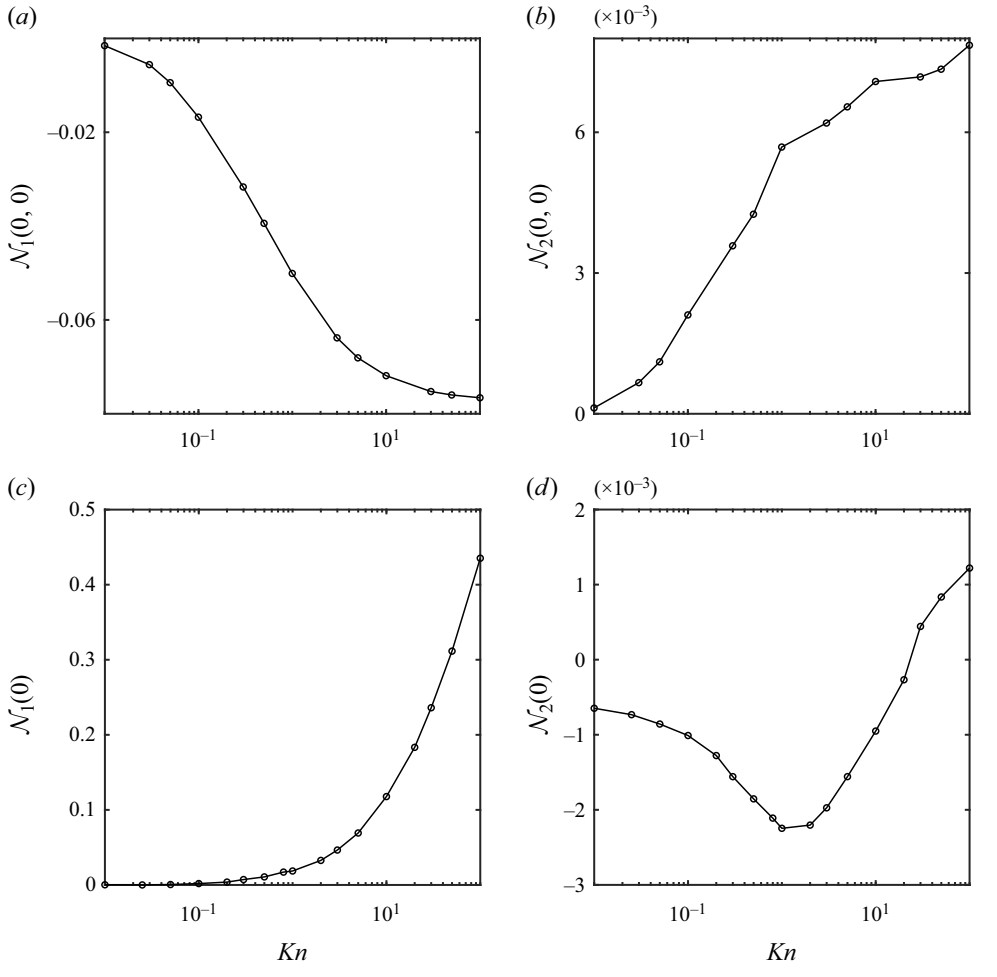

Figure 20. Variations of (*a*) $\mathcal{N}_1(0,0)$ and (*b*) $\mathcal{N}_2(0,0)$ with Knudsen number in the pressure-driven flow with parameter values as in figure 18. (*c*,*d*) Analogues of (*a*,*b*) for the acceleration-driven flow with $\hat{a} = 0.1$. For all panels the channel width is $L_y/d = 1860$.

The above findings on the *Kn*-dependence of two normal stress differences are robust, irrespective of the value of the imposed pressure gradient and the channel length as confirmed in figure 21(*a*,*b*). It is seen that the magnitude of $\mathcal{N}_1(0,0)$ decreases with decreasing G_p, and tends to saturate to constant values at large $Kn \gg 1$, irrespective of the imposed pressure gradient; similar behaviour persists for $\mathcal{N}_2(0,0)$ too (not shown).

4.3. *Origin of normal stress differences and comparison with theory*

The sign-change of two normal stress differences ((4.11*a*,*b*)–(4.12*a*,*b*)), depending on whether the flow is generated by an axial pressure gradient or a constant body force, is one major difference between the two Poiseuille-type flows. To provide a theoretical justification for the observed differences in (4.11*a*,*b*)–(4.12*a*,*b*), we carry out an analysis at

Downloaded from https://www.cambridge.org/core. IP address: 3.144.47.8, on 13 Nov 2024 at 06:58:59, subject to the Cambridge Core terms of use, available at https://www.cambridge.org/core/terms. https://doi.org/10.1017/jfm.2024.681

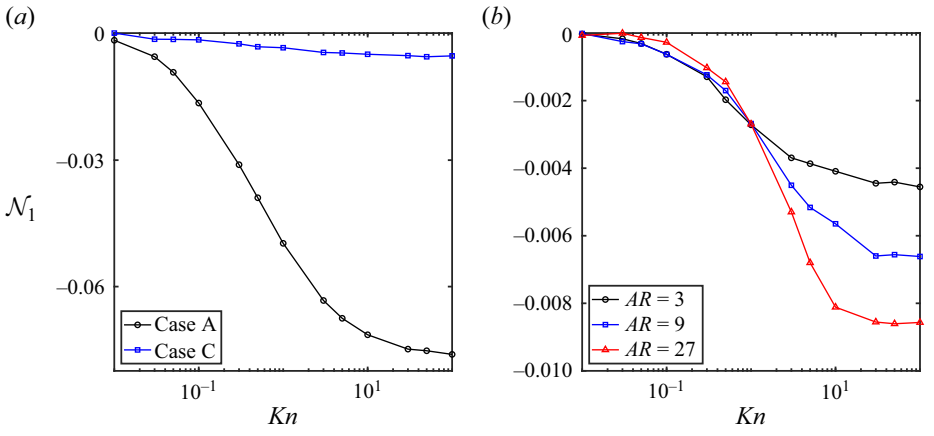

Figure 21. Effects of (*a*) imposed pressure gradient and (*b*) channel length or aspect-ratio on the variations of $\mathcal{N}_1(0,0)$ with Knudsen number. For both panels, the channel width is $L_y/d = 1860$, with other parameters as in tables 2 and 3.

the channel centre $(x, y) = (0, 0)$ for which

$$\frac{\partial}{\partial y}(\rho, T, p, u_x)\bigg|_{y=0} = 0 \tag{4.13}$$

that holds for both the forcings.

4.3.1. *Origin of $\mathcal{N}_i$ and the inequivalence between the two flows*

From the Burnett-order $O(Kn^2)$ stress tensor (Chapman & Cowling 1970; Sela & Goldhirsch 1998), the expressions for two normal stress differences have been derived – the details are given in Appendix C.3, leading to (C21) and (C23). For the pressure-driven Poiseuille flow, the expressions for the first and second normal stress differences, evaluated at $(x, y) = (0, 0)$, are given by

$$\mathcal{N}_1(0,0) \approx Kn^2\left(c_1 p^{-1}\partial_{yy}p - (c_1 - c_2)T^{-1}\partial_{yy}T\right) - \frac{2\mu(T,\Delta)}{p}\mathcal{S}_1$$
$$\underline{-c_3 Kn^2 p^{-1}\partial_x T\partial_x\rho + c_4 Kn^2 T^{-2}(\partial_x T)^2 - c_5 Kn^2 T^{-1}\mathcal{S}_1\Delta}\,, \tag{4.14}$$

$$\mathcal{N}_2(0,0) = -Kn^2\left(c_1 p^{-1}\partial_{yy}p - (c_1 - c_2)T^{-1}\partial_{yy}T\right) - \frac{2\mu(T,\Delta)}{p}\mathcal{S}_2$$
$$\underline{-Kn^2 T^{-1}\left(c_6\Delta - c_7\mathcal{S}_2\right)\mathcal{S}_2}\,, \tag{4.15}$$

where the numerical constants, c_i, are

$$c_1 \approx 3.8532, \quad c_2 \approx 2.322, \quad c_3 \approx 2.1374, \quad c_4 \approx 0.57, \quad c_5 \approx 0.1452, \tag{4.16a–e}$$

and

$$\mathcal{S}_1 \overset{\text{def}}{=} \left(S_{xx} - S_{yy}\right) = \frac{\partial u_x}{\partial x} - \frac{\partial u_y}{\partial y} \equiv D_{xx} - D_{yy}, \tag{4.17}$$

$$\mathcal{S}_2 \overset{\text{def}}{=} \left(S_{yy} - S_{zz}\right) = \frac{\partial u_y}{\partial y} - \frac{\partial u_z}{\partial z} = \frac{\partial u_y}{\partial y} \equiv D_{yy} - D_{zz}, \tag{4.18}$$

Downloaded from https://www.cambridge.org/core. IP address: 3.144.47.8, on 13 Nov 2024 at 06:58:59, subject to the Cambridge Core terms of use, available at https://www.cambridge.org/core/terms. https://doi.org/10.1017/jfm.2024.681

are called the first and second normal shear-rate difference (NSRD), respectively. The latter two parameters ((4.17)–(4.18)) represent the diagonal-anisotropy of the deformation rate $\boldsymbol{D}$ and its deviator $\boldsymbol{S}$ that are defined in § 3.3.1. Note that while the expression for $\mathcal{N}_2(0,0)$ in (4.15) is exact at this level, $O(Kn^2)$, of analysis, (4.14) has been approximated via an additional assumption that $\partial_{xx}(\rho,T) \ll \partial_{yy}(\rho,T)$ (see Appendix C.3).

The second term ($\propto \mathcal{S}_i$) in each of (4.14)–(4.15) needs clarification: they can be identified with the second and third terms in (C1), or, equivalently, with the second term in (C5) of the stress tensor, and are also present in the NSF-order $O(Kn)$ constitutive relation for the stress tensor. For finite values of G_p and $\mathcal{S}_i$, the quadratic-order terms in Kn in (4.14)–(4.15) can be neglected for $Kn \to 0$ and hence the expressions for $\mathcal{N}_i(0,0)$ simplify to

$$\mathcal{N}_i(0,0) \overset{Kn\to 0}{=} -\frac{2\mu}{p}\mathcal{S}_i = O\left(Kn\mathcal{S}_i\right), \quad \text{with } i = 1, 2, \tag{4.19}$$

since $\mu/p = O(Kn)$, and the sign of $\mathcal{N}_i(0,0)$ is dictated by '$\mathrm{sgn}(-\mathcal{S}_i)$' at $Kn \to 0$. Therefore, we conclude that the normal stress differences appear at $O(Kn)$ in the pressure-driven gaseous Poiseuille flow, both being driven by the coupling between the dynamic friction (μ/p) and the NSRDs ($\mathcal{S}_i \neq 0$). This should be contrasted with the Burnett-order $O(Kn^2)$ origin (Sela & Goldhirsch 1998; Alam & Luding 2005; Saha & Alam 2016) of the normal stress differences in the idealized acceleration-driven Poiseuille flow (Gupta & Alam 2017; Rongali & Alam 2018*a*) for which both the NSRDs vanish ($\mathcal{S}_1 = 0 = \mathcal{S}_2$). Equation (4.19) provides a confirmation of our assertion in § 3.3.2 that the pressure-driven and acceleration-driven Poiseuille flows are not equivalent even at NSF order $O(Kn)$.

4.3.2. *Qualitative comparison between theory and simulation*

It follows from (3.19*a*,*b*)–(3.20) and (4.17)–(4.18) that

$$\mathcal{S}_1 = O\left(G_p^2\right) \tag{4.20}$$

is second order in the normalized pressure-gradient (G_p), and $\mathcal{S}_2 = O(G_p^2/AR) \ll \mathcal{S}_1$. The underlined terms in each of (4.14)–(4.15) are smaller compared with the terms in the respective first line if the streamwise gradients of the hydrodynamic fields are assumed to be smaller than their transverse gradients. This has been verified from the present simulation data at $Kn = 0.05$ and 0.5 with $G_p = 1/3$; more specifically, the sum of the underlined terms in (4.14)–(4.15) remains negative and is an order-of-magnitude smaller than the third ($\propto \mathcal{S}_i$, negative) term in the corresponding equation, and hence they can be neglected. Therefore, the leading expressions for $\mathcal{N}_i(0,0)$ simplify to

$$\mathcal{N}_1(0,0) \approx -\frac{2\mu(T,\Delta)}{p}\mathcal{S}_1 \underline{-(c_1-c_2)Kn^2T^{-1}\partial_{yy}T + c_1Kn^2p^{-1}\partial_{yy}p}, \tag{4.21}$$

$$\mathcal{N}_2(0,0) \approx (c_1-c_2)Kn^2T^{-1}\partial_{yy}T \underline{-c_1Kn^2p^{-1}\partial_{yy}p - \frac{2\mu(T,\Delta)}{p}\mathcal{S}_2}. \tag{4.22}$$

At this level of analysis, there is a competition between the Burnett-order ($\propto Kn^2$) and the NSF-order ($\propto \mathcal{S}_i$) terms that would decide the sign of the two normal stress differences, depending on the values of imposed pressure gradient (G_p) and the Knudsen number (Kn). While the rarefaction-induced terms in (4.21)–(4.22) dominate in the limit of $G_p \to 0$,

Downloaded from https://www.cambridge.org/core. IP address: 3.144.47.8, on 13 Nov 2024 at 06:58:59, subject to the Cambridge Core terms of use, available at https://www.cambridge.org/core/terms. https://doi.org/10.1017/jfm.2024.681

the dilatation-driven terms dominate in the continuum limit $Kn \to 0$. In principle, one can determine a threshold value of $Kn_c(G_p)$ for finite G_p that would help to identify two regions in the (G_p, Kn)-plane where the dilatation and rarefaction effects are dominant. A complete analysis would require numerically evaluating the gradients of (p, T) for given (G_p, Kn), and is beyond the scope of the present paper. Below we focus on a few specific parameter values of (G_p, Kn) to estimate the order of magnitudes of different terms in (4.21)–(4.22) and comment on the leading behaviour of $\mathcal{N}_i(0, 0)$ over the studied range of G_p.

From the simulation data in figure 12(*a*,*c*) for $Kn = 0.05$, we have evaluated the curvature terms to be ordered as

$$\partial_{yy}T(0) \sim 10\partial_{yy}p(0) \gg \partial_{yy}p(0) > 0, \tag{4.23}$$

and the NSRDs are approximated as

$$\mathcal{S}_1(0, 0)|_{Kn=0.05} \approx 10^{-1} \quad \text{and} \quad \mathcal{S}_2(0, 0)|_{Kn=0.05} \approx 5 \times 10^{-3}. \tag{4.24a,b}$$

The sum of the two under-braced terms in (4.21) is found to be negative (but its magnitude is smaller by a factor of 10 compared with the first term), and hence the leading expression is

$$\mathcal{N}_1(0, 0) \sim -\frac{2\mu(T, \Delta)}{p}\mathcal{S}_1 < 0, \tag{4.25}$$

in agreement with simulation results in figure 20(*a*). It has been verified from present simulations that the above estimates hold also at $Kn = 0.5$, and therefore the behaviour of $\mathcal{N}_1(0, 0)$ is dictated by (4.25). Note that (4.25) represents the correlation between the first NSRD $\mathcal{S}_1$ and the dynamic friction $\mu(T, \Delta)/p$ which is the leading expression of $\mathcal{N}_1(0, 0)$ and hence responsible for its negative sign in the pressure-driven flow.

On the other hand, using the simulation data at $Kn = 0.05$ and 0.5, we found that the sum of the under-braced terms in (4.22) remains negative, but is of smaller magnitude compared with the first term which is positive, leading to

$$\mathcal{N}_2(0, 0) \sim (c_1 - c_2)\frac{Kn^2}{T}\partial_{yy}T > 0. \tag{4.26}$$

Therefore, the positive sign of $\mathcal{N}_2(0, 0)$ is primarily dictated by the curvature in the temperature field at the channel centre. Recalling from § 3.2.2 that the curvature in $T(y)$ is strongly influenced by the dilatation-coupled pressure cooling, the behaviour of the second normal stress difference is also tied indirectly to dilatation-driven effects. On the whole, our Burnett-order analysis correctly predicts the signs of both $\mathcal{N}_1(0, 0)$ and $\mathcal{N}_2(0, 0)$ for small Kn in the pressure-driven Poiseuille flow.

For the acceleration-driven Poiseuille flow, we have

$$\Delta = 0 = \mathcal{S}_i = \partial/\partial x(\cdot), \tag{4.27}$$

and hence it follows from (4.14)–(4.15) that

$$\mathcal{N}_1(0) = c_1 Kn^2 p^{-1}\partial_{yy}p - (c_1 - c_2)Kn^2 T^{-1}\partial_{yy}T, \tag{4.28}$$

$$\mathcal{N}_2(0) = -\mathcal{N}_1(0), \tag{4.29}$$

with c_i given in (4.16*a–e*). From the simulation data in figure 12(*d*,*f*), it has been verified that

$$\partial_{yy}p(0) > \partial_{yy}T(0) > 0 \quad \text{and} \quad \partial_{yy}p(0) = O\left(\partial_{yy}T(0)\right), \tag{4.30a,b}$$

for small values of Kn – this balance of curvature terms in (4.30*a*,*b*) should be contrasted with (4.23) that hold for its pressure-driven counterpart which is strongly influenced by

Downloaded from https://www.cambridge.org/core. IP address: 3.144.47.8, on 13 Nov 2024 at 06:58:59, subject to the Cambridge Core terms of use, available at https://www.cambridge.org/core/terms. https://doi.org/10.1017/jfm.2024.681

the dilatation. It follows immediately from (4.28)–(4.29) that $\mathcal{N}_1(0) > 0$ and $\mathcal{N}_2(0) < 0$ at the middle of the channel – these predictions are in qualitative agreement with the DSMC results in figure 20(*c*,*d*) for the acceleration-driven flow. Note, however, that there is another sign-change of $\mathcal{N}_2(0)$ (from negative to positive values, see figure 20*d*) at large values of $Kn = O(10)$ – this remains unexplained since the Burnett-order theory $O(Kn^2)$ is likely to hold only at small values of $Kn < 1$.

To conclude this section, the Kn-dependence of $\mathcal{N}_1(0, 0)$ and $\mathcal{N}_2(0, 0)$ (figures 20*a*,*b* and 20*c*,*d*) and their signs at small Kn are dictated by (i) the dilatation-driven effects (i.e. the NSRD-dynamic-friction coupling (4.25) and the pressure-dilatation cooling) in the pressure-driven Poiseuille flow and (ii) the curvatures in temperature and pressure/density profiles in its acceleration-driven counterpart.

5. Flow-induced heat transfer

In the present Poiseuille-type flows, although the two walls are kept at isothermal conditions ($T_w = T_0$), there is a heat-flux (q_y) along the wall-normal direction which is primarily driven by the flow-induced temperature gradient,

$$q_y = -\kappa_{yy}\frac{\partial T(y)}{\partial y} + \text{HOT} \neq 0, \tag{5.1}$$

with the normal thermal conductivity of the gas being given by $\kappa_{yy} \propto \rho l_f \sqrt{T}$. This flow-induced temperature gradient also drives a heat-current along the streamwise direction (x), leading to

$$q_x = -\kappa_{xy}\frac{\partial T(y)}{\partial y} + \text{HOT} \neq 0. \tag{5.2}$$

The latter is a second-order effect since the cross-thermal conductivity is $\kappa_{xy} \propto \dot{\gamma} = O(Kn)$ and hence $q_x = O(Kn^2)$ is called rarefaction-induced 'tangential' heat flux. As noted in § 3.2.2, the temperature profiles can differ significantly depending on whether the flow is dilatation-free or not, and the consequent changes in both $q_y(y)$ and $q_x(y)$ profiles and the related measures (such as the tangential heat flow rate) are briefly discussed below.

5.1. *Normal and tangential heat fluxes*

Figure 22(*a*) displays the cross-stream variations of the normal heat flux $q_y(0, y)$ at the midchannel ($x = 0$) for a range of Knudsen number. Comparing them with their acceleration-driven flow counterparts in figure 22(*c*), we find that the direction of $q_y(0, y)$ is reversed which is now directed from the walls towards the channel centre. This can be understood from the temperature profiles in figure 12(*c*,*f*) along with Fourier's law of heat conduction (5.1). The corresponding profiles of the tangential heat-flux $q_x(x = 0, y)$ are displayed in figure 22(*b*,*d*). For the pressure-driven case, a double-well-shaped $q_x(0, y)$ profile is found at small values of Kn (= 0.01 and 0.05, see figure 22*b*) that transitions into a single-well structure with increasing Knudsen number; in contrast, $q_x(y)$ profiles are of single-well shape for all $Kn > 0$ in the acceleration-driven flow, see figure 22(*d*).

To quantitatively characterize the transition of $q_x(y)$-profile from a double-well to a single-well, we introduce two parameters: (i) δq_x, a measure of the relative depth of the

Downloaded from https://www.cambridge.org/core. IP address: 3.144.47.8, on 13 Nov 2024 at 06:58:59, subject to the Cambridge Core terms of use, available at https://www.cambridge.org/core/terms. https://doi.org/10.1017/jfm.2024.681

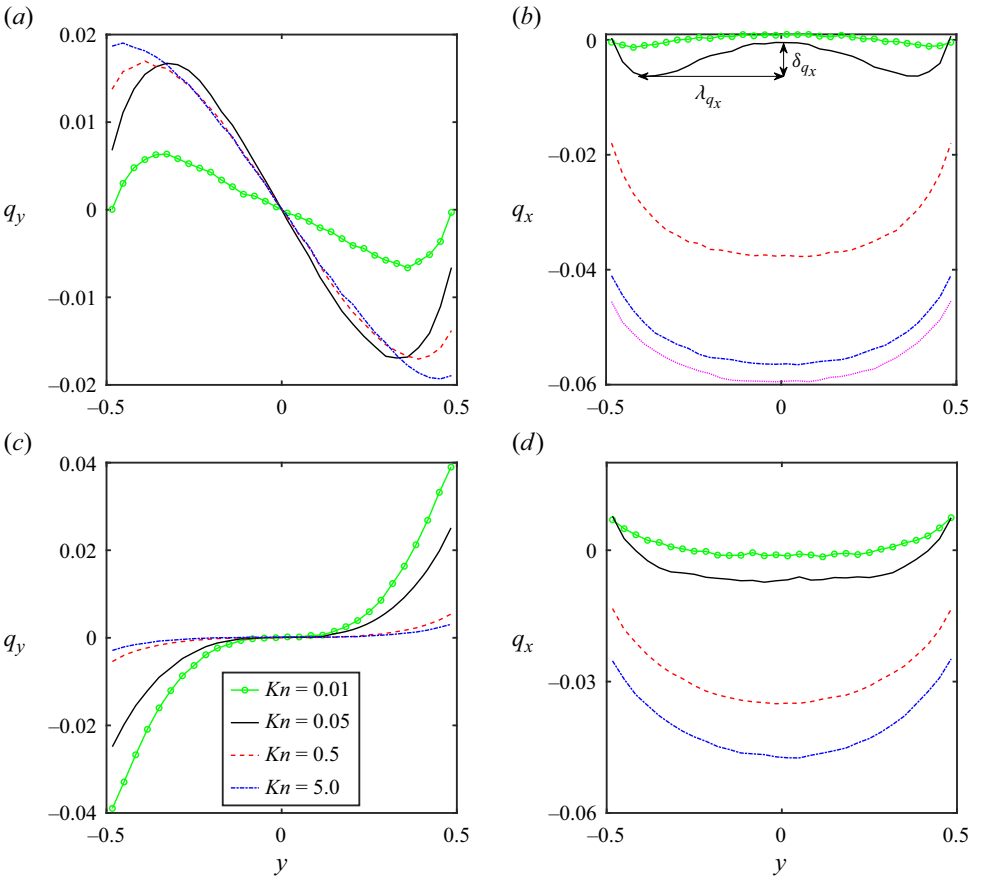

Figure 22. Cross-stream variations of (*a*,*c*) normal heat flux $q_y(0, y)$ and (*c*,*d*) tangential heat flux $q_x(0, y)$ in (*a*,*b*) pressure-driven flow with $\delta p/p_0 = 1.0$ and $AR = 3$ and (*c*,*d*) acceleration-driven flow with $\hat{a} = 0.1$. The heat flux is normalized by $\rho_0 u_0^3/2$ (see § 2.3); for all panels the channel width is $L_y/d = 1860$.

two wells with respect to $q_x(0)$, i.e.

$$\delta q_x = \min_y \left[q_x \left(y = \lambda_{q_x} \right) \right] - q_x(y = 0), \tag{5.3}$$

and (ii) λ_{q_x}, the distance of this minima, $\min(q_x(y))$, from the channel centre as marked in figure 22(*b*). The variations of δq_x and λ_{q_x} with Kn are displayed in figure 23(*a–d*). It is seen that δq_x increases until $Kn \sim 0.05$ and then falls sharply at higher Kn, while λ_{q_x} goes to 0 monotonically as $Kn \to \infty$ – these observations are robust and hold irrespective of the value of (i) the imposed pressure gradient (figure 23*a*,*b*) and (ii) the length of the channel (figure 23*c*,*d*). Since the double-well-shaped profile of $q_x(y)$ appears only at small values of the Knudsen number, this represents a near-continuum effect in the context of the pressure-driven Poiseuille flow of a rarefied gas. The present finding should be contrasted with a similar double-well shaped $q_x(y)$ profile that was reported in acceleration-driven 'granular' Poiseuille flow (Alam *et al.* 2021) – the latter phenomenon is driven by the inelasticity of particle collisions but disappears in the limit of a molecular gas.

Downloaded from https://www.cambridge.org/core. IP address: 3.144.47.8, on 13 Nov 2024 at 06:58:59, subject to the Cambridge Core terms of use, available at https://www.cambridge.org/core/terms. https://doi.org/10.1017/jfm.2024.681

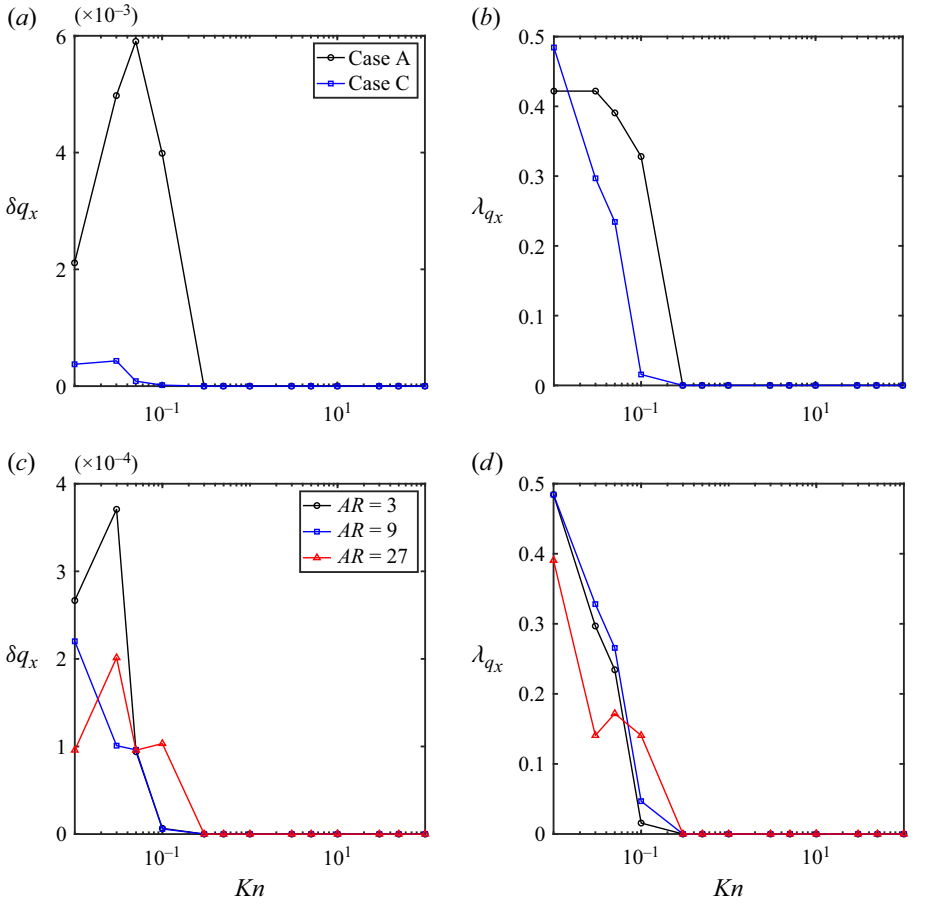

Figure 23. Effects of (*a*,*b*) pressure gradient and (*c*,*d*) channel length on the variations of (*a*,*c*) δq_x, (5.3), and (*b*,*d*) λ_{q_x} with Knudsen number, respectively; refer to figure 22(*c*) for definitions of δq_x and λ_{q_x}. For all panels, the channel width is $L_y/d = 1860$, with other parameters as in tables 2 and 3.

5.2. *Tangential heat flow rate*

Note from figure 22(*b*,*d*) that while $q_x(x = 0, y) < 0$ in the pressure-driven flow at any Kn (i.e. the tangential heat flux is directed against the imposed pressure gradient at the centre of the channel $x = 0$), it is positive and negative in the acceleration-driven case at small and large values of Kn, respectively. To measure the total heat flow rate of the tangential heat flux at any streamwise location (x), we define the following quantity:

$$\mathcal{Q}_{q_x}(x) = \int_{-0.5}^{0.5} q_x(x, y)\,\mathrm{d}y, \tag{5.4}$$

averaged over the channel width, and is called the tangential heat-flow rate (Aoki *et al.* 2002; Alam *et al.* 2021); note that (5.4) is expressed in dimensionless form. The variations of $\mathcal{Q}_{q_x}(x)$ are shown in figure 24(*a*) as a function of Kn at three different cross-sections for $\delta p/p_0 = 1$ and $AR = 3$. The analogous plots of $\mathcal{Q}_{q_x}(x = 0)$ for two values of $\delta p/p_0$ are compared in figure 24(*b*), demonstrating the effect of pressure gradient. Collectively, figure 24(*a*,*b*) confirm that $\mathcal{Q}_{q_x}(x)$ remains negative at any x (and hence is directed

Downloaded from https://www.cambridge.org/core. IP address: 3.144.47.8, on 13 Nov 2024 at 06:58:59, subject to the Cambridge Core terms of use, available at https://www.cambridge.org/core/terms. https://doi.org/10.1017/jfm.2024.681

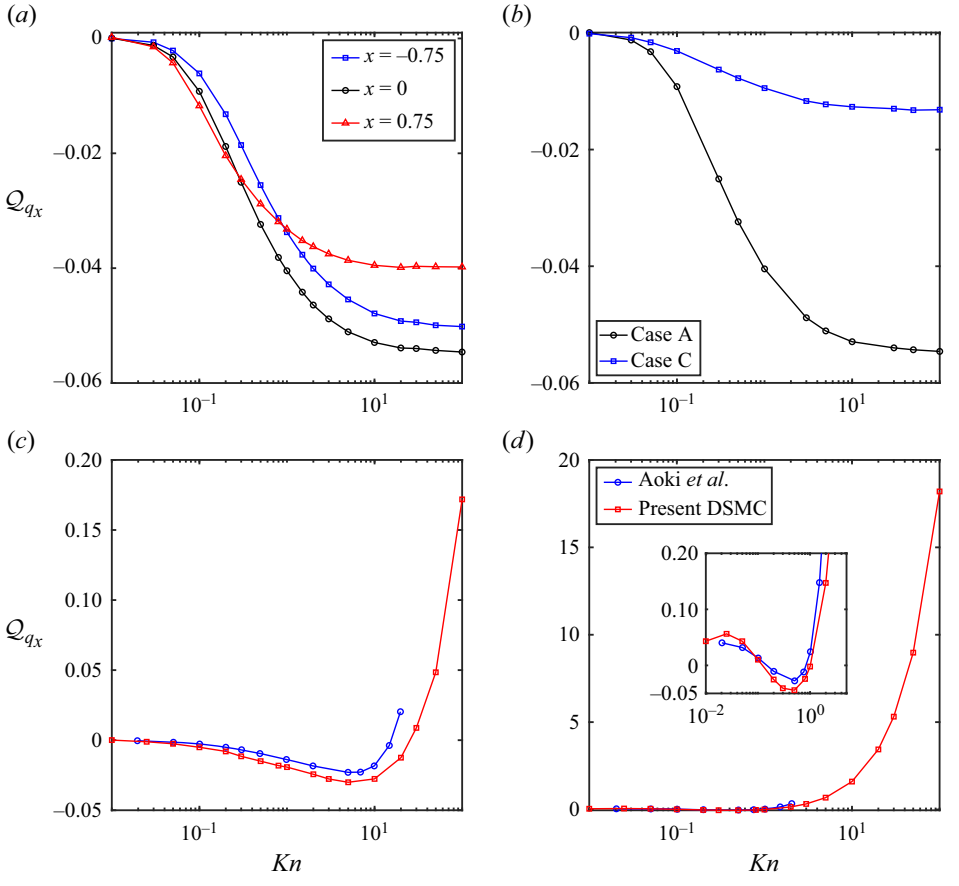

Figure 24. Variations of the tangential heat flow rate $\mathcal{Q}_{q_x}$, (5.4), with Kn: (a,b) the pressure-driven Poiseuille flow (a) at three axial locations ($x = -3/4, 0, 3/4$) with $\delta p/p_0 = 1$ and (b) the effect of pressure gradient G_p on $\mathcal{Q}_{q_x}(x = 0)$; (c,d) acceleration-driven Poiseuille flow with (c) $\hat{a} = 0.05$ and (d) $\hat{a} = 0.5$. In (c,d) the numerical results from Aoki *et al.* (2002), marked by blue circles, are also included for comparison; the inset of (d) is its close-up version over $Kn \in (10^{-2}, 1)$.

opposite to the flow direction), irrespective of the imposed pressure gradient, and its magnitude increases with increasing Kn.

In the acceleration-driven flow (figure 24b,c), however, $\mathcal{Q}_{q_x}$ can be negative/positive and varies non-monotonically with Kn. More specifically, figure 24(b,c) indicate that $\mathcal{Q}_{q_x}$ is directed along the flow direction at high Kn but can be directed against (figure 24c, $\hat{a} = 0.05$) or along (figure 24d, $\hat{a} = 0.5$) the flow direction at small Kn depending on the magnitude of forcing. In contrast, the negativity of $\mathcal{Q}_{q_x}(x)$ persists (i.e. the heat flow rate is directed against the flow direction) even if (i) the pressure-gradient is changed, see figure 24(b), and (ii) the channel length is increased, see figure 25. The latter figure shows an interesting result: $\mathcal{Q}_{q_x}(Kn, L_x)$ saturates to a constant value at $Kn > 10$ in a shorter-length channel ($AR = 3$), but it decreases continuously when the channel length is increased further ($AR = 9, 27$) and the saturation of $\mathcal{Q}_{q_x}(Kn, L_x)$ seems to be delayed to larger values of Kn with increased channel length. These overall observations are reminiscent of the saturation of the mass flow rate, see figures 7 and 8, in the pressure-driven flow through a finite-length channel.

Downloaded from https://www.cambridge.org/core. IP address: 3.144.47.8, on 13 Nov 2024 at 06:58:59, subject to the Cambridge Core terms of use, available at https://www.cambridge.org/core/terms. https://doi.org/10.1017/jfm.2024.681

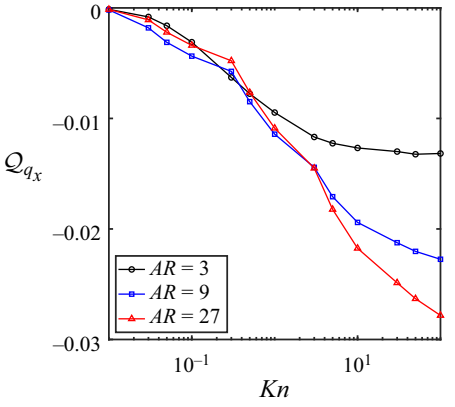

Figure 25. Effect of channel-length (L_x) on $\mathcal{Q}_{q_x}$ at $x = 0$, with $\delta p/p_0 = 0.2$: $AR = L_x/L_y = 3$ ($L_x/d = 5580$, black circles), 9 ($L_x/d = 16740$, blue squares) and 27 ($L_x/d = 50220$, red triangles); the channel width is $L_y/d = 1860$.

It should be noted that while the large-Kn branch of '$\mathcal{M}(Kn \gg 1) \sim \log Kn$' in the acceleration-driven flow can be exactly recovered (Cercignani 1979) from its pressure-driven counterpart $\mathcal{M}(Kn, L_x \to \infty)$ in the limit of infinite length ($L_x \to \infty$) of the channel, the large Kn-branches of the heat flow rate $\mathcal{Q}_{q_x}(Kn \gg 1)$ in the pressure-driven and acceleration-driven flows are qualitatively different (i.e. $\mathcal{Q}_{q_x}(Kn)$ is negative and positive, respectively). Therefore, $\mathcal{Q}_{q_x}(Kn \gg 1)$ under two forcing (G_p, $\hat{a}$) cannot be mapped from each other ($G_p \leftrightarrow \hat{a}$) in an infinite length channel ($L_x \to \infty$), irrespective of the magnitude of the forcing – this implies that the equivalence between two forcing does not hold at the level of $\mathcal{Q}_{q_x}(Kn, L_x \to \infty)$.

There is an interesting analogy between the dimensionless heat flow rate in the (acceleration-driven) Poiseuille flow and the dimensionless mass flow rate in the thermal transpiration flow (see equation (6.4) and figure 8 in Takata & Funagane (2011)) for a rarefied gas:

$$\mathcal{Q}_{q_x}\big|_{Poiseuille} = \mathcal{M}|_{ThermalTranspiration}, \quad Kn \gg 1 \quad \text{(dimensionless)}. \tag{5.5}$$

In light of the present result that $\mathcal{Q}_{q_x}(Kn \gg 1)$ has different asymptotic limits, depending on the forcing (pressure-gradient or acceleration), the validity of (5.5) is questionable for the pressure-driven Poiseuille flow of a molecular gas through a finite-length ($L_x < \infty$) channel. To demonstrate that (5.5) holds in the pressure-driven flow, one has to first show that $\mathcal{Q}_{q_x}(Kn \gg 1)$ makes a transition from negative to positive at critical values of (L_x^c, G_p^c). Although the latter seems unlikely to hold (based on results in figures 24*b* and 25 for $L_x/L_y \leq 27$), it should be further verified by considering the pressure-driven Poiseuille flow in a very long channel ($L_x \to \infty$) at arbitrarily small values of $G_p \to 0$. Given that the DSMC simulations at small G_p (and also at $\hat{a} \to 0$) yield noisy data, this issue may be investigated from a theoretical analysis based on the Boltzmann equation or by its direct solution using the fast spectral method.

5.3. *Qualitative comparison with theory: generalized Fourier law*

The primary goal of this section to explain the emergence of the double-well shape of the tangential heat flux (*viz.* figure 22*b*) in the near-continuum limit ($0 < Kn < 0.2$, figure 23) which is completely absent (*viz.* figure 22*d*) in the acceleration-driven Poiseuille flow.

Downloaded from https://www.cambridge.org/core. IP address: 3.144.47.8, on 13 Nov 2024 at 06:58:59, subject to the Cambridge Core terms of use, available at https://www.cambridge.org/core/terms. https://doi.org/10.1017/jfm.2024.681

Towards this goal, we consider the regularized 10-moment theory of Reddy & Alam (2020) who derived an expression for the heat flux of a granular gas using Grad's (Grad 1949) moment method. Their expression for the heat flux vector can be written in a compact form (Alam *et al.* 2021)

$$\boldsymbol{q} = -\boldsymbol{\kappa}^T \cdot \nabla T - \boldsymbol{\kappa}^\rho \cdot \nabla \rho - \boldsymbol{\kappa}^\sigma \cdot \nabla \cdot \boldsymbol{\sigma}, \tag{5.6}$$

which is nothing but a generalized version of the well-known Fourier law of heat conduction. The first, second and third terms in (5.6) represent heat fluxes driven by the gradients in (i) temperature (Fourier law), (ii) density (Dufour law) and (iii) deviatoric stress, respectively. The expressions for the components of the Fourier/thermal, Dufour and stress conductivity tensors are

$$\boldsymbol{\kappa}^T = \frac{\kappa}{p}\begin{pmatrix} P_{xx} & \sigma_{xy} \\ \sigma_{yx} & P_{yy} \end{pmatrix}, \quad \boldsymbol{\kappa}^\rho = -\frac{2\kappa}{5\rho^2}\begin{pmatrix} \sigma_{xx} & \sigma_{xy} \\ \sigma_{yx} & \sigma_{yy} \end{pmatrix}, \quad \boldsymbol{\kappa}^\sigma = \frac{2\kappa}{5\rho}\begin{pmatrix} 1 & 1 \\ 1 & 1 \end{pmatrix}, \tag{5.7a–c}$$

where $\kappa = \kappa(T)$ is the thermal conductivity of a monatomic gas at the NSF order, $O(Kn)$,

$$\kappa(T) = \kappa_{NSF} = \kappa_0\sqrt{T}, \quad \text{with } \kappa_0 = c_\kappa \rho l_f \quad \text{and} \quad c_\kappa = (1.025)\frac{75}{64}\sqrt{2\pi} \approx 3.013. \tag{5.8}$$

Note that the above theory is strictly valid for small values of $Kn < O(1)$.

The expression for the tangential heat flux is

$$\begin{aligned} q_x(x, y) = &-\kappa(T)\left(\frac{P_{xx}}{p}\partial_x T - \frac{2\sigma_{xx}}{5\rho^2}\partial_x\rho + \frac{2}{5\rho}\partial_x\sigma_{xx}\right) \\ &-\kappa(T)\left(\frac{\sigma_{xy}}{p}\partial_y T - \frac{2\sigma_{xy}}{5\rho^2}\partial_y\rho + \frac{2}{5\rho}\partial_y\sigma_{xy}\right) \equiv q_{x1} + q_{x2}, \end{aligned} \tag{5.9}$$

with q_{x1} and q_{x2} representing the terms involving x- and y-derivatives, respectively. The order of magnitudes of the three terms in q_{x1} can be estimated as

$$\frac{P_{xx}}{p}\partial_x T \sim O(G_p) < 0, \quad -\sigma_{xx}\partial_x\rho \sim O(G_p^2) > 0, \quad \partial_x\sigma_{xx} \sim O(G_p^2) > 0, \tag{5.10}$$

since $\sigma_{xx} = \partial_x u$ increases and both T and ρ decreases along the length of the channel, and the leading behaviour of q_{x1} is dictated by the first term,

$$q_{x1} \sim -\kappa(T)\left(1 + \frac{\sigma_{xx}}{p}\right)\partial_x T = O(G_p Kn) > 0, \tag{5.11}$$

which is positive. Therefore, the leading expression of (5.9) simplifies to

$$q_x(x, y) \approx -\kappa(T)\partial_x T - \kappa(T)\left(\frac{\sigma_{xy}}{p}\partial_y T - \frac{2\sigma_{xy}}{5\rho^2}\partial_y\rho + \frac{2}{5\rho}\partial_y\sigma_{xy}\right), \tag{5.12}$$

which also represents its dimensionless form, with the dimensionless thermal conductivity being given by

$$\kappa(T) = c_\kappa \rho\sqrt{T}Kn. \tag{5.13}$$

The estimated value of (5.12) at the centre of the channel $(x, y) = (0, 0)$ is

$$q_x(0, 0) = -\kappa(T)\partial_x T - \frac{2}{5\rho}\kappa(T)\left.\frac{\partial\sigma_{xy}}{\partial y}\right|_{(0,0)} < 0. \tag{5.14}$$

Focussing on the pressure-driven flow with $Kn = 0.5$, $\delta p/p_0 = 1$ and $AR = 3$ (figure 22), our calculations indicate that the magnitude of the first term (which is positive) in

Downloaded from https://www.cambridge.org/core. IP address: 3.144.47.8, on 13 Nov 2024 at 06:58:59, subject to the Cambridge Core terms of use, available at https://www.cambridge.org/core/terms. https://doi.org/10.1017/jfm.2024.681

(5.14) remains (slightly) smaller than the second term, yielding $q_x(0) < 0$. Therefore, the negativity of $q_x(0,0)$ originates from the heat flux driven by the stress-gradient, and this holds irrespective of whether the flow is driven by the pressure-gradient (figure 22*b*), or, the acceleration (figure 22*d*, for which $\partial_x T = 0$).

Let us now evaluate the curvature of $q_x(y)$, given by the second derivative of (5.12) as

$$\begin{aligned}\partial_{yy}q_x = &-\kappa_{yy}\partial_x T - 2\kappa_y\partial_{xy}T - \kappa\,\partial_{yyy}T - \kappa_{yy}\left(\frac{\sigma_{xy}}{p}\partial_y T - \frac{2\sigma_{xy}}{5\rho^2}\partial_y\rho + \frac{2}{5\rho}\partial_y\sigma_{xy}\right)\\ &- \kappa\left[\left(\frac{\sigma_{xy}}{p}\right)\partial_{yyy}T + 2\partial_y\left(\frac{\sigma_{xy}}{p}\right)\partial_{yy}T + \partial_{yy}\left(\frac{\sigma_{xy}}{p}\right)\partial_y T\right.\\ &-\left(\frac{2\sigma_{xy}}{5\rho^2}\right)\partial_{yyy}\rho - 2\partial_y\left(\frac{2\sigma_{xy}}{5\rho^2}\right)\partial_{yy}\rho - \partial_{yy}\left(\frac{2\sigma_{xy}}{5\rho^2}\right)\partial_y\rho\\ &\left.+\frac{2}{5\rho}\partial_{yyy}\sigma_{xy} + 2\partial_y\left(\frac{2}{5\rho}\right)\partial_{yy}\sigma_{xy} + \partial_{yy}\left(\frac{2}{5\rho}\right)\partial_y\sigma_{xy}\right].\end{aligned} \tag{5.15}$$

Noting that

$$\partial_y(T,\rho,p)\big|_{y=0} = 0 = \partial_{yyy}(T,\rho,p)\big|_{y=0} = \partial_{yy}\sigma_{xy}\big|_{y=0} = \partial_{yyy}\sigma_{xy}\big|_{y=0}, \tag{5.16}$$

the simplified expression for the curvature of $q_x(y)$ at the channel centre $(x,y) = (0,0)$ follows from (5.15) that

$$\begin{aligned}\left.\frac{\partial^2 q_x}{\partial y^2}\right|_{(0,0)} &= -\kappa_{yy}\left(\partial_x T + \frac{2}{5\rho}\partial_y\sigma_{xy}\right) - \kappa\left[2\partial_y\left(\frac{\sigma_{xy}}{p}\right)\partial_{yy}T - 2\partial_y\left(\frac{2\sigma_{xy}}{5\rho^2}\right)\partial_{yy}\rho\right.\\ &\qquad\left.+\,\partial_{yy}\left(\frac{2}{5\rho}\right)\partial_y\sigma_{xy}\right]_{y=0}\\ &= \left(\frac{\kappa_{yy}}{\kappa}\right)_{y=0} q_x(0,0) - 2\kappa\frac{\partial\sigma_{xy}}{\partial y}\left[\frac{1}{p}\partial_{yy}T - \frac{2}{5\rho^2}\partial_{yy}\rho - \frac{1}{5\rho^2}\partial_{yy}\rho\right]_{y=0}\\ &= \left(\frac{1}{\rho}\partial_{yy}\rho + \frac{1}{2T}\partial_{yy}T\right)_{y=0} q_x(0,0) - 2\frac{\kappa}{\rho}\frac{\partial\sigma_{xy}}{\partial y}\left[\frac{1}{T}\partial_{yy}T - \frac{3}{5\rho}\partial_{yy}\rho\right]_{y=0}\\ &= \underbrace{\left(\frac{1}{\rho}\partial_{yy}\rho + \frac{1}{2T}\partial_{yy}T\right)_{y=0}} q_x(0,0)\\ &\qquad + 5\,(q_x(0,0) + \kappa\partial_x T)\,\underbrace{\left[\frac{1}{T}\partial_{yy}T - \frac{3}{5\rho}\partial_{yy}\rho\right]_{y=0}},\end{aligned} \tag{5.17}$$

where we have used (5.14) in the last expression. Since $\partial_{yy}T > 0$ and $\partial_{yy}\rho < 0$ in the pressure-driven channel flow, the under-braced part of the second term in (5.17) is positive, and the underbraced part of the first term is also positive but is of much smaller magnitude than that of the second term; these estimates can be appreciated from figures 12(*b*,*c*) and 13(*b*,*c*), for example, $\partial_{yy}T(0,0) \approx 0.75$ (figure 12*c*) and $\partial_{yy}\rho(0,0) \approx -0.9$ (figure 12*b*) at

Downloaded from https://www.cambridge.org/core. IP address: 3.144.47.8, on 13 Nov 2024 at 06:58:59, subject to the Cambridge Core terms of use, available at https://www.cambridge.org/core/terms. https://doi.org/10.1017/jfm.2024.681

$Kn = 0.05$. Recalling that $q_x(0, 0) < 0$ and $\partial_x T < 0$, (5.17) confirms

$$\left.\frac{\partial^2 q_x}{\partial y^2}\right|_{(0,0)} < 0, \tag{5.18}$$

i.e. the curvature of q_x around the channel centre is negative (and hence responsible for the double-well shape of $q_x(0, y)$) which agrees with simulations in figure 22(*b*). Therefore, the generalized Fourier law ((5.6)–(5.7*a–c*)) is able to predict the emergence of the double-well shaped $q_x(0, y)$-profile at small Kn in the pressure-driven Poiseuille flow. In the present context, the $q_x(y)$-profile is indirectly affected by the dilatation-driven pressure cooling that strongly influences the curvatures of $T(y)$ and $\rho(y)$ as discussed in § 3.2.2.

It should be noted that we have omitted a flux term in (5.6), driven by the gradient of the dilatation (i.e. $\boldsymbol{q}^{\Delta} \propto \boldsymbol{\nabla}(\Delta)$) – the contribution of this term to q_x and $\partial_{yy} q_x(0, 0)$ remains negative and is of smaller magnitude compared with the retained terms, and our overall conclusions, based on above scaling arguments, would not change even if the dilatation-driven heat flux is included. In any case, a detailed quantitative comparison between theory and simulation is left to a future work.

6. Conclusions and outlook

We have studied the pressure-driven plane Poiseuille flow of a rarefied gas through a finite-length ($L_x < \infty$) channel, with a goal to ascertain its similarities and differences with the well-studied idealized problem of the acceleration-driven Poiseuille flow. For both cases, the DSMC method is used to obtain the hydrodynamic fields, the fluxes (stress tensor and heat-flux vector) and related transport coefficients over wide ranges of Knudsen number ($0.01 \leq Kn \leq 100$), pressure gradient ($0.033 < G_p = (\delta p/p_0)/AR < 1$) and aspect-ratio ($3 \leq AR = L_x/L_y \leq 27$) of the channel. Since a change in the gas pressure is always accompanied by a change in its density (assuming an isothermal state at the leading order), the steady pressure-driven Poiseuille flow, irrespective of (i) the channel length ($L_x < \infty$) and (ii) the axial pressure gradient $G_p > 0$, cannot be in a fully developed state as dictated by the mass balance equation (3.18). At the level of the deformation field, the fundamental difference between pressure-driven and acceleration-driven Poiseuille flows is identified as the presence of finite 'dilatation' ($\Delta = \mathrm{trace}(\boldsymbol{D}) = \boldsymbol{\nabla} \cdot \boldsymbol{u} > 0$, the first invariant of the deformation-rate tensor $\boldsymbol{D}$) in the former, resulting in its non-isochoric deformation ($\mathrm{D}\rho/\mathrm{D}t \neq 0$), while the flow is dilatation-free with isochoric deformation in the latter.

For the pressure-driven flow in finite-length channels, the mass flow rate, $\mathcal{M}(Kn) \sim Kn^0$, saturates to a constant value at $Kn \gg AR$ that agrees with theory (Raghuraman & Willis 1977; Cercignani 1979) and recent experiments (Ewart *et al.* 2007; Graur *et al.* 2009; Kunze *et al.* 2022), and holds irrespective of the magnitude of the axial pressure gradient and the local Mach number. The Kn- and L_x-dependence of $\mathcal{M}(Kn, L_x)$ can be predicted from the linearized Boltzmann theory (Cercignani & Daneri 1963; Raghuraman & Willis 1977; Cercignani 1979) by using the ansatz $\hat{a} \leftrightarrow G_p$, and the dilatation ($\Delta \neq 0$) does not affect $\mathcal{M}$ since this is a conserved quantity. The ansatz '$G_p \rightarrow \hat{a}$' amounts to imposing a 'constant' pressure gradient (and hence the linearly varying pressure and density fields along the axial direction (Cercignani 1979; Takata & Funagane 2011)), and the asymptotic logarithmic branch, $\mathcal{M}(Kn, L_x) \propto \log Kn$ at $Kn \gg 1$, is recovered in the limit of $L_x \rightarrow \infty$. More specifically, the underlying assumptions ((3.4*a*,*b*)–(3.5*a*,*b*)) help to transform the 'two-dimensional' problem of the pressure-driven

Downloaded from https://www.cambridge.org/core. IP address: 3.144.47.8, on 13 Nov 2024 at 06:58:59, subject to the Cambridge Core terms of use, available at https://www.cambridge.org/core/terms. https://doi.org/10.1017/jfm.2024.681

flow to an equivalent 'one-dimensional' problem of acceleration-driven flow (Takata & Funagane 2011), leading to the perceived equivalence which holds for all hydrodynamic fields up-to the NSF order of small pressure gradient $O(G_p)$. Therefore, we conclude that the 'equivalence' between the two forcings holds only for $\mathcal{M}(Kn, L_x)$ in the limit of an infinite-length ($L_x \to \infty$) channel.

In contrast to the acceleration-driven Poiseuille flow, there are two other measurable differences in the pressure-driven flow, namely, (i) the shape of the temperature profile $T(y)$ and (ii) the non-zero wall-normal velocity $u_y(y)$ – both are driven by the finite dilatation $\Delta(x, y) > 0$ in the latter flow. As explained in § 3.2.2, one important consequence of the dilatation is an effective cooling via the pressure-dilatation work ($\Phi_p = -p\Delta < 0$ since $\Delta > 0$) that rules out the possibility of the bimodal shape (Tij & Santos 1994; Mansour *et al.* 1997; Tij & Santos 2004; Alam *et al.* 2015; Gupta & Alam 2017) of the temperature profile $T(y)$ in the pressure-driven flow as confirmed via DSMC simulations over a large range of pressure gradients. This is notwithstanding the fact that the bimodality of the $T(y)$ profile is a super-Burnett order effect (Tij & Santos 1994; Rongali & Alam 2018*a*) as it appears at $O(a^4)$ for which the degree of pressure-dilatation cooling ($\Phi_p = -p\Delta \sim O(G_p^2)$) would also increase if one adopts the equivalence ansatz of $\hat{a} \leftrightarrow G_p$ between the two forcings.

The effect of dilatation was found to decrease the effective shear viscosity (*viz.* figure 16*c*,*f*) of the gas which is in agreement with the Burnett-order shear viscosity (4.5) that includes dilatation. The first and second normal stress differences ($\mathcal{N}_1$ and $\mathcal{N}_2$) have opposite signs in the pressure-driven flow in comparison with their values in the acceleration-driven flow.

From an analysis of the Burnett-order stress tensor (§ 4.3.1), we found that both $\mathcal{N}_1$ and $\mathcal{N}_2$ appear at the NSF order $O(Kn)$ in the pressure-driven Poiseuille flow that are driven by the dilatation, whereas they originate from Burnett-order $O(Kn^2)$ rarefaction effects in its acceleration-driven counterpart. These findings confirmed that the two flows are not equivalent even at the NSF order for finite axial pressure gradient $G_p \sim O(1)$. We showed (§ 4.3.2) that the odd-signs of $\mathcal{N}_1(0, 0)$ and $\mathcal{N}_2(0, 0)$ (figures 20*a*,*b* and 20*c*,*d*) and their Kn-dependence at small Kn are tied to the dilatation-driven effects: while (i) the coupling ($\sim \mu(T, \Delta)\mathcal{S}_1/p$) between the first NSRD ($\mathcal{S}_1 = \partial_x u_x - \partial_y u_y$) and the dynamic friction (μ/p) is responsible for the leading behaviour of $\mathcal{N}_1$ and its negative sign, (ii) the pressure-dilatation cooling ($\Phi_p = -p\Delta < 0$) affects the curvatures in temperature and pressure/density profiles (4.23), thereby resulting in the positive sign of $\mathcal{N}_2(0, 0)$. Although the leading expression of $\mathcal{N}_2$ remains the same ((4.22) and (4.29)) in the two flows, the vanishing of the pressure work ($\Phi_p = 0$ since $\Delta = 0$) in the acceleration-driven flow makes the curvatures of its temperature and pressure/density profiles (4.30*a*,*b*) different from (4.23), resulting in the negative sign of $\mathcal{N}_2(0, 0)$.

A double-well shape of the tangential heat flux profile ($q_x(y)$), with a local maximum at the channel centre and two symmetrically located minima away from the centre, has been uncovered over a range of $0 < Kn < 0.2$ in the pressure-driven case which is absent in its acceleration-driven counterpart. The genesis of this near-continuum effect (at $Kn \sim 0$) has been explained from a generalized Fourier law in § 5.3. The heat-flow rate of the tangential heat flux ($\mathcal{Q}_{q_x} = \int q_x(x, y)\,\mathrm{d}y$) is found to be negative, i.e. $\mathcal{Q}_{q_x}$ is directed against the axial pressure gradient; this holds for all Kn and pressure-gradient in contrast to the positive/negative $\mathcal{Q}_{q_x}$ at large/small values of Kn in its force-driven counterpart. Similar to the length scale dependence of $\mathcal{M}(Kn, L_x)$, the tangential heat flow rate $\mathcal{Q}_{q_x}(Kn, L_x)$ is found to saturate to constant values at $Kn \gg 1$ in finite length channels. While the large-Kn branch of '$\mathcal{M}(Kn \gg 1) \sim \log Kn$' in the acceleration-driven flow can be exactly

Downloaded from https://www.cambridge.org/core. IP address: 3.144.47.8, on 13 Nov 2024 at 06:58:59, subject to the Cambridge Core terms of use, available at https://www.cambridge.org/core/terms. https://doi.org/10.1017/jfm.2024.681

recovered from its pressure-driven counterpart $\mathcal{M}(Kn, L_x \to \infty)$, the large Kn-branches of $Q_{q_x}(Kn \gg 1)$ in the pressure-driven and acceleration-driven flows are qualitatively different, i.e. $Q_{q_x}(Kn \gg 1, L_x)$ is negative and positive, respectively, irrespective of the magnitude of the forcing and the channel length. The later result provides another piece of evidence for the inequivalence between the two forcings, and seems to rule out recovering the large-Kn branch of $Q_{q_x}(Kn \gg 1, L_x)$ using the ansatz '$G_p \leftrightarrow \hat{a}$'. This also puts into question the validity of (5.5): 'the dimensionless heat-flow rate in the pressure-driven Poiseuille flow can(not) be used as a proxy to estimate the dimensionless mass flow rate in the thermal transpiration flow' (Takata & Funagane (2011) and references therein). The related theoretical issues are recommended for further investigation.

On the whole, the present DSMC results, backed by theoretical analyses, confirmed that, except for the mass flow rate and its dependence on the channel length, the mapping '$G_p \leftrightarrow \hat{a}$' cannot be used to predict all flow properties in the pressure-driven Poiseuille flow of rarefied gases from those in its acceleration-driven counterpart even at the NSF order $O(Kn)$. We conclude that the dilatation, $\Delta = \boldsymbol{\nabla} \cdot \boldsymbol{u} > 0$, is responsible for the observed differences between the two flows in terms of hydrodynamic fields (§ 3), rheology (§ 4) and the flow-induced heat transfer (§ 5). Since the pressure-driven flow is created by an external pressure gradient ($u_x \propto G_p$), the dilatation scales quadratically (3.20) with the axial pressure gradient, $\Delta \propto O(G_p^2)$, and hence the observed differences belong to the second-order effects in G_p. Considering (i) the critical Knudsen number for the onset of rarefaction effects as $Kn_c \approx 10^{-3}$ (*viz.* figure 1) and (ii) the leading behaviour of the first normal stress difference

$$\mathcal{N}_1 = O(Kn\mathcal{S}_1 + Kn^2) \approx O(Kn\Delta + Kn^2), \tag{6.1}$$

we note that the equivalence between pressure-driven and acceleration-driven flows may be expected only at arbitrarily small values of $G_p \ll \sqrt{Kn_c} \approx 0.03$. The latter constraint is not satisfied in the present simulations since the smallest pressure gradient for which we could produce reliable DSMC data is $G_p = 1/30 \approx 0.033$.

In the context of the gaseous Poiseuille flow, the dilatation can be called 'pressure-gradient-induced' dilatancy and this, though of the same parental origin, differs from the well-known Reynolds dilatancy (Reynolds 1885), also called the 'shear-induced' dilatancy (i.e. shear-coupled volume change at constant pressure/load, $\Delta = \boldsymbol{\nabla} \cdot \boldsymbol{u} \propto \dot{\gamma}$), in the context of the dense granular media (Goddard 2014; Krishnaraj & Nott 2016). In the latter case, there is an equation of state for the granular pressure $p = p(D_1, D_2, \phi)$ or, equivalently, an equation for the dilatation $D_1 = \Psi(D_2, p, \phi)$, called the dilatancy relation, where $D_1 \equiv \Delta$ and D_2 are, respectively, the first and second invariants of the deformation rate tensor $\boldsymbol{D}$; expectedly, an evolution equation for the particle volume fraction ϕ governs the behaviour of the granular dilatancy Δ (Goddard 2014).

On a future perspective, the protocol of generating non-isochoric steady flows, such as the pressure-driven Poiseuille flow, can be used to study the impact of dilatation on the thermohydrodynamics of other related flows. For example, the present work can be extended to dilute gas–solid suspensions undergoing non-isochoric deformation – this is likely to shed light on certain unresolved issues (Jackson 2000) regarding the hydrodynamic fields and heat transfer in gas–solids suspensions that are encountered in fluidized-bed reactors. The present results may also find applications in gas-based catalytic processes that involve pressure-driven flows (Keerthi *et al.* 2018) through finite-length nanochannels for which the reactions are mediated by flow-induced heat and mass transfer processes in different regimes.

Downloaded from https://www.cambridge.org/core. IP address: 3.144.47.8, on 13 Nov 2024 at 06:58:59, subject to the Cambridge Core terms of use, available at https://www.cambridge.org/core/terms. https://doi.org/10.1017/jfm.2024.681

Acknowledgements. We gratefully acknowledge the support of the National Supercomputing Mission (NSM) of India for the use of the ParamYukthi Supercomputing cluster, JNCASR.

Declaration of interests. The authors report no conflict of interest.

Author ORCIDs.
Shashank Ravichandir https://orcid.org/0009-0005-8898-9961;
Meheboob Alam https://orcid.org/0000-0002-8900-5224.

Appendix A. Boltzmann equation and the DSMC algorithm

The Boltzmann equation (Chapman & Cowling 1970) provides a mesoscopic description of an N-particle system in terms of the time evolution of the single particle distribution function $f(\boldsymbol{r}, \boldsymbol{v}, t)$, and is appropriate to describe the behaviour of a dilute gas as long as two-particle and higher-order correlations are negligible. The single-particle distribution function is defined such that $f(\boldsymbol{r}, \boldsymbol{v}, t)\,\mathrm{d}\boldsymbol{r}\,\mathrm{d}\boldsymbol{v}$ is the average number of particles in an infinitesimal volume $\mathrm{d}\boldsymbol{r}$ at $\boldsymbol{r}$ having velocities in an infinitesimal interval $\mathrm{d}\boldsymbol{v}$ around $\boldsymbol{v}$. Thus, the integration of $f(\boldsymbol{r}, \boldsymbol{v}, t)$ over the entire phase space yields

$$\int f(\boldsymbol{r}, \boldsymbol{v}, t)\,\mathrm{d}\boldsymbol{r}\,\mathrm{d}\boldsymbol{v} = N, \tag{A1}$$

the total number of particles in the system. The Boltzmann equation can be written as

$$\frac{\partial f(\boldsymbol{r}, \boldsymbol{v}, t)}{\partial t} + \boldsymbol{v} \cdot \frac{\partial f(\boldsymbol{r}, \boldsymbol{v}, t)}{\partial \boldsymbol{r}} + \frac{\boldsymbol{F}}{m} \cdot \frac{\partial f(\boldsymbol{r}, \boldsymbol{v}, t)}{\partial \boldsymbol{v}} = \left(\frac{\partial f}{\partial t}\right)_{coll}. \tag{A2}$$

This evolution equation embodies the following facts. The distribution function $f(\boldsymbol{r}, \boldsymbol{v}, t)$ can change due to three processes: (i) the change in the location of particles due to local velocity (i.e. the second term on the left-hand side); (ii) the change in the velocity of particles due to external forcing $\boldsymbol{F}$ (i.e. the third term on the left-hand side); (iii) the change in the velocity of particles due to interparticle (binary) collisions represented by the term on the right-hand side of (A2). The exact form of the last term can be written down in terms of an integral operator in the velocity and physical space, thus making the Boltzmann equation (A2) a nonlinear integrodifferential equation.

The behaviour of gases/fluids under the continuum hypothesis is governed by the NSF equation and its variants, that can be obtained by coarse-graining the Boltzmann equation in the velocity space, leading to balance equations for the relevant low-order moments of the distribution function. For example, identifying the zeroth-, first- and second-order moments of $f(\boldsymbol{r}, \boldsymbol{v}, t)$ as the mass-density (ρ), momentum density ($\rho\boldsymbol{u}$) and energy density (e), respectively,

$$mn(\boldsymbol{r}, t) = m \int f(\boldsymbol{r}, \boldsymbol{v}, t)\,\mathrm{d}\boldsymbol{v} \equiv \rho(\boldsymbol{r}, t), \tag{A3}$$

$$mn(\boldsymbol{r}, t)u(\boldsymbol{r}, t) = m \int \boldsymbol{v} f(\boldsymbol{r}, \boldsymbol{v}, t)\,\mathrm{d}\boldsymbol{v}, \tag{A4}$$

$$\frac{3}{2} k_B n(\boldsymbol{r}, t) T(\boldsymbol{r}, t) = \frac{m}{2} \int [\boldsymbol{v} - \boldsymbol{u}(\boldsymbol{r}, t)]^2 f(\boldsymbol{r}, \boldsymbol{v}, t)\,\mathrm{d}\boldsymbol{v} \equiv e(\boldsymbol{r}, t), \tag{A5}$$

where n is the number density, $\boldsymbol{u}$ is the hydrodynamic velocity and T is the temperature, the celebrated NSF equations are found for the hydrodynamic fields $(\rho, \boldsymbol{u}, T)$. The NSF equations hold for near-equilibrium flows for which the Knudsen number is small $O(Kn)$

Downloaded from https://www.cambridge.org/core. IP address: 3.144.47.8, on 13 Nov 2024 at 06:58:59, subject to the Cambridge Core terms of use, available at https://www.cambridge.org/core/terms. https://doi.org/10.1017/jfm.2024.681

that can also be thought of as flows having small gradients in hydrodynamic fields. However, when $Kn > 0.001$, the continuum hypothesis breaks down and the rarefaction effects (such as non-zero slip velocity, temperature slips, normal stress differences, tangential heat flux, etc.) become increasingly important with increasing Kn, see figure 1, which depicts different flow regimes and the applicability of NSF and Boltzmann equations.

The main difficulty in solving the Boltzmann equation lies in computing the collision term $(\partial f/\partial t)_{coll}$ in (A2) that involves a five-fold integral in the velocity and physical space. To overcome this difficulty, Bird (1963) introduced a stochastic method, the DSMC method, that solves (A2) by integrating it using 'quasi' particles (Bird 1994; Pöschel & Schwager 2005). Instead of tracking the trajectories of real particles as in molecular dynamics, the DSMC maps a system containing real particles onto a set of smaller number of quasiparticles, thus making the computation more efficient than the standard molecular dynamics method. Initially, N 'computational' particles are distributed randomly in the simulation domain which is divided into cells for processing collisions and averaging. The change in the distribution function is implemented in two stages due to (i) streaming and (ii) collision of quasiparticles. The streaming stage incorporates the change in the velocity distribution function due to (i) local particle motion and (ii) external forcing; during this stage, the position vector and velocity vector of each particle are updated as

$$\boldsymbol{x}_i \rightarrow \boldsymbol{x}_i + \boldsymbol{v}_i \Delta t + \tfrac{1}{2}\boldsymbol{a}\Delta t^2, \tag{A6}$$

$$\boldsymbol{v}_i \rightarrow \boldsymbol{v}_i + \boldsymbol{a}\Delta t, \tag{A7}$$

where $\boldsymbol{a} = \boldsymbol{F}/m$ is the external acceleration. Note that this updating is done only for the particles which are unaffected by the boundary conditions. Once the particles are advected and the boundary conditions (see (A13*a*,*b*) and (A14)) are applied, they are sorted out into their respective collision cells based on their positions.

During the collision stage, the number of collisions within a cell of volume V_c during a given time step Δt is taken as (Bird 1994)

$$N_c = \frac{2\pi R^2 N_s^2 \langle |\boldsymbol{v}_{12}| \rangle \Delta t N_e}{V_c}, \tag{A8}$$

where N_s is the number of simulated particles in the cell, N_e is the ratio of real particles to simulated particles and $\boldsymbol{v}_{12} = \boldsymbol{v}_1 - \boldsymbol{v}_2$ is the relative velocity between two particles. A detailed derivation of the collision frequency and hence, the number of collisions in a time step, N_c can be found in Pöschel & Schwager (2005). The DSMC method processes this number of collisions by randomly choosing N_p pairs of particles where

$$N_p = \frac{8\pi R^2 N_s^2 v_{12}^{max} \Delta t N_e}{V_c}, \tag{A9}$$

and selecting only certain pairs based on an acceptance–rejection scheme such that the number of pairs chosen is equal to N_c. A collision between two particles is accepted if

$$\Theta(\boldsymbol{k} \cdot \boldsymbol{v}_{12})|\boldsymbol{k} \cdot \boldsymbol{v}_{12}| > \mathrm{rand}[0, 1) v_{12}^{max}, \tag{A10}$$

where Θ is the Heaviside function and $\boldsymbol{k}$ is an equidistributed random vector over a unit sphere. The maximum relative velocity v_{12}^{max} is initially set to be three times the mean probable velocity (Gupta & Alam 2017) and is dynamically updated to be the relative

Downloaded from https://www.cambridge.org/core. IP address: 3.144.47.8, on 13 Nov 2024 at 06:58:59, subject to the Cambridge Core terms of use, available at https://www.cambridge.org/core/terms. https://doi.org/10.1017/jfm.2024.681

velocity of a chosen pair that exceeds the defined maximum relative velocity. Once a pair of particles has been accepted, their post collision velocities are updated as

$$\boldsymbol{v}_i \rightarrow \boldsymbol{v}_i - [(\boldsymbol{v}_i - \boldsymbol{v}_j) \cdot \boldsymbol{k}_{ij}]\boldsymbol{k}_{ij}, \tag{A11}$$

$$\boldsymbol{v}_j \rightarrow \boldsymbol{v}_j + [(\boldsymbol{v}_i - \boldsymbol{v}_j) \cdot \boldsymbol{k}_{ij}]\boldsymbol{k}_{ij}, \tag{A12}$$

where $\boldsymbol{k}_{ij}$ is the unit vector along the line joining the centres of the colliding spheres and can be taken as the same vector $\boldsymbol{k}$ that was used in the acceptance rejection scheme.

The lateral walls at $y = \pm L_y/2$ have been modelled as fully 'diffuse' thermal walls (Bird 1994; Pöschel & Schwager 2005; Gupta & Alam 2018) for both pressure-driven and acceleration-driven flows. For a particle colliding with a fully diffuse thermal wall (maintained at a fixed temperature T_w), its x and z components of velocity are forgotten after a collision and are replaced by

$$v_x^{t+\Delta t} = \sqrt{\frac{k_B T_w}{m}} v_G + g t_{post} \quad \text{and} \quad v_z^{t+\Delta t} = \sqrt{\frac{k_B T_w}{m}} v_G, \tag{A13a,b}$$

where v_G is the velocity sampled from a Gaussian distribution with zero mean and a variance corresponding to the temperature of the wall ($T_w = 1$). On the other hand, the y-component of the postcollision velocity of a colliding particle with wall is changed according to the following rule:

$$v_y^{t+\Delta t} = \sqrt{\frac{2k_B T_w}{m}} v_{BG}, \tag{A14}$$

where v_{BG} represents a biased Gaussian distribution. Other technical details of the DSMC method can be found in Gupta & Alam (2017).

Appendix B. Local Knudsen, Mach and Reynolds Numbers

Since the density field varies across the flow domain in the pressure-driven Poiseuille flow, the global/average Knudsen number (2.7) is different from its local value. We define the 'local' Knudsen number in terms of the local density $\rho(x, y)$ as

$$Kn(x, y) = \frac{m}{\sqrt{2}\pi d^2 \rho(x, y) L_y} \equiv Kn_{local} \tag{B1}$$

such that

$$Kn \equiv \langle Kn(x, y) \rangle_{x,y} \equiv Kn_{global} \tag{B2}$$

represents the average/global value of the Knudsen number. The corresponding 'local' Mach and Reynolds numbers are defined as

$$Ma(x, y) = \frac{u_x(x, y)}{c_s(x, y)}, \quad \text{and} \quad Re(x, y) = \frac{Ma(x, y)}{Kn(x, y)} \sqrt{\frac{\gamma \pi}{2}}, \tag{B3a,b}$$

where c_s is the sound speed given by

$$c_s(x, y) = \sqrt{\gamma \frac{\partial p}{\partial \rho}} = \sqrt{\gamma \frac{k_B T(x, y)}{m}}, \tag{B4}$$

with $\gamma = 5/3$ for a monatomic gas.

Downloaded from https://www.cambridge.org/core. IP address: 3.144.47.8, on 13 Nov 2024 at 06:58:59, subject to the Cambridge Core terms of use, available at https://www.cambridge.org/core/terms. https://doi.org/10.1017/jfm.2024.681

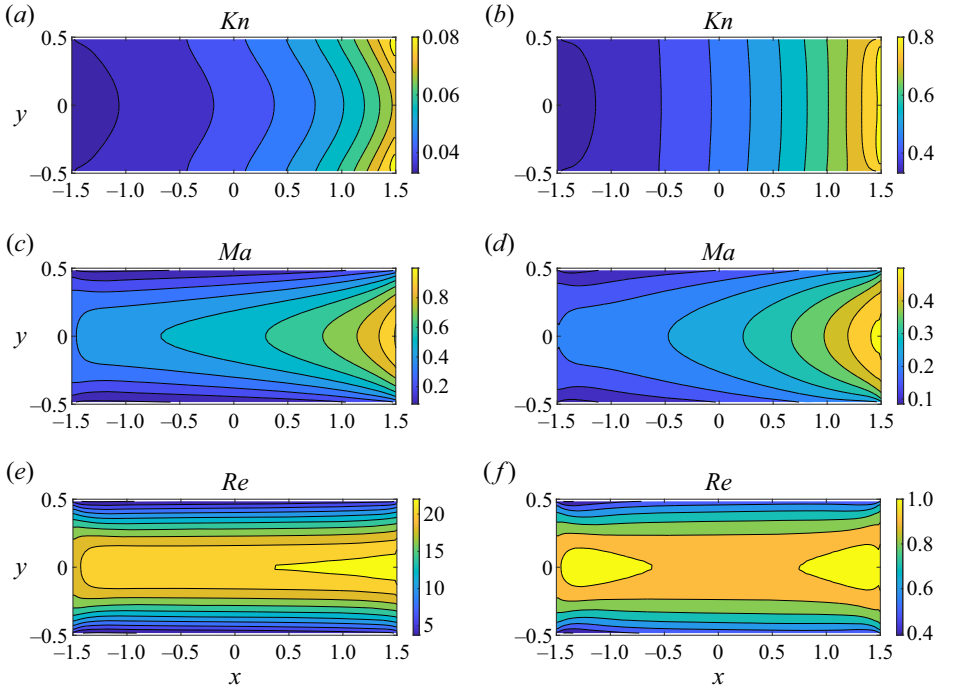

Figure 26. Contour plots of (*a*,*b*) $Kn(x, y)$, (*c*,*d*) $Ma(x, y)$ and (*e*,*f*) $Re(x, y)$ for global/average $Kn_{av} = \langle Kn \rangle = 0.05$ (*a*,*c*,*e*) and $Kn_{av} = \langle Kn \rangle = 0.5$ (*b*,*d*,*f*), with $\delta p/p_0 = 1$; other parameters as in figure 3.

The contour plots of $Kn(x, y)$, $Ma(x, y)$ and $Re(x, y)$ are displayed in figure 26(*a–f*) – figure 26(*a*,*c*,*e*) and figure 26(*b*,*d*,*f*) represent the data at 'global' Knudsen number (B2) of $Kn_{av} = \langle Kn \rangle = 0.05$ and 0.5, respectively; the pressure-difference is set to $\delta p/p_0 = 1.0$, with the channel aspect-ratio being $AR = L_x/L_y = 3$. It is seen that there exist significant variations of $Kn(x, y)$, $Ma(x, y)$ and $Re(x, y)$ across the flow domain. The analogous plots for a lower pressure-difference of $\delta p/p_0 = 0.1$ are displayed in figure 27(*a–f*). Comparing figures 26 and 27, we find that the magnitudes of Re and Ma decrease by an order of magnitude when the pressure difference is lowered from 1 to 0.1; also, the streamwise variations are relatively lesser at $\delta p/p_0 = 0.1$. For both cases, the flow belongs to the low-speed, subsonic regime.

Table 4 shows a comparison between the maximum values of Mach and Reynolds numbers occurring at the centre of the channel ($x = 0$ and $y = 0$) for the pressure-driven flow and the corresponding maximum Ma and Re occurring in its acceleration-driven counterpart with the dimensionless acceleration (2.10) being set to $\hat{a} = 0.1$. We conclude that similar values of forcing terms ($\delta p/p_0 = 1$ and $\hat{a} = 0.1$) produce flows with comparable Re and Ma in magnitude.

Appendix C. Burnett-order stress tensor and the Poiseuille flows

Here we write down the constitutive relations for the stress tensor (§ C.1), accurate up-to the Burnett order $O(Kn^2)$ (Burnett 1935; Kogan 1969; Chapman & Cowling 1970; Sela & Goldhirsch 1998), and derive expressions for (i) the shear stress and viscosity (§ C.2) and (ii) two normal stress differences (§ C.3) that hold for both pressure-driven and acceleration-driven Poiseuille flows.

Downloaded from https://www.cambridge.org/core. IP address: 3.144.47.8, on 13 Nov 2024 at 06:58:59, subject to the Cambridge Core terms of use, available at https://www.cambridge.org/core/terms. https://doi.org/10.1017/jfm.2024.681

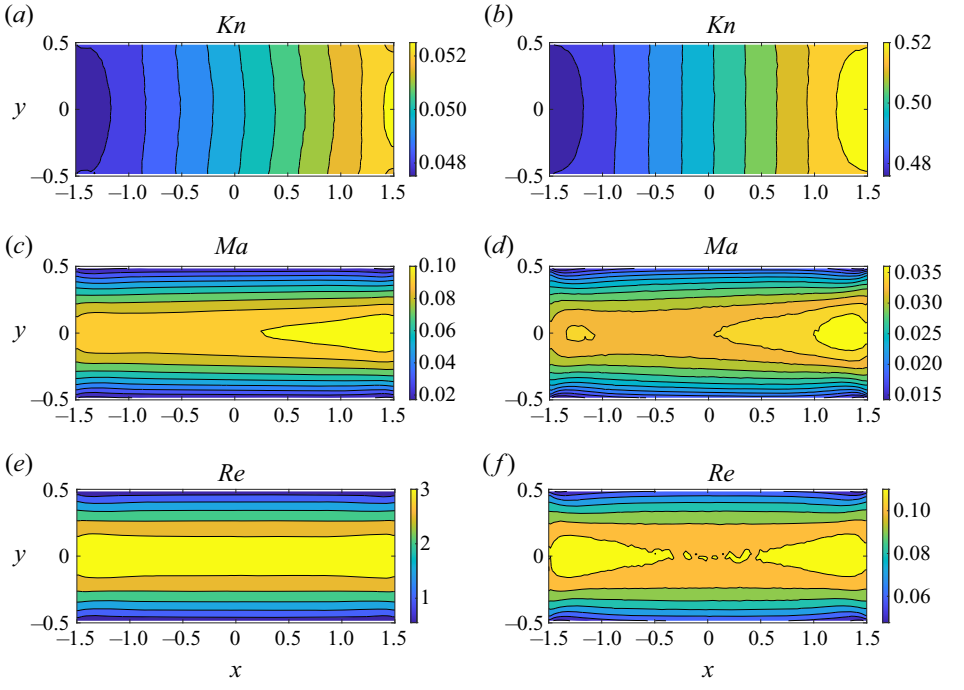

Figure 27. Same as figure 26, but for $\delta p/p_0 = 0.1$.

	Force-driven		Pressure-driven		Pressure-driven		
	$\hat{a} = 0.1$		$\delta p/p_0 = 1$		$\delta p/p_0 = 0.1$		
Kn	$Ma(0)$	$Re(0)$	$Ma(0,0)$	$Re(0,0)$	$Ma(0,0)$	$Re(0,0)$	p_0
0.05	0.54	17.54	0.56	21.92	0.099	3.22	1.21×10^{-3}
0.5	0.20	0.62	0.28	0.99	0.034	0.11	1.21×10^{-4}
5	0.19	0.064	0.25	0.088	0.030	0.01	1.21×10^{-5}
50	0.24	0.0078	0.25	0.0089	0.030	0.001	1.21×10^{-6}

Table 4. Comparison of the maximum values of Mach number and Reynolds number between the acceleration-driven ($\hat{a} = 0.1$) and pressure-driven ($\delta p/p_0 = 1$ and 0.1, with $L_x/L_y = 3$) Poiseuille flows.

C.1. *Stress tensor at Burnett order*

For a monatomic gas, the Burnett-order expression for the stress tensor (chapter 7 in Chapman & Cowling (1970); equation (46) in Sela & Goldhirsch (1998) with $\epsilon = 0$) is given by

$$\begin{aligned} P_{ij} = {} & p\delta_{ij} - 2\sqrt{2}\omega_0 \rho l_f T^{1/2} \overline{\partial_j u_i} + 2\omega_1 \rho l_f^2 \partial_k u_k \overline{\partial_j u_i} \\ & - 2\omega_2 \rho l_f^2 \left(3\overline{\partial_i \left(n^{-1} \partial_j p\right)} + \overline{\partial_k u_i \, \partial_j u_k} + 2\,\overline{\overline{\partial_k u_i} \partial_j u_k} \right) \\ & + 2\omega_3 \rho l_f^2 \overline{\partial_{ij} T} + 2\omega_4 \frac{l_f^2}{T} \overline{\partial_i p \partial_j T} + 2\omega_5 \frac{\rho l_f^2}{T} \overline{\partial_i T \partial_j T} + 2\omega_6 \rho l_f^2 \overline{\overline{\partial_k u_i} \, \overline{\partial_j u_k}}, \end{aligned} \tag{C1}$$

Downloaded from https://www.cambridge.org/core. IP address: 3.144.47.8, on 13 Nov 2024 at 06:58:59, subject to the Cambridge Core terms of use, available at https://www.cambridge.org/core/terms. https://doi.org/10.1017/jfm.2024.681

where the numerical constants ω_i are (Sela & Goldhirsch 1998)

$$\left.\begin{array}{llll} \omega_0 \approx 0.5627, & \omega_1 \approx 1.2845, & \omega_2 \approx 0.6422, & \omega_3 \approx 0.7656, \\ \omega_4 \approx 0.2157, & \omega_5 \approx 0.0693, & \omega_6 \approx 2.3510, & \end{array}\right\} \tag{C2}$$

and the mean free path of the gas is defined as

$$l_f = \frac{1}{\sqrt{2}\pi n d^2}. \tag{C3}$$

In (C1), an over-bar on a tensorial quantity denotes its deviatoric part, and we have adopted the following index notation for partial derivatives:

$$\partial_i = \frac{\partial}{\partial x_i}, \quad \partial_{ij} = \frac{\partial^2}{\partial x_i \partial x_j}. \tag{C4a,b}$$

Equation (C1) can be rewritten in terms of the velocity gradient tensor $\boldsymbol{L} = \boldsymbol{\nabla u}$, its symmetric part $\boldsymbol{D} = \mathrm{sym}(\boldsymbol{L})$, the deviatoric deformation $\boldsymbol{S} = \mathrm{dev}(\boldsymbol{D})$ and the dilatation $\Delta \equiv \partial_k u_k = \mathrm{trace}(\boldsymbol{D}) = \mathrm{trace}(\boldsymbol{L})$ as

$$\begin{aligned} P_{ij} = {} & p\delta_{ij} - 2\rho l_f \left(\sqrt{2}\omega_0 T^{1/2} - \omega_1 l_f \Delta\right) S_{ji} - 2(3\omega_2 - \omega_3)\rho l_f^2 \left(\partial_{ij} T - \frac{1}{3}\delta_{ij}\partial_{kk} T\right) \\ & - 6\omega_2 l_f^2 T \left(\partial_{ij}\rho - \frac{1}{3}\delta_{ij}\partial_{kk}\rho - \rho^{-1}\left(\partial_i n \partial_j \rho - \frac{1}{3}\delta_{ij}\left(\partial_k \rho\right)^2\right)\right) \\ & - 2l_f^2\ (3\omega_2 - \omega_4)\left(\frac{1}{2}\left(\partial_i T \partial_j \rho + \partial_j T \partial_i \rho\right) - \frac{1}{3}\delta_{ij}\partial_k T \partial_k \rho\right) \\ & + 2(\omega_4 + \omega_5)\frac{\rho l_f^2}{T}\left(\partial_i T \partial_j T - \frac{1}{3}\delta_{ij}\left(\partial_k T\right)^2\right) - 2\omega_2 \rho l_f^2 \left[\frac{1}{2}\left(L_{ik}L_{kj} + L_{jk}L_{ki}\right)\right. \\ & \left. - \frac{1}{3}\delta_{ij}L_{mk}L_{km} + \left(D_{ik}L_{kj} + D_{jk}L_{ki} - \frac{2\Delta}{3}D_{ij}\right) - \frac{2}{3}\delta_{ij}\left(D_{mk}L_{km} - \frac{\Delta^2}{3}\right)\right] \\ & + 2\omega_6 \rho l_f^2 \left[\left(D_{ik}D_{kj} - \frac{2\Delta}{3}D_{ij} + \frac{\Delta^2}{9}\delta_{ij}\right) - \frac{1}{3}\delta_{ij}\left(D_{mk}D_{km} - \frac{\Delta^2}{3}\right)\right]. \end{aligned} \tag{C5}$$

C.2. *Shear stress and shear viscosity in Poiseuille flows*

The expression for the xy-component of the Burnett-order shear stress (C5) is

$$\begin{aligned} P_{xy}(x, y, z) = {} & -2\rho l_f \left(\sqrt{2}\omega_0 T^{1/2} - \omega_1 l_f \Delta\right) S_{xy} - 2(3\omega_2 - \omega_3)\rho l_f^2\ \partial_{xy} T \\ & - 6\omega_2 l_f^2 T \left(\partial_{xy}\rho - \rho^{-1}\ \partial_x \rho \partial_y \rho\right) - l_f^2\ (3\omega_2 - \omega_4)\left(\partial_x T \partial_y \rho + \partial_y T \partial_x \rho\right) \\ & - 2\omega_2 \rho l_f^2 \left(\frac{1}{2}\left(L_{xk}L_{ky} + L_{yk}L_{kx}\right) + \left(D_{xk}L_{ky} + D_{yk}L_{kx} - \frac{2\Delta}{3}D_{xy}\right)\right) \\ & + 2(\omega_4 + \omega_5)\frac{\rho l_f^2}{T}\ \left(\partial_x T \partial_y T\right) + 2\omega_6 \rho l_f^2 \left(D_{xk}D_{ky} - \frac{2\Delta}{3}D_{xy}\right), \end{aligned} \tag{C6}$$

Downloaded from https://www.cambridge.org/core. IP address: 3.144.47.8, on 13 Nov 2024 at 06:58:59, subject to the Cambridge Core terms of use, available at https://www.cambridge.org/core/terms. https://doi.org/10.1017/jfm.2024.681

that holds for the pressure-driven Poiseuille flow for which the flow is homogeneous along the z-direction and the following relations hold:

$$\left.\begin{aligned}
&\partial/\partial z(.) = 0, \quad L_{zk} = 0 = L_{kz} = D_{kz} = D_{zk},\\
&D_{xy} = D_{yx} = \frac{1}{2}(\partial_y u_x + \partial_x u_y), \quad D_{xx} = \partial_x u_x = L_{xx}, \quad D_{yy} = \partial_y u_y = L_{yy},\\
&L_{xy} = \partial_y u_x, \quad L_{yx} = \partial_x u_y, \quad \mathcal{L}_{12} = L_{xy} - L_{yx},\\
&\Delta = \partial_x u_x + \partial_y u_y = D_{xx} + D_{yy} = L_{xx} + L_{yy},\\
&\mathcal{S}_1 = S_{xx} - S_{yy} = D_{xx} - D_{yy} = \mathcal{D}_1 = L_{xx} - L_{yy} = \mathcal{L}_1,\\
&\mathcal{S}_2 = S_{yy} - S_{zz} = D_{yy} - D_{zz} = \mathcal{D}_2 = L_{yy} - L_{zz} = \mathcal{L}_2.
\end{aligned}\right\} \tag{C7}$$

Let us evaluate the shear stress (C6) at the midchannel $(x, y) = (0, 0)$ as

$$\begin{aligned}
P_{xy}(0,0) &= -2\rho l_f \left(\sqrt{2}\omega_0 T^{1/2} - \omega_1 l_f \Delta\right) S_{xy} - 2(3\omega_2 - \omega_3)\rho l_f^2 \partial_{xy} T - 6\omega_2 l_f^2 T \partial_{xy}\rho\\
&\quad - 2\omega_2 \rho l_f^2 \left(\frac{1}{2}\left(L_{xy} + L_{yx}\right)\Delta + D_{xx}L_{xy} + D_{yy}L_{yx} + \frac{\Delta}{3}D_{xy}\right) + \frac{2}{3}\omega_6 \rho l_f^2 D_{xy}\Delta,\\
&\approx -2\rho l_f \left(\sqrt{2}\omega_0 T^{1/2} - (\omega_1 + \omega_6/3 - \omega_2/3)\, l_f \Delta\right) S_{xy} - 2\omega_2 \rho l_f^2 \left(\frac{3}{2} S_{xy}\Delta\right),\\
&= -2\rho l_f \left(\sqrt{2}\omega_0 T^{1/2} - \delta_1 l_f \Delta\right) S_{xy},
\end{aligned} \tag{C8}$$

with

$$\delta_1 = \omega_1 + \tfrac{1}{3}\omega_6 + \tfrac{11}{6}\omega_2 \approx 3.2455. \tag{C9}$$

The leading expression for the shear-viscosity, $\mu(0,0) = -P(0,0)/2S_{xy}$, in the pressure-driven Poiseuille flow simplifies to

$$\mu(0,0) = \rho l_f \left(\sqrt{2}\omega_0 T^{1/2} - \delta_1 l_f \Delta\right) = \mu_0 T^{1/2}\left(1 - \frac{\delta_1 l_f \Delta}{\sqrt{2}\omega_0 T^{1/2}}\right) \equiv \mu_{NSF}\mathcal{F}_0(T, \Delta), \tag{C10}$$

where

$$\mu_{NSF} = \mu_0\sqrt{T}, \quad \text{with } \mu_0 = \sqrt{2}\omega_0 \rho l_f \approx 0.7957 \rho l_f, \tag{C11}$$

is the viscosity at the NSF order and

$$\mathcal{F}_0(T, \Delta) = 1 - c_\mu Kn \frac{\tilde{\Delta}}{\sqrt{\tilde{T}}}, \quad \text{with } c_\mu = \frac{\omega_1 + \omega_6/3 + 11\omega_2/6}{\sqrt{2}\omega_0} \approx 4, \tag{C12}$$

is its correction due to dilatation. Note that $\tilde{T} = T/T_0$ is the dimensionless temperature and

$$\tilde{\Delta} = \Delta / \left(\frac{u_0}{L_y}\right) = \left(\frac{\partial u_x}{\partial x} + \frac{\partial u_y}{\partial y}\right)\left(\frac{L_y}{u_0}\right) \tag{C13}$$

is the dimensionless dilatation, with $u_0 = \sqrt{2k_B T_0/m}$, $k_B = 1/2$ and $T_0 = 1$ in the present simulations. In the main text and here onwards, we omit the 'tilde' to denote the dimensionless dilatation by Δ.

Downloaded from https://www.cambridge.org/core. IP address: 3.144.47.8, on 13 Nov 2024 at 06:58:59, subject to the Cambridge Core terms of use, available at https://www.cambridge.org/core/terms. https://doi.org/10.1017/jfm.2024.681

On the other hand, for the acceleration-driven Poiseuille flow, it is straightforward to verify from (C6) that the expression for the Burnett-order shear stress is

$$P_{xy} = -2\sqrt{2}\omega_0 \rho l_f T^{1/2} S_{xy} \tag{C14}$$

which is identical to that at the NSF order. Therefore, for the acceleration-driven Poiseuille flow, the shear viscosity is

$$\mu = \sqrt{2}\omega_0 \rho l_f T^{1/2} \equiv \mu_0 T^{1/2}, \quad \text{with } \mu_0 = \sqrt{2}\omega_0 \rho l_f \approx 0.7957 \rho l_f, \tag{C15}$$

that holds up to the Burnett-order $O(Kn^2)$. For viscometric flows such as in the plane shear flow, it is known (Chapman & Cowling 1970; Saha & Alam 2020) that

$$\mu_{NSF} = \mu_{Burnett}, \tag{C16}$$

for a monatomic gas, and the non-zero contribution (beyond NSF order) to the shear viscosity of gases appears at the super-Burnett order and beyond.

C.3. *First and second normal stress differences in Poiseuille flows*

For general flows with arbitrary deformation $\boldsymbol{L}$, the scaled first normal stress difference is

$$\begin{aligned}
\mathcal{N}_1(x,y,z) &\overset{\text{def}}{=} \frac{P_{xx} - P_{yy}}{p} \\
&= -2\frac{l_f}{T}\left(\sqrt{2}\omega_0 T^{1/2} - \omega_1 l_f \Delta\right)\left(S_{xx} - S_{yy}\right) - 2\left(3\omega_2 - \omega_3\right)\frac{l_f^2}{T}\left(\partial_{xx}T - \partial_{yy}T\right) \\
&\quad - 6\omega_2 \frac{l_f^2}{\rho}\left(\partial_{xx}\rho - \partial_{yy}\rho - \rho^{-1}\left((\partial_x\rho)^2 - \left(\partial_y\rho\right)^2\right)\right) \\
&\quad - 2\left(3\omega_2 - \omega_4\right)\frac{l_f^2}{p}\left(\partial_x T \partial_x \rho - \partial_y T \partial_y \rho\right) + 2(\omega_4 + \omega_5)\frac{l_f^2}{T^2}\left((\partial_x T)^2 - \left(\partial_y T\right)^2\right) \\
&\quad - 2\omega_2 \frac{l_f^2}{T}\left(L_{xk}L_{kx} - L_{yk}L_{ky} + 2\left(D_{xk}L_{kx} - D_{yk}L_{ky}\right) - \frac{2\Delta}{3}\left(D_{xx} - D_{yy}\right)\right) \\
&\quad + 2\omega_6 \frac{l_f^2}{T}\left[D_{xk}D_{kx} - D_{yk}D_{ky} - \frac{2\Delta}{3}\left(D_{xx} - D_{yy}\right)\right],
\end{aligned} \tag{C17}$$

and the scaled second normal stress difference is

$$\begin{aligned}
\mathcal{N}_2(x,y,z) &\overset{\text{def}}{=} \frac{P_{yy} - P_{zz}}{p} \\
&= -2\frac{l_f}{T}\left(\sqrt{2}\omega_0 T^{1/2} - \omega_1 l_f \Delta\right)\left(S_{yy} - S_{zz}\right) - 2\left(3\omega_2 - \omega_3\right)\frac{l_f^2}{T}\left(\partial_{yy}T - \partial_{zz}T\right) \\
&\quad - 6\omega_2 \frac{l_f^2}{\rho}\left(\partial_{yy}\rho - \partial_{zz}\rho - \rho^{-1}\left((\partial_y\rho)^2 - (\partial_z\rho)^2\right)\right) \\
&\quad - 2\left(3\omega_2 - \omega_4\right)\frac{l_f^2}{p}\left(\partial_y T \partial_y \rho - \partial_z T \partial_z \rho\right) + 2(\omega_4 + \omega_5)\frac{l_f^2}{T^2}\left((\partial_y T)^2 - (\partial_z T)^2\right)
\end{aligned}$$

Downloaded from https://www.cambridge.org/core. IP address: 3.144.47.8, on 13 Nov 2024 at 06:58:59, subject to the Cambridge Core terms of use, available at https://www.cambridge.org/core/terms. https://doi.org/10.1017/jfm.2024.681

$$- 2\omega_2 \frac{l_f^2}{T}\left(L_{yk}L_{ky} - L_{zk}L_{kz} + 2\left(D_{yk}L_{ky} - D_{zk}L_{kz}\right) - \frac{2\Delta}{3}\left(D_{yy} - D_{zz}\right)\right)$$
$$+ 2\omega_6 \frac{l_f^2}{T}\left[D_{yk}D_{ky} - D_{zk}D_{kz} - \frac{2\Delta}{3}\left(D_{yy} - D_{zz}\right)\right]. \tag{C18}$$

Note that

$$-2\frac{l_f}{T}\left(\sqrt{2}\omega_0 T^{1/2} - \omega_1 l_f \Delta\right) = -\frac{2\mu_0\sqrt{T}}{p}\left(1 - \frac{\omega_1}{\sqrt{2}\omega_0} Kn \frac{\Delta}{\sqrt{T}}\right) = -\frac{2\mu(T,\Delta)}{p}, \tag{C19}$$

where

$$\mu(T,\Delta) = \mu_{NS}\mathcal{F}(\Delta), \quad \mathcal{F}(\Delta) = 1 - c_\mu Kn \frac{\Delta}{\sqrt{T}} \quad \text{and} \quad \mu_{NS} = \mu_0\sqrt{T}, \tag{C20a–c}$$

with $c_\mu = \omega_1/\sqrt{2}\omega_0 \approx 1.6144$.

For the pressure-driven case, inserting (C7) into (C17) and (C18), the expressions for the first and second normal stress differences at the middle $(x, y) = (0, 0)$ of the channel are considerably simplified:

$$\mathcal{N}_1(0,0) = c_1 \frac{l_f^2}{\rho}\left(\partial_{yy}\rho - \partial_{xx}\rho - \rho^{-1}(\partial_x\rho)^2\right) + c_2 \frac{l_f^2}{T}\left(\partial_{yy}T - \partial_{xx}T\right) - \frac{2\mu(T,\Delta)}{p}\mathcal{S}_1$$
$$- 2\left(3\omega_2 - \omega_4\right)\frac{l_f^2}{p}\left(\partial_x T \partial_x \rho\right) + 2(\omega_4 + \omega_5)\frac{l_f^2}{T^2}\left(\partial_x T\right)^2 - \frac{2}{3}\left(4\omega_2 - \omega_6\right)\frac{l_f^2}{T}\mathcal{S}_1\Delta$$
$$\approx c_1 Kn^2 p^{-1}\partial_{yy}p - (c_1 - c_2)Kn^2 T^{-1}\,\partial_{yy}T - \frac{2\mu(T,\Delta)}{p}\,\mathcal{S}_1$$
$$- c_3 Kn^2 p^{-1}\,\partial_x T \partial_x \rho + c_4 Kn^2 T^{-2}(\partial_x T)^2 - c_5 Kn^2 T^{-1}\mathcal{S}_1\Delta, \tag{C21}$$
$$\approx -\frac{2\mu(T,\Delta)}{p}\,\mathcal{S}_1 + c_1 Kn^2 p^{-1}\partial_{yy}p - (c_1 - c_2)Kn^2 T^{-1}\partial_{yy}T, \tag{C22}$$

$$\mathcal{N}_2(0,0) = -Kn^2\left(c_1 p^{-1}\partial_{yy}p + (c_2 - c_1)T^{-1}\partial_{yy}T\right) - \frac{2\mu(T,\Delta)}{p}\,\mathcal{S}_2$$
$$- 2\omega_2\frac{l_f^2}{T}\left(3L_{yy}^2 - \frac{2}{3}\mathcal{S}_2\Delta\right) + 2\omega_6\frac{l_f^2}{T}\left[D_{yy}^2 - \frac{2}{3}\mathcal{S}_2\Delta\right]$$
$$= -Kn^2\left(c_1 p^{-1}\partial_{yy}p + (c_2 - c_1)T^{-1}\partial_{yy}T\right) - \frac{2\mu(T,\Delta)}{p}\,\mathcal{S}_2$$
$$- Kn^2 T^{-1}\left(c_6\Delta - c_7\mathcal{S}_2\right)\mathcal{S}_2, \tag{C23}$$

Downloaded from https://www.cambridge.org/core. IP address: 3.144.47.8, on 13 Nov 2024 at 06:58:59, subject to the Cambridge Core terms of use, available at https://www.cambridge.org/core/terms. https://doi.org/10.1017/jfm.2024.681

$$\approx (c_1 - c_2)Kn^2 T^{-1}\partial_{yy}T - c_1 Kn^2 p^{-1}\partial_{yy}p - \frac{2\mu(T,\Delta)}{p}\mathcal{S}_2. \tag{C24}$$

In the above the density derivatives are replaced by the pressure derivatives via the equation of state $p = \rho T$ and

$$\rho^{-1}\partial_{yy}\rho = p^{-1}\partial_{yy}p - T^{-1}\partial_{yy}T, \quad \text{at} y = 0. \tag{C25}$$

The numerical values of c_i are

$$\left.\begin{aligned} &c_1 = 6\omega_2 = 3.8532, \quad c_2 = 2\,(3\omega_2 - \omega_3) = 2.322, \quad c_3 = 2(2\omega_2 - \omega_4) \approx 2.1374,\\ &c_4 = 2(\omega_4 + \omega_5) = 0.57, \quad c_5 = \tfrac{2}{3}\,(4\omega_2 - \omega_6) \approx 0.1452,\\ &c_6 = \tfrac{4}{3}\,(\omega_6 - \omega_2) \approx 2.2784, \quad c_7 = 2\,(\omega_6 - 3\omega_2) \approx 0.8488. \end{aligned}\right\} \tag{C26}$$

From the present simulation data on the pressure-driven Poiseuille flow with $Kn = 0.05$, $AR = 3$ and $\delta p/p_0 = 1.0$, the following estimates hold at the channel centre $(x, y) = (0, 0)$:

$$\left.\begin{aligned} &\partial_{yy}T \approx 0.75, \quad \partial_{yy}p \approx 0.07, \quad \partial_{yy}\rho \approx -0.90,\\ &\partial_{xx}T \approx -0.025, \quad \partial_{xx}p \approx -0.11, \quad \partial_{xx}\rho \approx -0.09,\\ &\partial_{x}T \approx -0.04, \quad \partial_{x}p \approx -0.27, \quad \partial_{x}\rho \approx -0.23, \end{aligned}\right\} \quad \text{(figures 10 and 12)} \tag{C27}$$

$$\left.\begin{aligned} &D_{xy}(0,0) = \frac{1}{2}\frac{\partial u_y}{\partial x}(0,0) = 0 = D_{yx} = S_{xy} = S_{yx} = L_{xy} = L_{yx}, \quad \lim_{\dot\gamma\to 0}\frac{L_{xy}}{D_{xy}} = 2,\\ &D_{xx}(0,0) = \frac{\partial u_x}{\partial x}(0,0) = -\frac{\rho u_x}{\rho^2}\frac{\partial \rho}{\partial x}\bigg|_{(0,0)} \approx 0.096 \sim O(10^{-1}), \quad \text{(figures 5c, 10e and 12b)}\\ &D_{yy}(0,0) = L_{yy}(0,0) = \frac{\partial u_y}{\partial y}(0,0) \sim O(5\times 10^{-3}), \quad \text{(figure 6c)}\\ &\mathcal{S}_1(0,0) = \left(D_{xx} - D_{yy}\right)(0,0) \approx D_{xx}(0,0) \sim O(10^{-1})\\ &\mathcal{S}_2(0,0) = D_{yy}(0,0) \sim O(5\times 10^{-3})\\ &\Delta(0,0) = \left(L_{xx} + L_{yy}\right)(0,0) \approx L_{xx}(0,0) \sim O(10^{-1})\\ &\frac{D_{xx}}{D_{yy}}\bigg|_{(0,0)} \approx 20, \quad \frac{\Delta}{D_{yy}}\bigg|_{(0,0)} \approx 21, \quad \frac{\mu}{p}\bigg|_{(0,0)} \approx 0.05. \quad \text{(figures 12a and 16c)} \end{aligned}\right\} \tag{C28}$$

Downloaded from https://www.cambridge.org/core. IP address: 3.144.47.8, on 13 Nov 2024 at 06:58:59, subject to the Cambridge Core terms of use, available at https://www.cambridge.org/core/terms. https://doi.org/10.1017/jfm.2024.681

Using the above values, the different terms in (C22)–(C24), evaluated at the midchannel $(0, 0)$ for $Kn = 0.05$, are approximated as

$$\left.\begin{array}{l} -c_3 Kn^2 p^{-1}\partial_x T\partial_x \rho \approx -4.3\times 10^{-5}, \quad c_4 Kn^2 T^{-2}(\partial_x T)^2 \approx +2.6\times 10^{-6}, \\ -c_5 Kn^2 T^{-1}\mathcal{S}_1 \Delta \approx -3.88\times 10^{-6} \\ c_1 Kn^2 p^{-1}\partial_{yy} p \approx +6\times 10^{-4}, \quad -(c_1-c_2)Kn^2 T^{-1}\,\partial_{yy} T \approx -3\times 10^{-3} \\ \left.\begin{array}{l} c_1 Kn^2 p^{-1}\partial_{yy} p - (c_1-c_2)Kn^2 T^{-1}\,\partial_{yy} T \approx -2.4\times 10^{-3} \\ -\dfrac{2\mu}{p}\,(1-1.6141 Kn\Delta)\,\mathcal{S}_1 \approx -10^{-2} \end{array}\right\} \Rightarrow \mathcal{N}_1(0,0) < 0 \\ -\dfrac{2\mu}{p}\,(1-1.6141 Kn\Delta)\,(\mathcal{S}_1, \mathcal{S}_2)\,|_{(0,0)} \approx -\,(10^{-2}, 5\times 10^{-4}) \\ -Kn^2 T^{-1}\,(c_3\Delta - c_4\mathcal{S}_2)\,\mathcal{S}_2|_{(0,0)} \approx -0.2383 Kn^2\mathcal{S}_2 \approx -3\times 10^{-6} \\ -c_1 Kn^2 p^{-1}\partial_{yy} p \approx -9\times 10^{-4} \\ \left.\begin{array}{l} -c_1 Kn^2 p^{-1}\partial_{yy} p - \dfrac{2\mu}{p}\,(1-1.6141 Kn\Delta)\,\mathcal{S}_2 \approx -1.4\times 10^{-3} \\ (c_1-c_2)Kn^2 T^{-1}\partial_{yy} T \approx \ +2\times 10^{-3} \end{array}\right\} \Rightarrow \mathcal{N}_2(0,0) > 0. \end{array}\right\} \tag{C29}$$

We have verified from our simulation data that the above estimates also hold at $Kn = 0.5$. In summary, the Burnett-order theory predicts that

$$\mathcal{N}_1(0,0) < 0 \quad \text{and} \quad \mathcal{N}_2(0,0) > 0, \tag{C30a,b}$$

for small Kn in the pressure-driven gaseous Poiseuille flow through a finite-length ($L_x < \infty$) channel.

For the acceleration-driven Poiseuille flow, we have

$$\left.\begin{array}{l} \partial/\partial x(.) = 0 = \partial/\partial z(.), \quad \Delta = 0 = L_{zk} = L_{kz} = D_{kz} = D_{zk} = D_{ii}, \\ D_{xy} = D_{yx} = \frac{1}{2}\partial_y u_x, \quad L_{xy} = \partial_y u_x, \quad L_{yx} = 0. \end{array}\right\} \tag{C31}$$

Hence the expressions for the first and second normal stress differences are

$$\begin{aligned} \mathcal{N}_1(y) &= 2\,(3\omega_2 - \omega_3)\,\frac{l_f^2}{T}\,\partial_{yy} T + 6\omega_2 \frac{l_f^2}{\rho}\left(\partial_{yy}\rho - \rho^{-1}\left(\partial_y \rho\right)^2\right) \\ &\quad + 2\,(3\omega_2 - \omega_4)\,\frac{l_f^2}{p}\partial_y T\partial_y \rho - 2(\omega_4 + \omega_5)\frac{l_f^2}{T^2}\,\left(\partial_y T\right)^2 \\ &\quad + 2\omega_2 \frac{l_f^2}{T}\left(\frac{\partial u_x}{\partial y}\right)^2, \\ \mathcal{N}_2(y) &= -2\,(3\omega_2 - \omega_3)\,\frac{l_f^2}{T}\left(\partial_{yy} T\right) - 6\omega_2 \frac{l_f^2}{\rho}\left(\partial_{yy}\rho - \rho^{-1}\left(\partial_y \rho\right)^2\right) \\ &\quad - 2\,(3\omega_2 - \omega_4)\,\frac{l_f^2}{p}\partial_y T\partial_y \rho + 2(\omega_4 + \omega_5)\frac{l_f^2}{T^2}\,(\partial_y T)^2 \end{aligned} \tag{C32}$$

Downloaded from https://www.cambridge.org/core. IP address: 3.144.47.8, on 13 Nov 2024 at 06:58:59, subject to the Cambridge Core terms of use, available at https://www.cambridge.org/core/terms. https://doi.org/10.1017/jfm.2024.681

$$-\frac{1}{2}\left(4\omega_2-\omega_6\right)\frac{l_f^2}{T}\left(\frac{\partial u_x}{\partial y}\right)^2. \tag{C33}$$

At the midchannel $y=0$ (for which $\partial/\partial y(u_x,\rho,T)=0$), these expressions simplify to

$$\begin{aligned}\mathcal{N}_1(0)&=2\left(3\omega_2-\omega_3\right)\frac{l_f^2}{T}\partial_{yy}T+6\omega_2\frac{l_f^2}{\rho}\partial_{yy}\rho\\&=-1.5312\frac{l_f^2}{T}\partial_{yy}T+3.853\frac{l_f^2}{p}\partial_{yy}p\end{aligned} \tag{C34}$$

$$\mathcal{N}_2(0)=-2\left(3\omega_2-\omega_3\right)\frac{l_f^2}{T}\partial_{yy}T-6\omega_2\frac{l_f^2}{\rho}\partial_{yy}\rho=-\mathcal{N}_1(y). \tag{C35}$$

From the simulation data in figures 12(d) and 12(f), it is clear that

$$\partial_{yy}p>\partial_{yy}T>0, \tag{C36}$$

and therefore $\mathcal{N}_1(0)>0$ and $\mathcal{N}_2(0)<0$ at the middle of the channel (see figure 20c,d) in the acceleration-driven Poiseuille flow.

References

Akhlaghi, H., Roohi, E. & Stefanov, S. 2023 A comprehensive review on micro- and nano-scale gas flow effects: slip-jump phenomena, Knudsen paradox, thermally-driven flows, and Knudsen pumps. *Phys. Rep.* **997**, 1–60.

Alam, M., Gupta, R. & Ravichandir, S. 2021 Shear-induced heat transport and the relevance of generalized Fourier's law in granular Poiseuille flow. *Phys. Rev. Fluids* **6** (11), 114303.

Alam, M. & Luding, S. 2003 First normal stress difference and crystallization in a dense sheared granular fluid. *Phys. Fluids* **15** (8), 2298–2312.

Alam, M. & Luding, S. 2005 Non-Newtonian granular fluid: simulation and theory. In *Powders and Grains* (ed. R. Garcia-Rojo, H. J. Herrmann & S. McNamara), pp. 1141–1144. A.A. Balkema.

Alam, M., Mahajan, A. & Shivanna, D. 2015 On Knudsen-minimum effect and temperature bimodality in a dilute granular Poiseuille flow. *J. Fluid Mech.* **782**, 99–126.

Alaoui, M. & Santos, A. 1992 Poiseuille flow driven by an external force. *Phys. Fluids* A **4**, 1273–1282.

Aoki, K., Takata, S. & Nakanishi, T. 2002 Poiseuille-type flow of a rarefied gas between two parallel plates driven by a uniform external force. *Phys. Rev.* E **65** (2), 026315.

Arkilic, E.B., Schmidt, M.A. & Breuer, K.S. 1997 Rarefied gas flow through a long rectangular channel. *J. Micromech. Syst.* **6** (2), 167–178.

Beskok, A. & Karniadakis, G.E. 1999 A model for flows in channels, pipes and ducts at micro and nano scales. *Nanoscale Microscale Thermophys. Engng* **3** (1), 43–77.

Bird, G.A. 1963 Approach to translational equilibrium in a rigid sphere gas. *Phys. Fluids* **6** (10), 1518–1519.

Bird, G.A. 1994 *Molecular Gas Dynamics and the Direct Simulation of Gas Flows*. Clarendon.

Brancher, R., Johansson, M.V., Perrier, P. & Graur, I.A. 2021 Measurements of pressure gradient and temperature gradient driven flows in a rectangular channel. *J. Fluid Mech.* **923**, A35.

Burnett, D. 1935 The distribution velocities in a slightly non-uniform gas. *Proc. Lond. Math. Soc.* **39**, 385–430.

Cercignani, C. 1979 Rarefied gas flow through long slots. *Z. Angew. Math. Phys.* **30**, 943–951.

Cercignani, C. & Daneri, A. 1963 Flow of a rarefied gas between two parallel plates. *J. Appl. Phys.* **34** (12), 3509–3513.

Chapman, S. & Cowling, T.G. 1970 *The Mathematical Theory of Nonuniform Gases*. Cambridge University Press.

Ewart, T., Perrier, P., Graur, I.A. & Méolans, J.G. 2007 Mass flow rate measurements in a microchannel, from hydrodynamic to near free molecular regime. *J. Fluid Mech.* **584**, 337–356.

Goddard, J.D. 2014 Continuum modelling of granular media. *Appl. Mech. Rev.* **66**, 050801.

Grad, H. 1949 On the kinetic theory of rarefied gases. *Commun. Pure Appl. Maths* **2**, 331–407.

Downloaded from https://www.cambridge.org/core. IP address: 3.144.47.8, on 13 Nov 2024 at 06:58:59, subject to the Cambridge Core terms of use, available at https://www.cambridge.org/core/terms. https://doi.org/10.1017/jfm.2024.681

GRAUR, I.A., PERRIER, P., GHOZLANI, W. & MEOLANS, J.G. 2009 Measurements of tangential momentum accommodation coefficient for various gases in plane microchannel. *Phys. Fluids* **21** (10), 102004.
GUPTA, R. & ALAM, M. 2017 Hydrodynamics, wall-slip, and normal-stress differences in rarefied granular Poiseuille flow. *Phys. Rev.* E **95** (2), 022903.
GUPTA, R. & ALAM, M. 2018 Disentangling the role of athermal walls on the Knudsen paradox in molecular and granular gases. *Phys. Rev.* E **97** (1), 012912.
JACKSON, R. 2000 *Dynamics of Fluidized Particles*. Cambridge University Press.
KEERTHI, A., *et al.*2018 Ballistic molecular transport through two-dimensional channels. *Nature* **558** (7710), 420–424.
KNUDSEN, M. 1909 Die Gesetze der Molekularströmung und der inneren Reibungsströmung der Gase durch Röhren. *Ann. Phys.* **333** (1), 75–130.
KOGAN, M.K. 1969 *Rarefied Gas Dynamics*. Plenum.
KRISHNARAJ, K.P. & NOTT, P.R. 2016 A dilatation-driven vortex flows in sheared granular materials explains a rheometric anomaly. *Nat. Commun.* **7**, 10630.
KUNZE, S, GROLL, R., BESSER, B. & THÖMING, J. 2022 Molecular diameters of rarefied gases. *Sci. Rep.* **12**, 2057–2069.
KUNZE, S., PERRIER, O., GROLL, R., BESSER, B., VAROUTIS, S., LÜTTGE, A., GRAUR, I. & THÖMING, J. 2023 Rarefied gas flow in functionalized microchannels. arXiv:2301.12575v1.
LV, Q., LIU, X., WANG, E. & WANG, S. 2013 Analytical solution to predicting gaseous mass flow rates of microchannels in a wide rage of Knudsen numbers. *Phys. Rev.* E **88**, 013007.
MANSOUR, M.M., BARAS, F. & GARCIA, A.L. 1997 On the validity of hydrodynamics in plane Poiseuille flows. *Physica* A **240** (1–2), 255–267.
MARINO, L. 2009 Experiments on rarefied gas flows through tubes. *Microfluid. Nanofluid.* **6**, 109–119.
OHWADA, T., SONE, Y. & AOKI, K. 1989 Numerical analysis of the Poiseuille and thermal transpiration flows between two parallel plates on the basis of the Boltzmann equation for hard-sphere molecules. *Phys. Fluids* A **1** (12), 2042–2049.
PERRIER, P., GRAUR, I.A., EWART, T. & MEOLANS, J.G. 2011 Mass flow rate measurements in microtubes: from hydrodynamic to near free molecular regime. *Phys. Fluids* **23** (4), 042004.
PÖSCHEL, T. & SCHWAGER, T. 2005 *Computational Granular Dynamics: Models and Algorithms*. Springer.
RAGHURAMAN, P. & WILLIS, D.R. 1977 Kinetic theory analysis of rarefied gas flow through finite length slots. *Phys. Fluids* **20** (6), 895–902.
RATH, A., SINGH, N. & AGRAWAL, A. 2018 A perturbation-based solution of Burnett equations for gaseous flow in a long microchannel. *J. Fluid Mech.* **844**, 1038–1051.
RATH, A., YADAV, U. & AGRAWAL, A. 2021 Analytical solution of the Burnett equations for gaseous flow in a long microchannel. *J. Fluid Mech.* **912**, A53.
RAVICHANDIR, S. & ALAM, M. 2024 Hydrodynamics, normal stress differences and heat transfer in rarefied pressure-driven Poiseuille flow. In *AIP Conf. Proc.* (ed. R.S. Myong, K. Xu & J.S. Wu), vol. 2996, p. 080005. AIP Publishing.
REDDY, M.H.L. & ALAM, M. 2020 Regularized extended hydrodynamic equations for a rarefied granular gas and the plane shock waves. *Phys. Rev. Fluids* **5** (4), 044302.
REYNOLDS, O. 1885 On the dilatancy of media composed of rigid particles in contact, with experimental illustrations. *Phil. Mag.* **20**, 469–482.
RONGALI, R. & ALAM, M. 2018*a* Asymptotic expansion and Padè approximants for acceleration-driven Poiseuille flow of a rarefied gas: Bulk hydrodynamics and rheology. *Phys. Rev.* E **98** (1), 012115.
RONGALI, R. & ALAM, M. 2018*b* Asymptotic expansion and Padè approximants for gravity-driven flow of a heated granular gas: competition between inelasticity and forcing, up-to Burnett order. *Phys. Rev.* E **98** (5), 052144.
SAHA, S. & ALAM, M. 2016 Normal stress differences, their origin and constitutive relations for a sheared granular fluid. *J. Fluid Mech.* **795**, 549–580.
SAHA, S. & ALAM, M. 2017 Revisiting ignited-quenched transition and the non-Newtonian rheology of a sheared dilute gas–solid suspension. *J. Fluid Mech.* **833**, 206–246.
SAHA, S. & ALAM, M. 2020 Burnett-order constitutive relations, second-moment anisotropy and co-existing states in sheared dense gas–solid suspensions. *J. Fluid Mech.* **887**, A9.
SELA, N. & GOLDHIRSCH, I. 1998 Hydrodynamic equations for rapid flows of smooth inelastic spheres, to Burnett order. *J. Fluid Mech.* **361**, 41–74.
SHARIPOV, F.M. 1999 Rarefied gas flow through a long rectangular channel. *J. Vac. Sci. Technol.* A **17**, 3062.
SHARIPOV, F.M. & SELEZNEV, V.D. 1994 Rarefied gas flow through a long tube at any pressure ratio. *J. Vac. Sci. Technol.* A **12**, 2933–2935.
SONE, Y. 2000 Flows induced by temperature fields in a rarefied gas and their ghost effect on the behaviour of a gas in the continuum limit. *Annu. Rev. Fluid Mech.* **32**, 779–811.

Downloaded from https://www.cambridge.org/core. IP address: 3.144.47.8, on 13 Nov 2024 at 06:58:59, subject to the Cambridge Core terms of use, available at https://www.cambridge.org/core/terms. https://doi.org/10.1017/jfm.2024.681

TAHERI, P., TORRILHON, M. & STRUCHTRUP, H. 2009 Couette and Poiseuille microflows: analytical solutions for regularized 13-moment equations. *Phys. Fluids* **21**, 017102.

TAKATA, S. & FUNAGANE, H. 2011 Poiseuille and thermal transpiration flows of a highly rarefied gas: over-concentration in the velocity distribution function. *J. Fluid Mech.* **669**, 242–259.

TIJ, M. & SANTOS, A. 1994 Perturbation analysis of a stationary non-equilibrium flow generated by an external force. *J. Stat. Phys.* **76** (5), 1399–1414.

TIJ, M. & SANTOS, A. 2004 Poiseuille flow in a heated granular gas. *J. Stat. Phys.* **117** (5), 901–928.

TISON, S.A. 1993 Experimental data and theoretical modelling of gas flows through metal capillary leaks. *Vaccum* **44**, 1171–1174.

TITAREV, V.A. & SHAKHOV, E.M. 2010 Nonisothermal gas flow in a long channel. *Comput. Maths Math. Phys.* **50**, 2231–2244.

TITAREV, V.A. & SHAKHOV, E.M. 2012 Efficient method for computing rarefied gas flow in a long finite plane channel. *Comput. Maths Math. Phys.* **52** (2), 269–284.

TORRILHON, M. 2016 Modelling non-equilibrium gas flow based on moment equations. *Annu. Rev. Fluid Mech.* **48**, 429–458.

URIBE, F.J. & GARCIA, A.L. 1999 Burnett description for plane Poiseuille flow. *Phys. Rev.* E **60** (4), 4063–4078.

YANG, Z. & GARIMELLA, S.V. 2009 Rarefied gas flow in microtubes at different inlet-outlet pressure ratios. *Phys. Fluids* **21** (5), 052005.

ZHENG, Y., GARCIA, A.L. & ALDER, B.J. 2002 Comparison of kinetic theory and hydrodynamics for Poiseuille flow. *J. Stat. Phys.* **109** (3), 495–505.

Downloaded from https://www.cambridge.org/core. IP address: 3.144.47.8, on 13 Nov 2024 at 06:58:59, subject to the Cambridge Core terms of use, available at https://www.cambridge.org/core/terms. https://doi.org/10.1017/jfm.2024.681